FLEXIBLE, IMPLANTABLE, MICRO-ELECTRODE PROBES WITH AN ULTRAFAST DEGRADING POLYMER COATING AS A TEMPORARY INSERTION AID FOR LONG TERM NEURONAL SIGNAL AQUISITION

By

MENG-CHEN LO

A Dissertation submitted to the
Graduate School –New Brunswick
Rutgers, the State University of New Jersey
And
The Graduate School of Biomedical Sciences
In Partial Fulfillment of the Requirements

For the Degree of

Doctor of Philosophy

Graduate program in Biomedical Engineering
Written under the direction of
Dr. Jeffrey D. Zahn
And approved by

_____

_____

_____

_____

New Brunswick, New Jersey

October, 2015

ABSTRACT OF THE DISSERTATION

FLEXIBLE, IMPLANTABLE, MICRO-ELECTRODE PROBES WITH AN ULTRAFAST DEGRADING POLYMER COATING AS A TEMPORARY INSERTION AID FOR LONG TERM NEURONAL SIGNAL ACQUISITION

BY MENG-CHEN LO

Dissertation Director: Professor Jeffrey D. Zahn

Brain computer interfaces (BCI) establish communication between the brain and external devices by recording and decoding neural signals and using the signals to drive the devices. Implanted neural microprobes are one means of recording these signals. Despite the short term feasibility of currently available neural prosthetic devices, most of these devices suffer from long term gliosis. In order to address this challenge, it is hypothesized that smaller, more flexible probes that match the mechanical properties of brain tissue could allow better long term integration with neural tissue.

The goal of this work is to investigate and understand different device design parameters (e.g., size and material) that might affect brain tissue responses of a long term chronic intracortical neural probe. The miniaturized probe is coated with an ultrafast degrading Tyrosine-derived polycarbonate (E5005(2K)). The polymer is mechanically stiff, which allows it to act as a temporary insertion aid for the probes to penetrate tissue, yet has been

designed to degrade within several hours, leaving the flexible probes in place for high fidelity recording.

First, a fabrication process was developed incorporating both probe fabrication and polymer coating procedures. The probes were characterized to ensure consistent quality. Second, the probes were evaluated using an in-vivo rat model to assess glial tissue response via immunohistochemistry. Finally, the microfabrication process was expanded to electrically functionalize the probes via metallization, to create electrodes for signal recording.

In vivo animal study suggested that both polymer coating and probe sizes play roles in glial scar formation. The larger polymer coating devices introduced more severe glial scar response despite polymer degradation within a few hours post device implantation, which might result from the more severe insertion mechanical trauma. The experimental results also confirmed our hypothesis that the smaller probe/polymer coating devices performed better with minimal glial response compared to the larger probe/polymer coating devices in both short/long terms. Finally, we demonstrated the probe's recording feasibility using in vitro models, and showed that the electrode remained intact during polymer coating and degradation for the proper device operation.

In conclusion, the flexible microprobe with an ultrafast degrading polymer coating as an insertion aid demonstrates promising results to address challenges in electrode-cell

interface. Future work will evaluate the electrical recording performance of the miniaturized probe to confirm consistent signal quality while attenuating tissue reaction for prolonged device operation.

DEDICATION

To my parents, Jing-ming and hui-ju

For your unconditional love

Nothing is possible without your support

To my grandmother, Bi-xia

Thank you for watching me from far away

I feel your love everyday

ACKNOWLEDGEMENT

First, I would like to thank my advisor, Professor Jeffrey Zahn for providing me great amount of mentorship as well as independence for me to explore my own projects. He guided through many difficult times and kept me motivated for research and science. In the same way, I would like to thank my committee members, Professor David Shreiber, Professor Joachim Kohn and Dr. Danish Shabbar. They not only provided valuable comments and advise to this project but also challenged and trained me to be a better researcher.

I thank all the lab members at the BioMEMS and Microfluidics Laboratory for making the lab a fun place to work. I would like to specially thank Jack Zheng, Joe Fantuzzo, Joseph Sherba, Natalia Garcia, Mercedes Morales, Kiana Aran and Larry Sasso. Thank you for all your support and friendship.

I would also like to express my gratitude to members, who are in the collaborative labs, Hilton Kaplan, Shuwu Wang, Vinod Damondaran, Kevin Coffey and Davie Barker. I learned a great deal from all of you and thank you for the help on the project.

Thanks to all my friends for all the laughter that you brought me, Sagar , Connie , Max, Shihmin , Peishan , Pichu, Chiatien, Joni, Tara, Ariel , Tim and Poa. Special thanks to Alvin Chen for your care, companionship and patience for the past couple years.

Finally, I would like to acknowledge my parents, Hui-ju and Jing-ming and my two brothers, Stan and Dustin for providing me unconditional support and love. You gave me everything and nothing is possible without you.

TABLE OF CONTENTS

ABSTRACT OF THE DISSERTATION ii

DEDICATION v

ACKNOWLEDGEMENT vi

TABLE OF CONTENTS vii

LIST OF TABLES xii

LIST OF FIGURES xiii

LIST OF EQUATIONS xxvii

CHAPTER 1 INTRODUCTION 1

1.1 Brain computer interface 1

1.2 Hypothesis and Research objective 4

1.3 Dissertation overview 5

CHAPTER 2 BACKGROUND AND SIGNIFICANCE 7

2.1 Intracortical neural probes micromachining technologies 7

2.2 Tissue reaction to neural implants 11

2.3 Strategies to improve the electrode-cell interface 14

2.3.1 Biochemical approaches to improve electrode-cell interface 14

2.3.2 Device design parameters to improve electrode-cell interface ...17

2.4 Insertion aids for miniaturized and flexible neural probes 19

2.5 Tyrosine-derived polycarbonates as an insertion shuttle for neural probe implantation 21

CHAPTER 3 DEVICE FABRICATION AND CHARACTERIZAION 24

3.1 Overview.....24

3.2 Device design and fabrication.....25

3.2.1 Tyrosine-derived polycarbonate 25

3.2.2 Design criteria of the polymer coated probe.....26

3.2.3 Polymer coated SU-8 probe fabrication procedure.....34

3.3 Device characterization.....40

3.3.1 Mechanical testing of the coated probes.....40

3.3.2 Chemical characterization of the coated probes 46

3.3.2.1 Polymer erosion profile in PBS 46

3.3.2.2 Polymer erosion profile in a brain tissue phantom 48

3.4 Extended polymer coated parylene probe fabrication procedure 53

3.4.1 Parylene deposition procedure.....53

3.4.2 Fabrication process for a parylene probe coated with the ultrafast degrading polymer 54

CHAPTER 4 IN VIVO ANIMAL STUDY 58

4.1 Overview 58

4.2 Materials and Methods 59

4.2.1 Experimental design and device selection 59

4.2.2 Surgical procedure 63

4.2.3 Tissue processing and immunohistochemistry 65

4.2.4 Imaging protocol 69

4.2.5 Image and data analysis 72

4.3 Results and discussion 76

4.3.1 Preliminary control experiment 76

4.3.2 Probe candidate implantation experiment 83

4.3.2.1 Glial cell response – Astrocyte 83

4.3.2.2 Glial cell response – Microglia 92

4.3.2.3 Discussion 100

CHAPTER 5 DEVICE FUNCTIONALIZATION 107

5.1 Overview 107

5.2 Functionalized polymer coated parylene probe fabrication.....108

5.2.1 Electrical considerations for the probe design.....108

5.2.2 Functional probe fabrication procedure.....109

5.3 Functionalized polymer coated parylene probe characterization.....116

5.3.1 Physical examination of the functional parylene probe.....116

5.3.2 Preliminary packaging design for the functional probe.....119

5.4 In vitro electrical characterization for the functionalized microprobes 120

5.4.1 Experimental methods.....120

5.4.2 Phase 1: The functional probe operational verification.....122

5.4.3 Phase 2: Polymer degradation characterization.....129

CHAPTER 6 CONCLUSION AND FUTURE WORK.....132

APPEDIX A ANIMAL STUDY.....138

A.1 Individual device intensity vs. time points (GFAP Staining).....138

A.2 Normalized intensity vs. distance from the center of the implantation site (GFAP staining).....141

A.3 Individual device intensity vs. time points (Iba-1 Staining).....146

A.4 Normalized intensity vs. Distance from the center of the implantation site (Iba-1 staining).....149

A.5 Relationship between astrocyte and microglia for each device at different time points.....155

BIBLIOGRAPHY.....158

LIST OF TABLES

Table 3-1: Insertion success rate for uncoated SU-8 probe (40 μm wide, 10 μm thick and 3 mm long) and E5005(2K) coated SU-8 probe (100 μm wide, 100 μm thick and 3.5 mm long) 45

Table 4-1: Polymer (E5005(2K)) coated parylene probe candidate for the animal study.....63

Table 4-2: Immunohistochemistry staining protocol. Each depth included three consecutive slices stained with different cell types. Slice one stained astrocytes and endothelial cells. Slice two stained neurons. Slice three stained microglia and all nuclei.....67

LIST OF FIGURES

Figure 1-1: (A) Operating procedure of a BCI system. (B) Recording locations between Electroencephalography (EEG), Electrocorticography (ECoG) and local field potential (LFPs) and single unit recordings[117].....3

Figure 2-1: (Left) The SEM image of a planar Michigan probe array[118]. (Right) The SEM image of the three dimensional Utah array[12].....10

Figure 2-2: Schematic of the acute and chronic tissue response post device implantation. (A) Acute tissue response: disruption of blood vessels releases erythrocytes, clotting factors, and inflammatory factors that facilitate macrophage recruitment as well as microglia activation. (B) Chronic tissue response: formation of a glial cell layer composed of microglia and astrocytes that isolates neuron from the neural implant[6].....12

Figure 2-3: Time course of glial scar formation at 4 different time points post-implantation using GFAP staining[36].....14

Figure 2-4: Images of β-tubulin (green) for neurons and Hoechst (blue) for cells other than neurons 4 weeks post device implantation. (A) The L1 modified probe (B) The controlled probe without modification. Scale bar : 100 μm[53].....15

Figure 2-5: Images of GFAP staining for astrocytes 1 week and 4 week post device implantation comparing uncoated and DEX coated probes. Scale bar : 100 μm[56].16

Figure 2-6: Histological analysis comparing standard Michigan probe (Mi probe) with microthread electrodes (MTE) using GFAP (astrocytes) and Iba-1(microglia) staining. The animal was sacrificed two weeks after devices implantation. Less astrocytes can be observed in the MTE than the traditional Michgan probe. More microglia can be observed near the traditional michigan probe implatation site compared to the MTE[68].....18

Figure 2-7: Images of various insertion shuttles for flexible probe implantation. (A) Poly(ethylene glycol)(PEG) coating[81]. (B) Poly(D,L-lactide-co-glycolide) (PLGA) insertion shuttle[84]. (C) Carboxyl-methylcellulose (CMC) insertion shuttle[85]. 20

Figure 2-8: Time lapse fluorescent images of thin polyimide films coated with (a) fast-degrading polymer (E5005(2K)) and (b) slow-degrading polymer (E1001(1K))[107]. The probes were inserted into agarose gel. 22

Figure 2-9: Histological analysis comparing uncoated the microriwes with polymer coated microwires using GFAP (astrocytes (yellow)) , Iba-1(microglia(blue)) and Nissl (neurons (green)) staining[107]. The animal was sacrificed 1 week after device implanation. Scale bar : 100 μm. 23

Figure 3-1: Chemical structure of the tyrosine-derived polycarbonate (Poly (DTE-co XX%DT-co-YY%PEG (MW)).....26

Figure 3-2: Probe buckling force vs. shank widths and thickness. (Length: 3.5 mm; Thickness: 100 μm and 65 μm) 29

Figure 3-3: Probe buckling force vs. shank width and length. (Thickness: 100 µm; Length: 3.5 mm, 4 mm and 5 mm) 29

Figure 3-4: Probe bending force vs. shank width and length**.** (Thickness: 100 µm; Length: 3.5 mm, 4 mm and 5 mm) 32

Figure 3-5: Probe bending force vs. shank width and thickness. (Thickness: 65 µm, 100 µm; Length: 3.5 mm 33

Figure 3-6: (Left) Polymer coating process. The polymer solution was introduced at the reservoir. Solvent evaporated and polymer solidified from the edge of the mold , eventually filling the whole cavity. (Right) Packaging method for the polymer coated probes. 36

Figure 3-7: Schematic of the polymer coated probe fabrication process. a) A thin layer of PDMS (~65 µm) is spin coated on to a substrate. b) The probe geometry is patterned on top of the PDMS layer. c) The SU-8 probe is aligned with the molding structure. d) Polymer solution is infused through the inlet of the mold using MIMIC technique and the polymer solvent is allowed to evaporate. e) The device is released from the substrate. f) The device is released from the molding structure. g) The device is lifted mechanically off from the PDMS substrate. 37

Figure 3-8: (a) SEM micrograph of a non-functional SU-8 probe. Probe dimension: 30 µm wide, 10 µm thick and 3 mm long. (b) Light microscope image of the coated probe. (c) SEM micrograph of the coated probe. Device dimension: polymer shank: 200 µm wide, 100 µm thick and 3.5 mm long. SU-8 probe: 30 µm wide, 20 µm thick and 3 mm long 39

Figure 3-9: Schematic of the mechanical testing apparatus 42

Figure 3-10: Experimental and theoretical buckling force measurements vs. different coating width. Device dimension: polymer shank: 100 µm thick and 3.5 mm long. SU8-probe: 30 µm wide, 20 µm thick and 3 mm long.....44

Figure 3-11: Relative mass retention of the E5005(2K) coated probe with different probe candidates. Device dimension: polymer shank: 100 or 150 µm wide, 100 µm thick and 3.5 mm long. SU8-probe: 30 µm wide, 20 µm thick and 3 mm long. ...48

Figure 3-12: Time lapse fluorescent images of SU-8 probe coated with (a) E5005(2K) and (b) E1001(1K). Device dimension: (a) polymer shank: 100 µm wide, 100 µm thick and 3.5 mm long. SU8-probe: 30 µm wide, 20 µm thick and 3 mm long. (b) Polymer shank: 200 µm wide, 100 µm thick and 3.5 mm long. SU-8 probe: 30 µm wide, 20 µm thick and 3 mm long. (c) Intensity profile for E5005(2K) coated probe over different time points from the center of the probe.(d) Intensity profile for E1001(1K) coated probe over different time points from the center of the probe.....52

Figure 3-13: Schematic illustration of parylene deposition process.....54

Figure 3-14: Parylene probe fabrication and polymer coating procedure. First, a thin layer of parylene was deposited. A thin aluminum mask layer that defined the probe geometry was deposited onto the top of the parylene layer through lift-off methods. Oxygen plasma etch was performed to pattern the probe. The mask layer was dissolved with a chemical etchant to complete probe fabrication. The polymer coating procedure was the same as described in the previous section (Chapter 3.2.2). The probe was coated with the polymer though micromolding in capillaries and the whole device was dried and released from the substrate. 56

Figure 3-15: SEM micrograph of (a) a non-functional parylene probe. (b) a polymer coated probe (c) a polymer coated probe from the device backside. Device dimension: polymer shank: 100 µm wide, 100 µm thick and 4 mm long. Parylene probe: 30 µm wide, 5 µm thick and 3.5 mm long.....57

Figure 4-1: (Left) The customized surgical holder with 10 devices fixed on it. (Right) The customized surgical holder and headstage incorporated with a standard stereotaxic station.....60

Figure 4-2: The experimental design of different device types and their fixation locations on the surgical holder. w: microwires dimension : 50 µm in diameter and 4 mm long. Polymer coating dimensions : various widths and heights as indicated ; 4 mm long. 61

Figure 4-3: Surgical procedure for the animal study. Two craniotomies were drilled. 10 probes with different dimensions were implanted simultaneously via the customed designed surgical holder. Dental cement was used to fix the surgical holder and the wound was sutured. The animal was placed on warm heat pad until recovery from anesthesia. 64

Figure 4-4: Location and dimension of the two craniotomy holes and the 10 probes (Table 4-1 for reference) with different dimensions. a= 4 mm ; b=4 mm; c= 6 mm; d=3 mm. 65

Figure 4-5: Fluorescent spectra of different secondary antbodies conjugated with different cell types and spectra range of different imaging filters (DAPI; GFP; RFP; Cy5).....68

Figure 4-6: Representative images of tissue staining with different cell types (Astrocytes, Microglia, Neurons and Cell nuclei). 69

Figure 4-7: Representative image of a montage brain slices. Sample ID: 72-hour control animal at 2 mm deep from the surface of the brain stained with GFAP (astrocytes). R and L indicated right hemisphere and left hemisphere brain for the animal.....69

Figure 4-8: Representative image of 1) a montage of brain slices with a grid application for implantation site identification. 2) Magnified images of several implantation sites for downstream image analysis process. Sample ID: 72-hour control animal at 2 mm deep from the surface of the brain stained with GFAP (astrocytes). R and L indicated right hemisphere and left hemisphere brain for the animal.....71

Figure 4-9: Rotational intensity sweep profile anaysis. The implantation site was ideintified through thresholding and the centroid was identified. An end point reaching the undamaged area was defined and an intensity profile along the line was obtained. The same analysis was repeated by rotating the line with small angle step in a full circle. The intesity values were averaged and plotted with respect to the distance from the center of the implantation site. 73

Figure 4-10: Represensative data showing normalized intensity vs. distance from the center of the implantation site. The intensity values were normalized by the undamaged area , which was denoted with a value of 1. 74

Figure 4-11: Represensative data showing normalized intensity vs. distance from the center of the implantation site. Area under the cruve above was obtained to represent the amount of cells that show comparably higher fluorescence than the undamaged area within the region of the interest. 75

Figure 4-12: GFAP staining (for astrocytes) images for three difference devices (the microwire, slow-degrading polymer shank and fast-degrading polymer shank) at two different time points (72 hour and 4 week post device implantation). Device dimension: The microwire: 50 μm in diameter and 4 mm long. The polymer shanks: 200 μm wide, 200 μm thick and 4 mm long. 77

Figure 4-13: The wound size for the three devices (the microwire, slow-degrading polymer shank and fast-degrading polymer shank) at two different time points (72 hour and 4 week post device implantation). Device dimension: The microwire: 50 μm in diameter and 4 mm long. The polymer shanks: 200 μm wide, 200 μm thick and 4 mm long. 77

Figure 4-14: The intensity over the distance from the center of the implantation site with GFAP staining for three different devices (the microwire, slow-degrading polymer shank and fast-degrading polymer shank) at two different time points (72 hour and 4 week post device implantation). Device dimension: The microwire: 50 μm in diameter and 4 mm long. The polymer shanks: 200 μm wide, 200 μm thick and 4 mm long. 79

Figure 4-15: Iba-1 staining (for microglia) images for three different devices (the microwire, slow-degrading polymer shank and fast-degrading polymer shank) at two different time points (72 hour and 4 week post device implantation). Device dimension: The microwire: 50 μm in diameter and 4 mm long. The polymer shanks: 200 μm wide, 200 μm thick and 4 mm long. 81

Figure 4-16: The intensity over the distance from the center of the implantation site with Iba-1 staining for the microwire, slow-degrading polymer shank and fast-degrading polymer shank at two different time points (72 hour and 4 week post device implantation). Device dimension: The microwire: 50 μm in diameter and 4 mm long. The polymer shanks: 200 μm wide, 200 μm thick and 4 mm long. 82

Figure 4-17: Normalized intensity of GFAP staining vs. different devices/rats 72 hour post implantation. Dashed line: statistical significance ($p<0.05$) between animals within an experimental group. Solid line: significance between devices across experimental groups ($p<0.05$). Scale bar : 200 μm.....84

Figure 4-18: Normalized intensity of GFAP staining vs. different devices/rats 10 days post implantation Dashed line: statistical significance ($p<0.05$) between animals within an experimental group. Solid line: significance between devices across experimental groups ($p<0.05$). Scale bar : 200 μm.....85

.....85

Figure 4-19: Normalized intensity of GFAP staining vs. different devices/rats 3 weeks post implantation Dashed line: statistical significance ($p<0.05$) between animals within an experimental group. Solid line: significance between devices across experimental groups ($p<0.05$). Scale bar : 200 μm.....86

.....86

Figure 4-20: Normalized intensity of GFAP staining vs. different devices/rats 7 weeks post implantation. Dashed line: statistical significance ($p<0.05$) between animals within an experimental group. Solid line: significance between devices between experimental groups ($p<0.05$). Scale bar : 200 μm. 87

Figure 4-21: Normalized intensity of GFAP staining vs. different devices/rats 12 weeks post implantation. Dashed line: statistical significance ($p<0.05$) between animals within an experimental group. Solid line: significance between devices across experimental groups ($p<0.05$). Scale bar : 200 μm.....89

Figure 4-22: Normalized intensity of GFAP staining vs. different devices/rats 24 weeks post implantation. Dashed line: statistical significance ($p<0.05$) between animals within an experimental group. Solid line: significance between devices across experimental groups ($p<0.05$). Scale bar : 200 μm.....90

Figure 4-23: Normalized intensity of GFAP staining vs. different devices at different time points. Solid line: significance between different time points ($p<0.05$).....91

Figure 4-24: Normalized intensity of Iba-1 staining vs. different devices/rats 72 hours post implantation. Scale bar : 200 μm. 93

Figure 4-25: Normalized intensity of Iba-1 staining vs. different devices/rats 10 days post implantation. Scale bar : 200 μm. 94

Figure 4-26: Normalized intensity of Iba-1 staining vs. different devices/rats 3 weeks post implantation. Scale bar : 200 μm. Dashed line: statistical significance ($p<0.05$) between animals. 95

Figure 4-27: Normalized intensity of Iba-1 staining vs. different devices/rats 7 weeks post implantation. Scale bar : 200 μm. Dashed line: statistical significance ($p<0.05$) between animals. 96

Figure 4-28: Normalized intensity of Iba-1 staining vs. different devices/rats 12 weeks post implantation. Scale bar : 200 μm. 96

Figure 4-29: Normalized intensity of Iba-1 staining vs. different devices/rats 24 weeks post implantation. Solid line: significance between devices ($p<0.05$). Scale bar : 200 μm. 97

Figure 4-30: Normalized intensity of Iba-1 staining vs. different devices at different time points. Solid line: significance between different time points ($p<0.05$). 98

Figure 4-31: The relationship between microglia and astrocytes at different time points for different devices. 100

Figure 4-32: The brain defect caused by large craniotomy holes for device implantation. 106

Figure 5-1: Fabrication process of the parylene functional microelectrode. A thin layer of parylene film (5 μm) was deposited onto a substrate. Ti/Pt electrodes were defined using the lift-off method. Another layer of parylene film (2.5 μm) was deposited to insulate the electrical traces. An aluminum mask defined the probe geometry and patterned electrode openings/connecting pad. Finally, an oxygen plasma was used to etch the un-masked parylene and the aluminum mask was dissolved using an aluminum etchant. 109

Figure 5-2: Schematic of the mask layer defining (Top) the recording windows and the connection pad, and (Bottom) the probe geometry. The cross marks are alignment mark for aligning the probe with the electrode. Device dimension: The probe: 90 μm wide and 4 mm long. The recording window: 30 μm × 30 μm square. The connecting pad: 1 cm long and 1.5 mm wide. 113

Figure 5-3: Oxygen plasma etching of a parylene layer. It is an isotropic process that removes material at an equal rate in all directions.....114

Figure 5-4: SEM image of a parylene probe masked by an aluminum layer post oxgygen plasma etching treatment. The vertical etch rate is ~7.5 μm and horizontal etch rate is ~2 μm at 250W for 30 minutes.....115

Figure 5-5: Bright field microscopy images of the funationalized probe with connecting traces, a recording window and the connecting pad for outer electrical instrumentation incorporation. Device dimension : The probe: 90 μm wide, 5 μm thick and 4 mm long. The recording window: 30 μm x 30 μm square. The connecting pad: 1 cm long and 1.5 mm wide. 117

Figure 5-6: A represensative mask design with multiple electrodes patterned along a single shank of the probe. Each electrode requires individual trace connection for signal delivery to the outer data acquisition system. 118

Figure 5-7: The SEM micrograph of a polymer coated functional probe. Device dimension: The probe: 90 μm wide, 5 μm thick and 3.5 mm long. The polymer coating: 100 μm wide, 100 μm thick and 4 mm long. 118

Figure 5-8: Photograph of a packaged functional probe. The zero-insertion-force (ZIF) connector was used to incorporate parylene probe with electrcal pins for interfacing. 119

Figure 5-9: Experimental set up for the in vitro probe electrical characterization.121

Figure 5-10: The conductivity experiment for the functional parylene probes. The electrode was stimulated at 200 mV @ 45 kHz within different solutions (100, 500 and 1000 μS/cm) and current readings were recorded. 123

Figure 5-11: The I-V curve experiment. The electrode was stimulated at an increasing voltage recipe (500-600 mV with 10 mV increments; 600-1000 mV with 100 mV increments) at 1 kHz and current readings were recording. The experiments were also repeated within solutions of different condictivities (1000, 500 and 100 μS/cm).....124

Figure 5-12: The impedance magnitude vs. frequncy within different solutions. The electrode was stimulated at various voltage (500 mV for 1000, 500 and 100 μS/cm solutions and 50 mV for PBS solutions). The freqeuncy was swept from 100 Hz to 10 kHz and the impedance was monitored. 126

Figure 5-13: (A) The I-V curve experiment within the PBS solution and 0.5% agarose gel. The electrode was stimulated with a steadily increasing voltage (5-30 mV in 5 mV increments; 30-100 mV in 10 mV increments) at 1 kHz. (B) The impedance magnitude vs. frequncy within PBS and 0.5% agarose gel. The electrode was stimulated at 50 mV. The freqeuncy was swept from 100 Hz to 1200 kHz and the impedance was monitored.....128

Figure 5-14: Impedance vs. time during polymer degrading/erosion. Device dimension: The probe: 90 μm wide and 3.5 mm long. The polymer coating: 100 μm wide, 100 μm thick and 4 mm long. 131

LIST OF EQUATIONS

Equation 1 $F = \frac{\pi^2 EI}{(KL^2)}$ 28

Equation 2 $I = \frac{(bh^3)}{12}$ 28

Equation 3 $F = \frac{\pi^2 Ebh^3}{5.88L^2}$ 28

Equation 4 $\sigma = \frac{Mc}{I}$ 31

Equation 5 $F = \frac{\sigma yI}{cL}$ 31

Equation 6 $F = \frac{\sigma bh^2}{6L}$ 31

CHAPTER 1 INTRODUCTION

1.1 Brain computer interface

Brain computer interface (BCI) is a method to establish the communication between brain neural signals and external devices without actual physical pathways through the peripheral neural system and muscles[1,2]. There has been a rising interest in BCI to assist people who suffer from nervous system impairments (e.g., spinal cord injury , neurodegenerative diseases and demyelinating diseases) by replacing the lost sensory and motor functions with the external neural prosthetic devices[2–5].

There are 4 essential elements for BCI[6,7]: (1) neural signals in the form of neuron depolarization are recorded from the brain, (2) the electrical signals are decoded and processed using translational algorithms to covert the recorded neural signals into computational compatible signals, (3) device commands are then generated and output from the BCI prosthetic devices and finally (4) operating protocols and commands are sent to peripheral operators or the patient to obtain feedback or generate movements (Figure 1-1[1](A)). The first step of the BCI system is signal recording. It is therefore essential to ensure BCI systems are capable of obtaining brain signals efficiently (e.g. high signal to noise ratio) over a long period of time for consistent and reliable device operation.

[1]Reprinted from The Lancet Neurobiology, Vol 7, Daly,J.J. & Wolpaw, J. R. Brain-computer interfaces in neurological rehabilitation. Page 1032–1043,.Copyright (2008), with permission from Elsevier.

There are different recording modalities which can be used, each depending on electrode placement (Figure 1-1(B)). There is a tradeoff between electrode placement with the cortical spatial resolution and recording fidelity (e.g., signal to noise ratio, spectral frequencies recorded, etc.) which in turn affects the types of device commands which can be generated for assistive devices. In general, the more invasive the recording modalities, the more precise the cortical homunculus recording domain is targeted, and higher quality recordings (e.g., single neuron recording) are obtained, allowing finer motor intent resolution to target specific movements. Electroencephalography (EEG) is a non-invasive recording modality, but it is the easiest and safest way to record neural signals. It records electrical signals from the scalp located 2-3 cm away from the surface of the cortex. However, research in EEG recording to determine motor intent estimated that ~6 cm^2 of cortical tissue must have synchronized intent in order to obtain a measurable potential on the scalp[8,9] and therefore EEG can only decode low spatial and spectral resolutions such as gross limb movements. Electrocorticography (ECoG) records signals around 0.5 cm from the cortex surface so it can improve the spatial resolution of motor intent to the order of mm and therefore offers better efficacy[10]. Recording from single neurons within the cortical layer has been identified as the most optimal method to capture neural signals due to its high spatial resolution and can help to generate a more accurate understanding of motor intent and finer movements or higher levels of patient feedback [7,11].

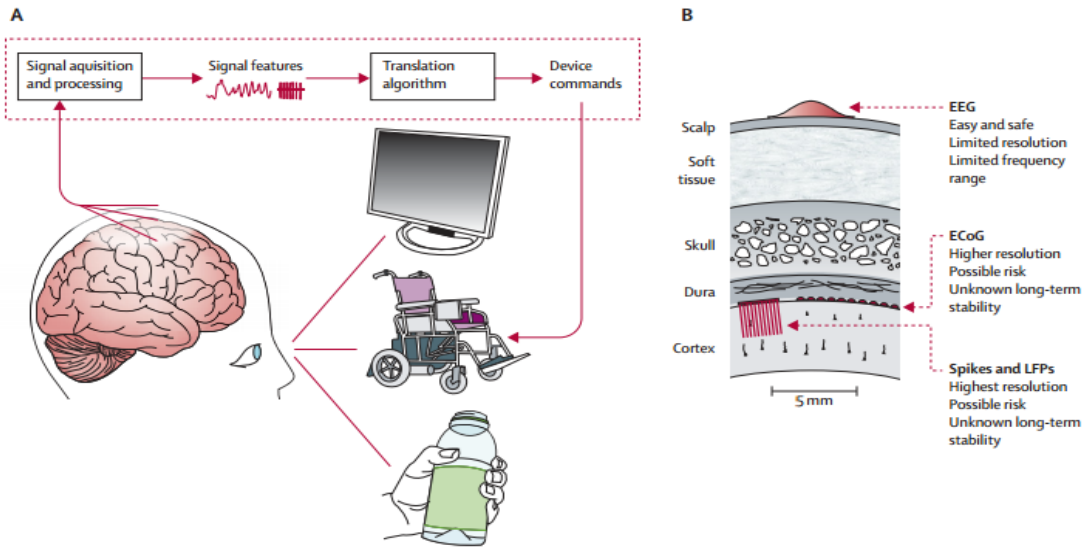

Figure 1-1: (A) Operating procedure of a BCI system. (B) Recording locations between Electroencephalography (EEG), Electrocorticography (ECoG) and local field potential (LFPs) and single unit recordings[136].

Due to the advantages of the intracortical neural probes described above, there has been a wealth of research in developing penetrating neural microelectrode for long term BCI operations. Several considerations which must be taken into account during the neural probe development are probe dimensions, microfabrication process, electrode dimensions and the electrode-cell interfaces. Despite several decades of chronic neural probe development, electrode failure is still a major challenge that prevents intracortical neural probes from clinical applications in human. One of the most distinctive reasons for electrode failures is the electrode-cell interface disruption. Some examples include tissue inflammation, glial scar formation and neural death around device implantation sites (detailed discussion in Chapter 2). The disruption can cause inconsistent signal quality,

electrode breakage which eventually limits the probe's functionality. Most conventional intracortical electrodes (e.g., microwires, Utah arrays or Michigan arrays) can sustain recording performance for couple months (6-12 months with good signal to noise ratio) before the signal quality begins to drop significantly approximately 18-24 months after device implantation[12–14] and eventually are incapable of acquiring signals.

The decreasing functionality of the intracortical neural probes over time causes various issues. First, BCI devices are programmed and operated based on neural signal recorded from the subject. Inconsistent signal acquisitions would affect BCI performance and operational parameters have to be adjusted downstream (signal processing algorithms, and prosthetic controls, etc) to maintain functionality. Second, intracortical neural probes require surgeries for device implantation. If the device loses its function and needs to be replaced, it not only costs time/money but also affects the patients' quality of life. Therefore, there is a need to develop neural probe technology that is capable of acquiring neuronal signal consistently for long term BCI operation. Furthermore, it is beneficial to understand how different device design parameters attenuate tissue response for prolonged device life time.

1.2 Hypothesis and Research objective

The goal of this work is to develop a new chronic intracortical microelectrode neural probe and investigate the fundamental probe design parameters that might affect long term brain tissue response. The size and material of neural probes have been identified

as two possible design factors that might affect the long term device performance. It is hypothesized that a smaller, more flexible probe would allow better long term integration with neural tissue by limiting the mechanical disruption of tissue upon device implantation as well as being flexible enough to deform with the surrounding tissue during cell movements. However, smaller, more flexible probes inherently lack the mechanical strength to penetrate into tissue on their own which limits their ability to be effectively implanted. Therefore, the miniaturized probe is coated with an ultrafast degrading Tyrosine-derived polycarbonate (E5005(2K)). The polymer is mechanically stiff which allows it to act as a temporary insertion aid to penetrate tissue yet has been designed to degrade within several hours leaving the flexible probes in place for high fidelity recordings.

1.3 Dissertation overview

The dissertation is organized with the current chapter introducing overview of the brain computer interface, intracortical neural probe advantages over other technology in BCI applications, motivation of this work in developing a chronic neural microelectrode as well as project hypothesis to investigate different design parameters (probe size and material) in tissue response progression. I propose to develop a miniaturized and flexible microelectrode probe coated with an ultrafast degrading polymer as a temporary insertion aid for long term neuronal signal acquisition.

Chapter 2 presents background information in cortical neural probe micromachining technologies. I also discuss the underlying mechanism for tissue response towards penetrating devices and what are the current strategies being investigated to improve the electrode-cell interface.

Chapter 3 describes the fabrication procedure of the non-functional SU-8 and parylene microprobes coated with an ultrafast degrading tyrosine-derived polycarbonate. The devices were characterized to ensure consistent quality for an in vivo animal implantation study.

Chapter 4 describes the animal study to evaluate the polymer coated probes. The study was performed by implanting probe candidates with varying probe/coating dimensions into rat brains. The rat brains were harvested at different time points and the tissue damage was evaluated. Different cell types were immunolabeled and the effects of different design parameters on acute/chronic tissue responses were investigated.

Chapter 5 describes the fabrication procedure to functionalize the microprobe by metallization. The functional devices were electrically characterized in vitro to ensure operational feasibility.

Chapter 6 summarizes and discusses results obtained from the project and also proposes ideas for future research directions.

CHAPTER 2 BACKGROUND AND SIGNIFICANCE

Note: Part of this chapter is reproduced from the following publication:

Lo, M. *et al.* Coating flexible probes with an ultrafast degrading polymer to aid in tissue insertion. *Biomed. Microdevices* **17,** 9927 (2015)[106].

2.1 Intracortical neural probes micromachining technologies

The major goals in the development of multi-electrode arrays for neural signal recordings include the ability to obtain high quality signals from recording sites allowing long term implantation, ultimately over decades of recording time, to enable lifetime use of a BCI prosthetic device. There are several considerations which must be taking into account during neural probe development such as probe dimensions, microfabrication process, electrode dimensions and the electrode-cell interfaces.

Benjamin Franklin (1757) first suggested the use of electrical current as an possible modality to treat paralysis[15]. However, it was not extensively explored until the 1930's when Hodgkin and Huxley demonstrated the first work recording action potentials within neural fibers[16] and later in 1952 when the nerve membrane's ability to conduct nerve electrical impulses quantitatively illustrated[17]. Beginning in the 1950s, many of the pioneering neural recording studies used miniaturized metal wires made from platinum, iridium, copper or stainless steel 30 to 50 μm in diameter, coupled with a Teflon or polyimide coating as an insulation layer with the tips exposed for recordings[18–20]. Brindley and Lewin implanted arrays of electrodes on the surface of the visual cortex of a blind

patient for stimulation and demonstrated the feasibility to partially recover the patient's visual functions[21]. However, this work also suggested the development of intracortical microelectrodes for this application due to the limited control of surface stimulation that sometimes caused an unpredictable response in patients. Since then, there has been extensive research into the use of metal microelectrodes arrays to assist handicapped people such as cochlear implants to restore auditory functions in the deaf[22], deep-brain stimulators for controlling tremors in patients with Parkinson's disease[23] and visual implants for restoring eyesight in the blind[21]. The advantage of using microwires is the easy and straightforward fabrication process. However, each wire is a rather large individual recording unit so it is difficult to measure single neuron activity, create a high density multi-electrode array, and these probes create a large amount of tissue damage during insertion which ultimately limits their use as a neural probe. Moreover, each metal wire only yields one recording site and therefore it is difficult to insert large number of probes accurately into brain tissue to increase the device efficacy. For these reasons, microwire arrays have found more clinical success in the use for neural stimulation rather than neural recordings.

In order to address the limitations of metal microwires described previously, silicon based neural probes have been explored as an alternative to microwire electrodes. In the late 1970s, Wise and Angell used microfabrication techniques to demonstrate the first silicon-based neural probes for signal recordings[24]. Silicon microfabrication processes provides fine control over the probe and electrode size, shape, spacing and even allows

multiple recording sites to be fabricated within one device to increase the device efficacy. One of the well known silicon-based probes that is currently commercialized and can be purchased for research use is the Michigan probe developed by Wise and Najafi (1990)[25] (Figure 2-1[2]). The Michigan probe is a planar electrode array with a thin silicon shank and each of the electrodes is about 2 mm long, 100 µm wide and 15 µm thick. The Michigan probes enable a high density of electrodes per shank that further improve signal acquisition efficacy. However, due to the fabrication limitations where the thickness of the shank is 15 µm, many of the Michigan probes induce mechanical tissue disruption upon insertion which leads to a serious tissue response due to mechanical trauma as well as low signal resolution due to probe mispositioning. Another commonly used and investigated neural probe is the Utah electrode arrays developed by Normann et al. (1992)[26] (Figure 2-1[3]). The Utah arrays are fabricated from a block of silicon through cutting, doping, etching and heat treatment to yield a three-dimensional spiked array geometry. However, the recording abilities of the Utah arrays are constrained due to fabrication process so that electrode lengths cannot be longer than 1.5 mm limiting the electrode recoding ranges. Both the planar (Michigan probes) and three dimensional (Utah arrays) silicon based probes have been developed and explored intensively because they provide efficient signal recordings and have the ability to precisely record signals at well defined locations along the probe to

---

[2] © 2001 IEEE. Reprinted, with permission, from Bai, Q. & Wise, K. D. Single-unit neural recording with active microelectrode arrays. *IEEE Trans. Biomed. Eng.* August, 2001

[3] Reprinted from Journal of Neuroscience Methods, Vol 82, Rousche, P. J. & Normann, R. A. Chronic recording capability of the Utah Intracortical Electrode Array in cat sensory cortex. Page 1-15, Copyright (1998), with permission from Elsevier.

allow analysis of motor intent for complex activities[27–32]. However, silicon based probes are extremely rigid due to high Young's modulus of silicon. The implantation of such devices usually lead to serious mechanical trauma that induce a severe acute tissue response and later on chronic gliosis formation that limit the long term utilization (discussed in Chapter 2.2).

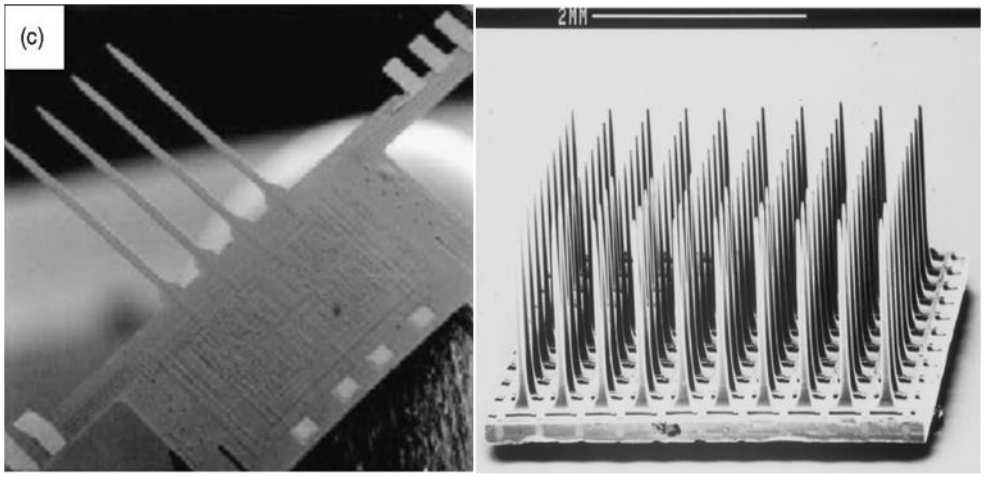

Figure 2-1: (Left) The SEM image of a planar Michigan probe array[137]. (Right) The SEM image of the three dimensional Utah array[12].

More recently , Meyer, Beutel and Stieglitz (1997) suggested the fabrication of flexible probes which can minimize tissue responses[33]. Since then, flexible neural probes have also been fabricated with more biocompatible materials such as polyimide or poly(p-xylylene) (parylene) to replace or improve the recordings abilities of the silicon based probes[34,35]. These types of polymer probes are usually less rigid compared to silicon-based probes, and have better long term biocompatibility. However, they usually suffer from

mechanical failure when implanting into tissues unless very large designs (>200 μm diameter) are used.

2.2 Tissue reaction to neural implants

Despite the feasibility for short term neural recordings (~2-6 weeks) [12,13] from these different types of probes, most of the devices ultimately fail due to disruption of the electrode-cell interface by the foreign body response, which alters the recording feasibility over time until the probes are finally no longer able to acquire stable and consistent signals[36–42]. Astrocytes and microglia are two glial cell populations involved in the neural tissue response. Astrocytes make up 30 to 60% of glial cells in the central nervous system (CNS)[43]. Astrocytes are the main component when a glial scar forms. They express the filamentous glial fibrillary acidic protein (GFAP) which is considered the specific marker for astrocyte activation. Microglia cells are another major cell type involved in the tissue response. The microglia cells initiate the wound healing process through the secretion of various soluble factors which activate astrocytes, other microglia, immune cells and cellular pathways. These two cellular populations modulate the implant response and lead to various cellular responses in response to brain tissue injuries.

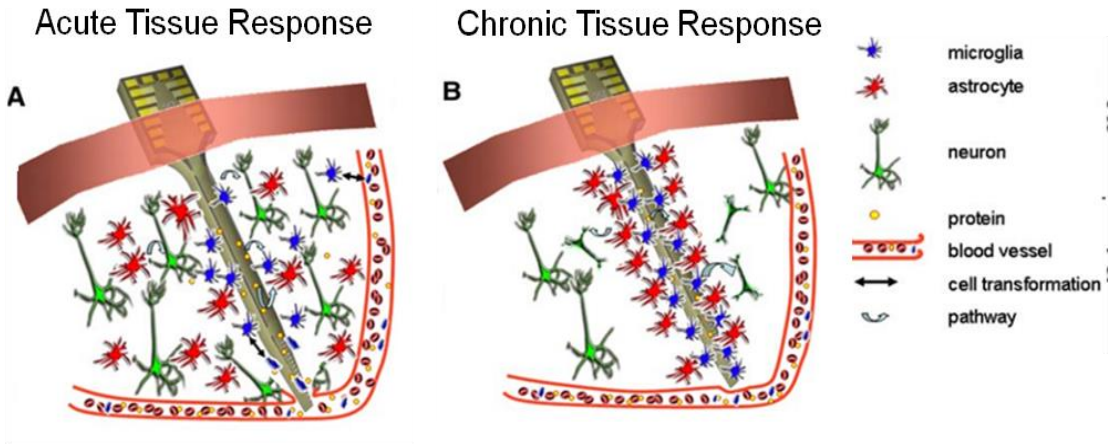

Figure 2-2: Schematic of the acute and chronic tissue response post device implantation. (A) Acute tissue response: disruption of blood vessels releases erythrocytes, clotting factors, and inflammatory factors that facilitate macrophage recruitment as well as microglia activation. (B) Chronic tissue response: formation of a glial cell layer composed of microglia and astrocytes that isolates neuron from the neural implant[6].

The two forms of tissue response to probe insertion are as follows (Figure 2-2[4]): (1) *acute* activation of microglia and astrocytes[36,37]; (2) *chronic* glial scar formation[44,45]. When neural probes are inserted into brain tissue, the mechanical trauma causes cellular damage and disruption of blood vessels that induces astrocyte/microglia activation[46–48], which interfere with microcirculation. Disruption of blood vessels releases erythrocytes, clotting factors, and inflammatory factors that facilitate macrophage recruitment[36,49]. Activated microglia, as early as 1 day post-implantation, will try to phagocytose the

[4] Reprinted from Neuron, Vol 52, Schwartz, A. B., Cui, X. T., Weber, D. J. & Moran, D. W. Brain-controlled interfaces: movement restoration with neural prosthetics. Page 205-220, Copyright (2006), with permission from Elsevier.

implant foreign matter for degradation[46,47]. This acute inflammatory response which may interrupt probe performance due to a unstable brain environments usually subsides within couple weeks post probe insertion[47,50].

After the acute tissue response subsides, a chronic foreign body response can then be observed, presumably aggravated by continual shear forces of the brain moving relative to the rigid probes[43,45]. Most functional probe failures result from this long term CNS response, in which gliosis forms an encapsulation layer that isolates the electrodes from the adjacent neural cells[12,36,42,45]. Figure 2-3[5] displays a typical observation of glial scar formation for most neural implants at various time points by using GFAP staining to monitor astrocyte activation. By week 2, the area of the activated astrocytes is spread out 500 to 600 μm around the probe insertion site. By week 4, the activated region has shrunk while the density of the astrocytes surrounding the implant increases. At week 6 to 12, there is the formation of a clear thick astrocytes layer surrounding the implant. This encapsulation electrically insulates the probes, impairs the devices by dramatically increasing their recording impedance [51,52], and decreasing the recording signal to noise ratio (SNR) as a consequence [39,42].

[5] Reprinted from Experimental Neurology, Vol 156, Turner, J. N. *et al.* Cerebral Astrocyte Response to Micromachined Silicon Implants. Page 33-49, Copyright (1999), with permission from Elsevier.

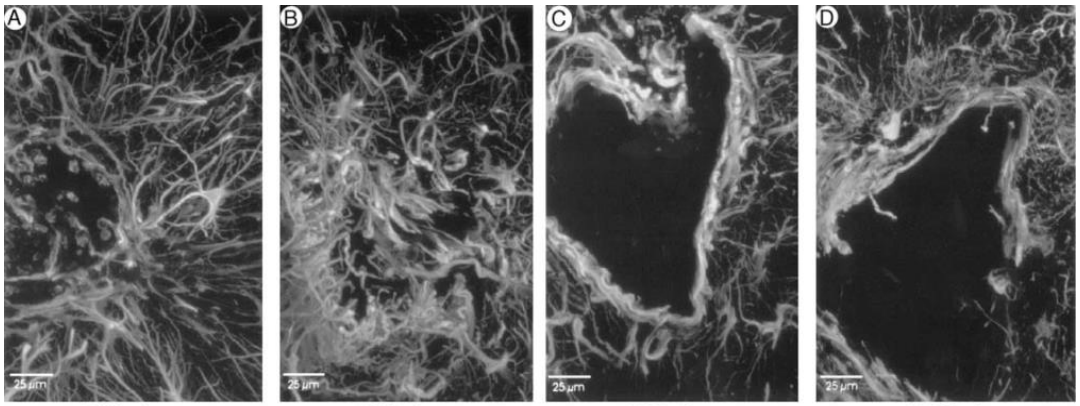

Figure 2-3: Time course of glial scar formation at 4 different time points post-implantation using GFAP staining[36].

2.3 Strategies to improve the electrode-cell interface

2.3.1 Biochemical approaches to improve electrode-cell interface

Various methods have been investigated to improve electrode-cell interfaces. Some research focuses on modifying commercially available probes with biochemical substances. Azemi et al. covalently immobilized neural adhesion molecules, L1, on the surface of a silicon-based neural probe[53]. L1 molecules are expressed in most neurons and are identified to promote neural outgrowth and guide neuron migration[54,55]. Results showed that the L1 modified neural probe not only lowered the glial cell activation but also promoted neuron attachments to the probe , which was a promising result to prolong device life time and obtain better signal quality due to easy electrode access to adjacent neurons (Figure 2-4[6]).

---

[6] Reprinted from Biomaterials, Vol 32, Azemi, E., Lagenaur, C. F. & Cui, X. T. The surface immobilization of the neural adhesion molecule L1 on neural probes and its effect on neuronal density and gliosis at the probe/tissue interface. Page 681-692, Copyright (2011), with permission from Elsevier.

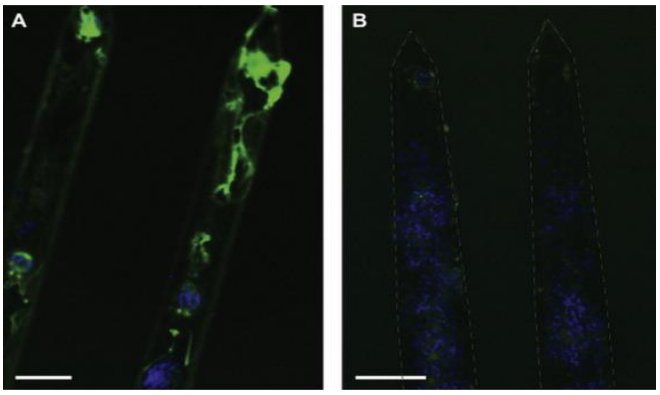

Figure 2-4: Images of β-tubulin (green) for neurons and Hoechst (blue) for cells other than neurons 4 weeks post device implantation. (A) The L1 modified probe (B) The controlled probe without modification. Scale bar : 100 μm[53].

Other applications include locally or systematic administration of anti-inflammatory drugs (e.g., Dexamethasone (DEX)[56–60], Flavopirido[61]). Zhong and Bellamkonda coated a micromachined silicon neural recording probe with DEX and evaluated glial cell behaviors using animal models. Figure 2-5[7] displays immunostaining images for astrocytes comparing uncoated and DEX coated Michigan probes at the 1 week and 4 week post device implantation. Astrocytes were more condense around the uncoated device than the DEX coated device at both the 1 and 4 week time points. This observation implied the addition of anti-inflammatory drug can help reduce glial cell activation and minimize astrocyte migration toward the implantation site, thereby improving the electrode-cell interface.

---

[7] Reprinted from Brain Research, Vol 1148, Zhong, Y. & Bellamkonda, R. V. Dexamethasone-coated neural probes elicit attenuated inflammatory response and neuronal loss compared to uncoated neural probes. Page 15-27, Copyright (2007), with permission from Elsevier.

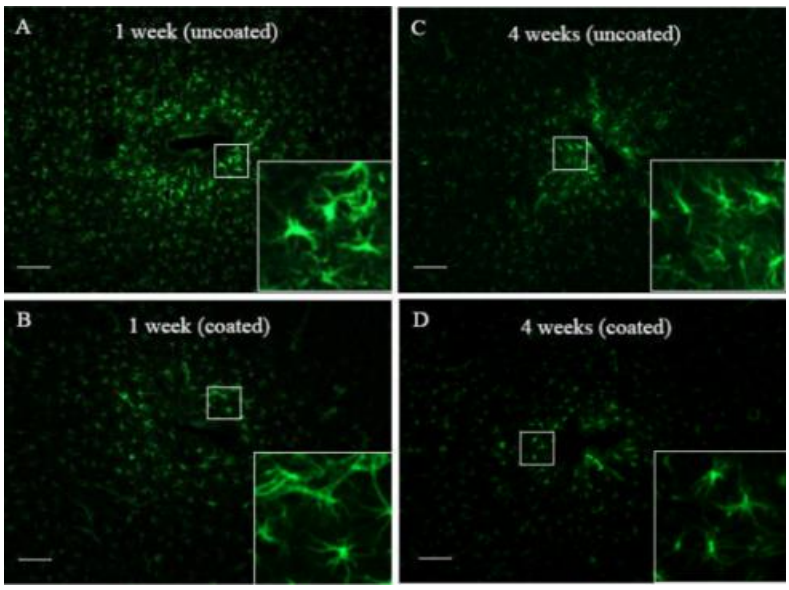

Figure 2-5: Images of GFAP staining for astrocytes 1 week and 4 week post device implantation comparing uncoated and DEX coated probes. Scale bar : 100 µm[56].

There have been other research modifying electrodes using conductive polymers[62–64]. Poly(3,4-ethylenedioxythiophene) (PEDOT) and poly(pyrrole) (PPy) are the two most commonly used materials for chronic neural probe applications. PEDOT and PPy help improve the electrode-cell interface due to their high charge injection capacity, compliant mechanical properties compared to brain tissue, thermal stability and biocompatibility[65–70]. More recently, Kolarcik et al. combined approaches using both conductive polymers and anti-inflammatory drugs by coating neural probes with a PEDOT, carbon nanotube (CNT) and DEX composite[71]. The addition of carbon nanotube increased the electrode conductivity, and improved composite attachment to the neural probe. Furthermore, the carbon nanotube provided a reservoir for DEX storage and enabled fine controlled release of the drug through electrical stimulation to prolong drug efficacy.

2.3.2 Device design parameters to improve electrode-cell interface

Another approach to improve the electrode-cell interface is to manipulate different device design parameters. Probe size and material are two parameters that have been widely studied. Larger devices (>100 μm wide long-term) are expected to cause more tissue disruption upon device implantation due to chronic shear injury and foreign body response, and ultimately induce a more severe chronic glial cell encapsulation[43,72–75]. Kozai et al has shown that ultrasmall microelectrodes (7 μm in diameter) reduced chronic tissue response compared to commercially available Michigan probes (100 x 150 μm) (Figure 2-6[8])[76]. It is therefore hypothesized that creating miniaturized probes will help reduce the extent of both acute and chronic tissue response through minimizing insertion trauma [9,77,78].

Material property is also identified as a contributor for tissue response. Mechanical mismatch between a rigid neural probe and the adjacent tissue layer can trigger cell recognition and induce a foreign body response due to the interfacial strain. Furthermore, friction between the interfaces is shown to worsen inflammatory response and disrupt the microenvironments[79–81]. Several groups have suggested the fabrication of probes from flexible materials such as polymers to minimize tissue responses by aiming to mechanically match device compliance with that of adjacent tissues[33,82–87]. More flexible materials have been used including SU-8, polyimide or poly(p-xylylene) (parylene) to improve recording ability compared to rigid silicon-based probes[34,35,88,89]. However, effectively inserting these

[8] Reprinted by permission from Macmillan Publishers Ltd: Nature Materials, Kozai, T. D. Y. *et al.* Ultrasmall implantable composite microelectrodes with bioactive surfaces for chronic neural interfaces. Copyright 2012.

flexible probes usually requires probes larger than their silicon counterparts and/or large insertion shuttles to aid in implantation, which usually causes larger mechanical trauma upon device insertion. Therefore, there have been efforts to investigate suitable insertion shuttles to aid such small and flexible devices for implantation with minimal mechanical trauma that might lead to short and long term reactive tissue response.

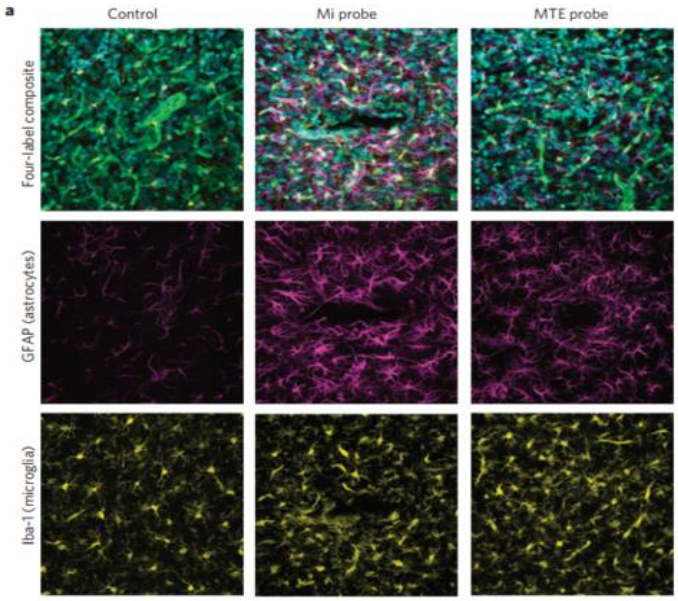

Figure 2-6: Histological analysis comparing standard Michigan probe (Mi probe) with microthread electrodes (MTE) using GFAP (astrocytes) and Iba-1(microglia) staining. The animal was sacrificed two weeks after devices implantation. Less astrocytes can be observed in the MTE than the traditional Michgan probe. More microglia can be observed near the traditional michigan probe implatation site compared to the MTE[73].

2.4 Insertion aids for miniaturized and flexible neural probes

Various insertion aids have been investigated to allow insertion of flexible probes. An ideal insertion aid will provide sufficient mechanical strength to penetrate the tissue in a narrow and sharp form to minimize the tissue response induced by insertion. Insertion aids made from stiffer materials such as needles or silicon shanks are incorporated with the flexible probes as temporary insertion shuttles and are removed after implantation [90,91]. However, these types of removable shuttles are usually stiffer and larger in size, and may therefore compromise probe performance due to mechanical trauma during insertion.

Another method to stiffen flexible microprobes is to encapsulate the device within biodegradable polymers as a temporary shuttle for insertion[92,93]. Poly(ethylene glycol) (PEG) has been investigated as an insertion aid due to its biocompatibility and solubility in the tissue solution body fluids (Figure 2-7 (A)[9])[91,94–97]. However PEG has limited rigidity and therefore requires thicker coatings to ensure successful insertion. Poly(D,L-lactide-co-glycolide) (PLGA) has also been used as an insertion aid for flexible parylene neural probes because it is both biocompatible and biodegradable and is widely used in biomedical applications (Figure 2-7 (B)[10])[98]. However, the degradation time of PLGA is around 3 to 4 weeks, which exceeds the time over which the acute and even chronic tissue responses

---

[9] © 2009 IEEE. Reprinted, with permission, from Chen, C.-H. *et al.* Three-dimensional flexible microprobe for recording the neural signal in *Nano/Molecular Med. Eng. (NANOMED), 2009 IEEE Int. Conf.* October, 2009.

[10] Reprinted with kind permission from Springer and Science and Business Media, "Springer and Biomedical Microdevices, Volume 11, 2009, Page 915-924, Flexible microfluidic devices supported by biodegradable insertion scaffolds for convection-enhanced neural drug delivery. Foley, C., Nishimura, N., Neeves, K., Schaffer, C. & Olbricht, W., Figure 2.

occur. Carboxyl-methylcellulose (CMC) has also been proposed as a shuttle which can couple with neural probes for insertion (Figure 2-7 (C)[11])[99]. It is bio-dissolvable and has also been proposed as a matrix for slow release of other molecules such as neural regenerative drugs to prevent tissue responses. However, when tested, the CMC composite was reported to become gel-like instead of completely degrading within the body, thereby potentially limiting the proximity of neural units.

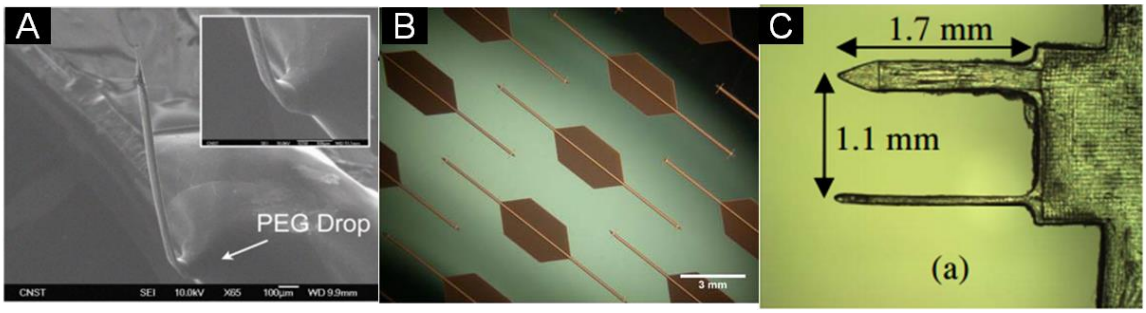

Figure 2-7: Images of various insertion shuttles for flexible probe implantation. (A) Poly(ethylene glycol)(PEG) coating[94]. (B) Poly(D,L-lactide-co-glycolide) (PLGA) insertion shuttle[98]. (C) Carboxyl-methylcellulose (CMC) insertion shuttle[99].

More recently, instead of incorporating flexible probes with degrading insertion shuttles, there are groups fabricating probes using novel materials where the stiffness is reduced following device implantation. One example is the fabrication of devices out of shape memory polymers that are stiff during implantation and soften *in vivo* to approach the brain tissue modulus[100–102]. However, the device stiffness (shear modulus ~700 MPa)

[11] 2012 IEEE. Reprinted, with permission, from Gilgunn, P. J. *et al.* An ultra-compliant, scalable neural probe with molded biodissolvable delivery vehicle in *Micro Electro Mech. Syst. (MEMS), 2012 IEEE 25th Int. Conf.* Februrary, 2012.

prior to insertion is still less than silicon (~200 GPa) and therefore a larger device is required to ensure successful implantation.

A mechanically adaptive polymer nanocomposite probe has been fabricated via film casting[103–105]. The material is capable of decreasing its tensile modulus from 5 GPa pre-insertion to 12 MPa post-insertion within 15 minutes under physiological conditions. However, since the study examined the implants without electrode traces, future investigation may be needed to ensure that the nanocomposite casting procedure can accommodate the patterning of recording elements.

2.5 Tyrosine-derived polycarbonates as an insertion shuttle for neural probe implantation

Previously, our group identified novel tyrosine-derived polycarbonates as a promising insertion shuttle. The polymer is biocompatible, mechanically stiff enough to sustain mechanical strength for probe insertion while rapidly degrading within couple hours following device implantation. Preliminary studies were performed by coating either flexible thin polyimide films or microwires (70 μm in diameter) with the polymer. Figure 2-8[12] displays the time lapse fluorescent images of the thin polyimide films coated with slow (E1001(1K)) and fast degrading (E5005(2K)) polymers. The fast degrading polymer degraded 270 minutes after device implantation whereas the slow degrading polymer was

[12] Reprinted from Acta Biomaterials Vol 7, Lewitus, D., Smith, K. L., Shain, W. & Kohn, J. Ultrafast resorbing polymers for use as carriers for cortical neural probes. Page 2483-2491,.Copyright (2011), with permission from Elsevier.

still intact at this time point. An in vivo animal study was also performed inserting uncoated microwires and fast degrading polymer coated microwires into rat brains (Figure 2-9[13]). Results showed there was no difference in the tissue response between the coated and uncoated microwires suggesting there are no adverse effects of the polymer on the acute or chronic tissue responses.

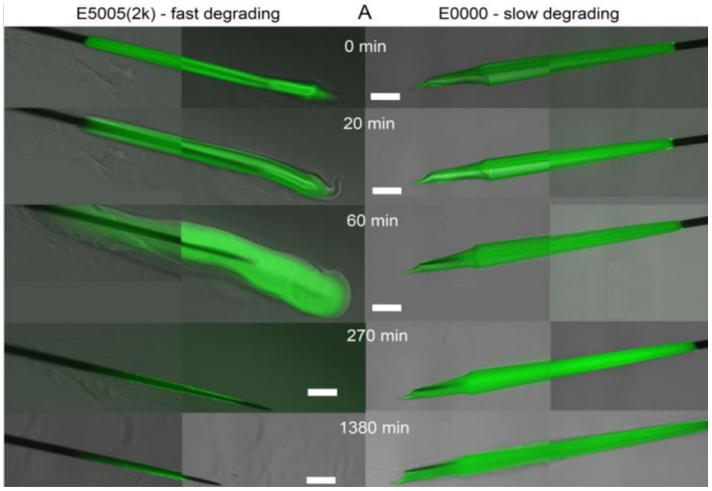

Figure 2-8: Time lapse fluorescent images of thin polyimide films coated with (a) fast-degrading polymer (E5005(2K)) and (b) slow-degrading polymer (E1001(1K))[126]. The probes were inserted into agarose gel.

The work demonstrated promising results for using tyrosine derived polycarbonates as an insertion shuttle. However, the devices were coated with the polymer through a dip-coating method. The coating dimensions were less defined and usually thicker than what

[13] Reprinted from Acta Biomaterials Vol 7, Lewitus, D., Smith, K. L., Shain, W. & Kohn, J. Ultrafast resorbing polymers for use as carriers for cortical neural probes. Page 2483-2491,.Copyright (2011), with permission from Elsevier.

is required for insertion (~200-500 μm). The dip-coating method introduces large variability for coating dimensions as well as higher risks of severe tissue response due to mechanical trauma induced by an unnecessarily thick polymer coating. It therefore motivated this thesis to develop a more confined and smaller polymer coating that is sufficient for device insertion. Furthermore, the microwires can penetrate brain tissue on their own with proper and careful handling. Therefore, it is desirable to develop a much smaller and flexible probe that would require the polymer coating as an insertion aid to further minimize tissue response.

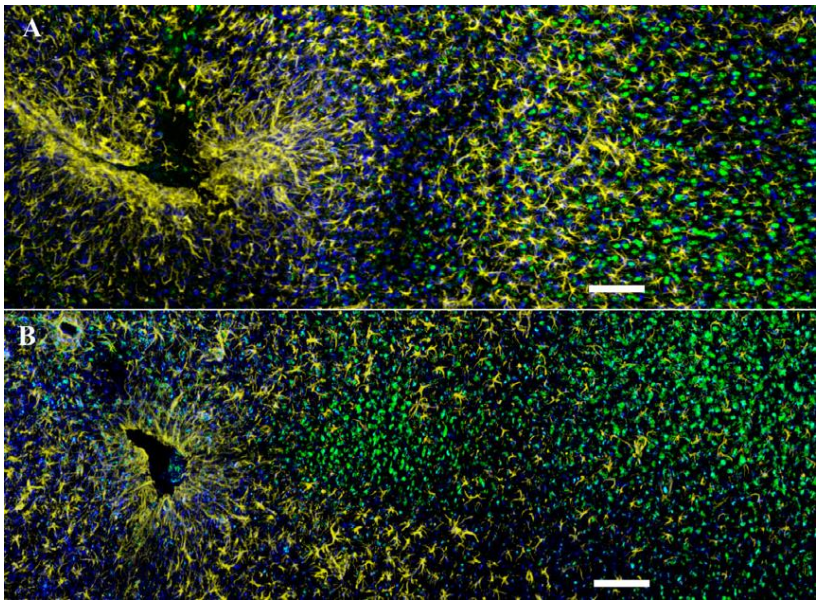

Figure 2-9: Histological analysis comparing uncoated the microriwes with polymer coated microwires using GFAP (astrocytes (yellow)) , Iba-1(microglia(blue)) and Nissl (neurons (green)) staining[126]. The animal was sacrificed 1 week after device implanation. Scale bar : 100 μm.

CHAPTER 3 DEVICE FABRICATION AND CHARACTERIZAION

Note: Part of this chapter is reproduced from the following publication:
Lo, M. *et al.* Coating flexible probes with an ultra fast degrading polymer to aid in tissue insertion. *Biomed. Microdevices* **17,** 9927 (2015).[106]

3.1 Overview

In this chapter, the development of the miniaturized neural probe coated with an ultrafast degrading polymer is described. A fabrication process that incorporates probe fabrication and polymer coating process was developed and a series of non-functional (lacking electrodes) coated probes were fabricated and physically examined to ensure coating reproducibility and a high yield process. SU-8 was chose as an early test material on which to develop the coating protocol due to easier fabrication of SU-8 probes, although the final probes for in-vivo work were manufactured using parylene due to the better mechanical properties of parylene compared to SU-8.

The coated probes were mechanically characterized measuring buckling and insertion forces, chemically characterized by monitoring the degradation profiles of the polymer coating in order to identify the ideal probe and coated polymer dimensions that can overcome the force barrier required for successful insertion while degrading fast enough to minimize tissue response. Finally, the fabrication and polymer coating process was adapted to fabricate polymer coated probes made from parylene, as a better probe

material candidate in terms of better mechanical match with neural tissue, inert property and biocompatibility.

3.2 Device design and fabrication

3.2.1 Tyrosine-derived polycarbonate

The tyrosine-derived polycarbonate based co-polymer used for coating was developed and synthesized at the New Jersey Center for Biomaterials according to previously published procedures[107,108] from 3 monomers: desaminotyrosyl-tyrosine alkyl ethyl ester (DTE), desaminotyrosyl-tyrosine (DT), and low-molecular-weight poly(ethylene glycol) (PEG).

The naming convention for this type of polymer is EXXYY(MW), meaning poly(DTE-co-XX%DT-co-YY%-PEGMW carbonate) where XX is the mole percent of DT, YY is the mole percent of the PEG and the MW is the average molecular weight of the PEG (Figure 3-1). The mechanical and chemical properties of these polymers depend on the polymer composition and relative molar percentages of the three monomers. The DTE component provides strength and stability, the DT component determines resorbtion rate and has a carboxyl group that allows functionality, and the PEG component determines resorbtion rate. The polymer degrades via hydrolysis of the carbonate linkages. The incorporation of DT and PEG in the polymer backbone makes the polymer more hydrophilic, enhancing the degradation rate by allowing faster water absorption. The specific type of polymer that was primarily used in this work is E5005(2K) (E=1.6 GPa,

T_g = 57°C, M_n=100K) which is 50% DT, 5% PEG. The E5005(2K) composition was found to have the proper mechanical and chemical qualities desired for an insertion aid, in that it has a fairly high Young's modulus (E=1.6 GPa), while being able to chemically degrade fully within a few hours .

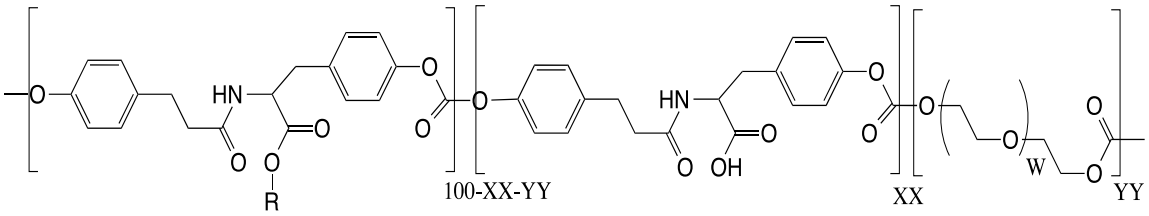

Desaminotyrosyl-tyrosineester (DTE) | Desaminotyrosyl-tyrosine (DT) | Poly(ethylene glycol) (PEG)

Figure 3-1: Chemical structure of the tyrosine-derived polycarbonate (Poly (DTE-co XX%DT-co-YY%PEG (MW))

3.2.2 Design criteria of the polymer coated probe

In order to determine appropriate probe dimensions required for tissue insertion, the buckling forces supported by probes of various dimensions were calculated to understand how changing length, width and height of the coated probes affect the mechanical failure limits. The polymer powder was dissolved at 10% w/v in dimethylformamide (DMF), cast into polytetrafluoroethylene (Teflon) dishes and cured at 70°C under vacuum for 3 days. The Young's modulus of the polymer was then measured using a MTS Sintech Universal Testing Machine (MTS System Corp. Eden Praire, MN, USA) with a 100 N load cell. The cast polymer films were 75 μm thick, with different widths (0.79, 1, 1.58, 2, 3 and 4 mm) and a length of 40 mm. The polymer films were

inserted in a 1% agarose gel phantom which has similar properties to brain tissue and the insertion force was measured using the normal force sensor on a Kinexus rheometer (Malvern Instruments, Westborough, MA, USA) by compressing the probe at a rate of 0.5 mm/min. An insertion force of approximately 7 mN was found for probes with widths varying from 0.79 to 4 mm using this set up. Therefore, a 7 mN threshold was used as the minimal force barrier which any designed probe must be overcome to allow for probe insertion. Once this threshold was established, suitable coated probe dimension ranges for investigation could be determined. For simplicity of calculations, the coated probe was assumed to be a solid tyrosine-derived polycarbonate polymer matrix. This is because most of mechanical rigidity is expected to be the result of the polymer coating.

When a probe is inserted into tissue, the insertion occurs axially and therefore probe failure is expected to occur via buckling. The buckling force a probe can support can be calculated and estimated by Euler's buckling equation (Equation 1) where E is the Young's modulus of the material specific to probe coating material. I is the area moment of inertia which is defined by the cross-sectional area (width and thickness) of the probe. L is the unsupported length of the column and K is the column effective length factor which is determined based upon the boundary conditions at each end of the probe. When coated probes are inserted into an agarose gel, one end is fixed by the machine and the other end is pinned once it makes contact to the gel meaning it is not allowed to move laterally but free to rotate. For this condition K has a value of 0.6999[109]. The moment of inertia is determined by the geometry of the probe. In these scenarios, the probe is assumed to be a

rectangular beam where h is the thickness of the probe and b is the width of the probe (Equation 2). By substituting (2) into (1), a buckling force equation related to the probe geometry can be obtained (3). 1.64 GPa, which is the Young's modulus of the polymer (E5005(2K)) was used for calculations assuming the coated probe was solidly filled without the actual probe encapsulation.

Equation 1 $$F = \frac{\pi^2 EI}{(KL)^2}$$

Equation 2 $$I = \frac{bh^3}{12}$$

Equation 3 $$F = \frac{\pi^2 Ebh^3}{5.88L^2}$$

Typical neural probes are usually 1 to 5 mm in length. Research has found that insertion depths of ~2 mm yield the highest number of spike waveforms in the motor cortex so the probes' length were chosen to be slightly longer than 2 mm in length to accommodate handling and insertion variability between subjects[110]. Figure 3-2 displays the buckling force calculations for various probe dimensions for a 3.5 mm long probe with varying shank width and thickness. The red line is the force barrier of 7 mN. For a 100 µm thick probe, the buckling forces are over 7 mN when the probe is above 80 µm wide. For a 65 µm thick probe, the probe must be at least 150 µm wide to overcome the force barrier. Figure 3-3 displays the buckling force calculation with a 100 µm thick probe as a function

of varying lengths and widths. The buckling forces overcome the 7mN force barrier at widths of 75, 80, and 90 µm for 3.5, 4, and 4.5 mm long shanks respectively.

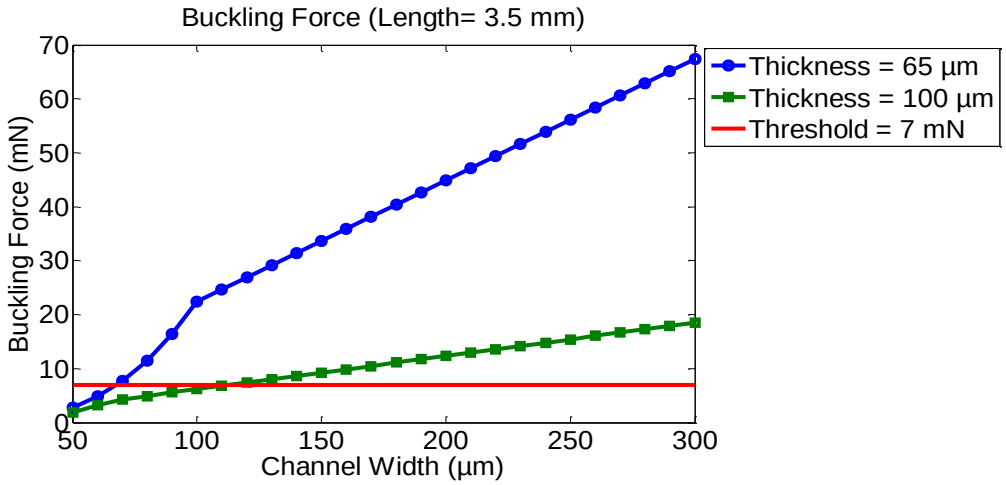

Figure 3-2: Probe buckling force vs. shank widths and thickness. (Length: 3.5 mm; Thickness: 100 µm and 65 µm)

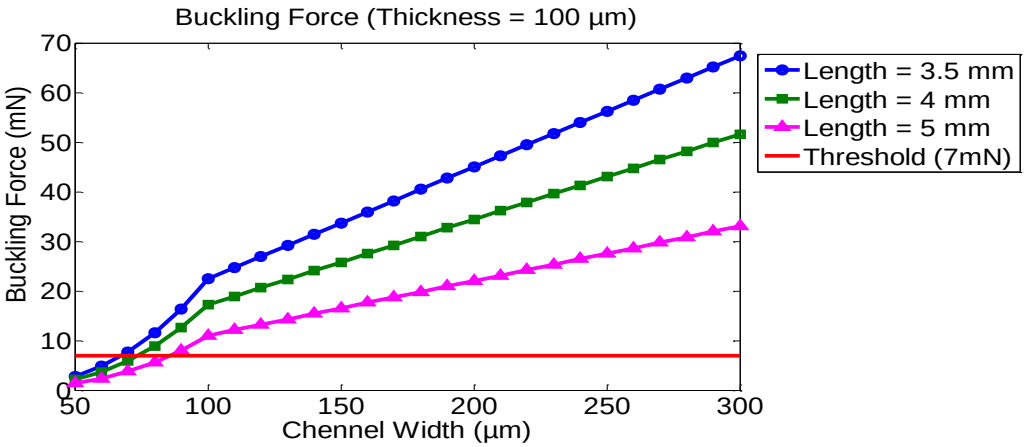

Figure 3-3: Probe buckling force vs. shank width and length. (Thickness: 100 µm; Length: 3.5 mm, 4 mm and 5 mm)

Since the actual probes are encapsulated within the polymer shanks, the actual buckling force is expected to be smaller compared to these calculations. Therefore, a safety factor of five to ten times larger than the 7 mN force barrier (35 to 70 mN buckling force) provides a much more conservative estimate for the desired coated probe dimensions. Therefore, the final coated probe length was chosen at least to be 3.5 mm long, with a 100 µm thickness. These dimensions can also be easily modified during the fabrication process if the need arises. Finally, various shank widths ranging from 90 µm to 400 µm were chosen to test multiple coated probe designs in providing strength for insertion.

Moreover, various probe dimensions ranging from 5-50 µm wide and 5-10 µm thick were chosen to identify the appropriate final probe dimensions that can record electrical signals while reducing the acute and chronic tissue response through miniaturized features.

In ideal situations, probes are inserted into tissues completely axially so all forces are transmitted axially along the probe. However, in real applications, any misalignment of the probe with the tissue could produce a force component perpendicular to the probe tip which can produce a bending moment. Therefore, it is also essential to calculate the transverse bending force that the device can withstand. The maximum bending stress in the shank can be calculated by equation 4. In this case, the maximum stress, σ, supported by the probe is defined by the yield strength (σ_y) of the material. For the E5005(2K) polymer the yield stress value was previously determined to be 28.4 MPa. c represents to maximum

distance from the neutral axis to the device edge and is set at h/2 and I represents the area moment of inertia (previously described in Equation 2) and both of these variables depend on the device geometry.

Equation 4 $$\sigma = \frac{Mc}{I}$$

M represents the bending moment which is maximum at the fixed end of the device. Thus the maximum moment is the transverse tip force (F) multiplied by the length of the device (L).By replacing M with F and L, the maximum transverse tip force which can be supported without shank yielding is calculated in Equation 5 as follows:

Equation 5 $$F = \frac{\sigma_y I}{cL}$$

By combining Equation 2 and Equation 5, the bending force can be calculated as Equation 6 where b is the width of the device and h is the height of the device.

Equation 6 $$F = \frac{\sigma b h^2}{6hL}$$

When calculating buckling forces, the bending forces the device could support were calculated based on various shank dimensions (Figure 3-4 and 3-5). There is linear relationship between the channel width and the maximum transverse tip forces as wider shanks can withstand more force before yielding. As the length of the device increases, the

bending moment for a given tip force increases. Different shank thicknesses were also compared. The supportable bending force for a 100 µm thick device is about twice as large as the 65 µm thick devices as expected from the change in area moment of inertia and distance from the neutral axis. This suggests that thicker devices would be more mechanically able to withstand bending moments acting on the shanks. The bending forces are also all in the range 0.5 mN or less which is significantly smaller than the buckling forces calculated previously (mostly ranging from 10 to 100 mN). This result suggests that any bending due to a transverse force could be the critical mode of mechanical failure compared to buckling due to the axial force. Therefore, it is essential to ensure the devices are inserted as axially as possible to avoid the generation of bending moments.

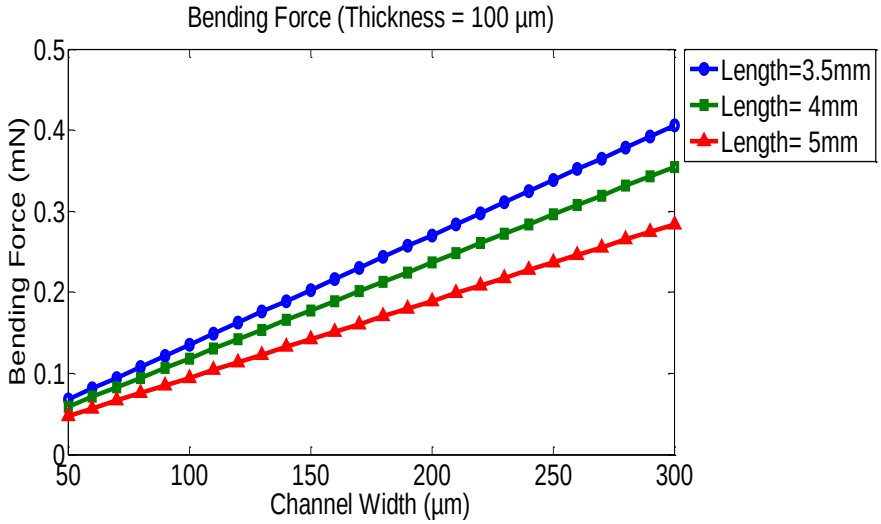

Figure 3-4: Probe bending force vs. shank width and length**.** (Thickness: 100 µm; Length: 3.5 mm, 4 mm and 5 mm)

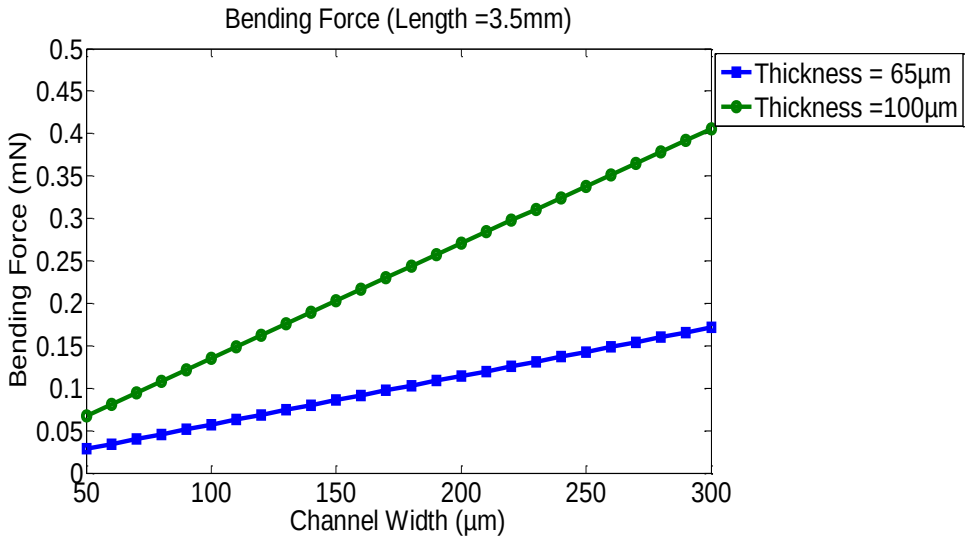

Figure 3-5: Probe bending force vs. shank width and thickness. (Thickness: 65 µm, 100 µm; Length: 3.5 mm

The scope of the polymer coated probe dimensions was identified through analytical estimations to accommodate possible mechanical failure modes such as buckling and bending. These initial calculations were further validated experimentally downstream in order to refine different design parameters of the polymer coated probe by confirming the polymer material constants, choosing the most appropriate safety factors for the buckling force estimations in order not to over accommodate the effect of actual probe encapsulation and better estimations of bending forces to improve device insertion protocols.

3.2.3 Polymer coated SU-8 probe fabrication procedure

Material and methods

The microprobe fabrication can be split into two parts: 1) Polymer coating mold fabrication; 2) Probe fabrication and polymer coating. The polymer coating mold was fabricated via a standard photolithography process. A thick negative photoresist (SU-8 2075) was spin-coated (2000 rpm) on a silicon substrate to the desired thickness (110 µm). The molding structure was defined and patterned by photolithography. Polydimethylsiloxane (PDMS) was poured over the master to create the molding cavity through soft lithography. After curing, the PDMS molding structure was removed from the wafer and a hole was drilled through the anchoring area as a solution inlet in the downstream polymer coating process.

PDMS was chosen as a substrate layer for fabrication to take advantage of the weak adhesion between PDMS and SU-8. This allowed for the device to be lifted from the substrate while still providing support to carry out photolithography to define the probe structure. To prevent significant contraction of SU-8 layer during baking because of rapid solvent evaporation, a special soft baking recipe at a lower temperature for a longer baking time was conducted. This ensured the desired uniform coating of SU-8 on top of the PDMS substrate. First, PDMS was mixed with the curing agent at 10:1 weight ratio for substrate coating. A thin layer of PDMS (65 µm) was spin-coated (2000 rpm) on top of the glass substrate, and baked for 5 minutes to cure the PDMS. Second, a thin layer of SU-8 (SU-8 2010; 10-20 µm) was spin-coated on top of the cured PDMS substrate layer. The whole

device was then baked at 30°C, 35°C, 40°C, 45°C, 50°C, 55°C, 60°C and 65°C for 5 minutes at each temperature, and then cooled to room temperature for at least 1 hour before downstream exposure. The SU-8 was then patterned to the probe geometries with standard photolithography. The probe was imaged using scanning electron microscope (SEM) (AMRAY-1830I, AMRAY, Bedford, MA, USA) to ensure probe integrity prior to polymer coating. Following probe definition, the PDMS molding piece, previously fabricated, was aligned with the SU-8 probe under a light microscope, and pressed onto the substrate to form a conformal contact and a molding capillary.

The E5005(2K) polymer solution was infused from the molding inlet to coat the probe using the micromolding in capillaries (MIMIC)[111] process, where polymer solution is introduced into a microchannel reservoir and fills the cavities through capillary action. The E5005(2K) polymer solution was prepared as 9% w/w in anhydrous 1, 4-dioxane (Sigma-Aldrich, St. Louis, MO, USA). To begin the coating process, 5 µL of polymer solution was introduced through the reservoir inlet twice at room temperature. The whole device was then placed on a 75°C hotplate, and 5 µL of the polymer solution was introduced 3 times at 5 minute intervals. The device remained on the hotplate for another 2 hours to drive off the solvent. To slowly and completely evaporate the solvent within the polymer, the whole device was placed under -15 inHg vacuum at 50°C for an hour, and finally in full vacuum (-29.92 inHg) for at least one day. The vacuum was increased slowly to remove any air bubbles to prevent cavitations of the solvent and improve the coating quality. Finally, the PDMS molding structure was peeled off from the PDMS substrate and

physically lifted away using tweezers. The polymer coated probes were then stored in 24-well cell plates that were vacuum sealed and stored in a -20°C freezer until downstream characterization to prevent polymer degradation from ambient humidity. For testing, the probes were returned to room temperature under vacuum for 15 minutes and fixed on a glass slide (Figure 3-6).

Figure 3-6: (Left) Polymer coating process. The polymer solution was introduced at the reservoir. Solvent evaporated and polymer solidified from the edge of the mold , eventually filling the whole cavity. (Right) Packaging method for the polymer coated probes.

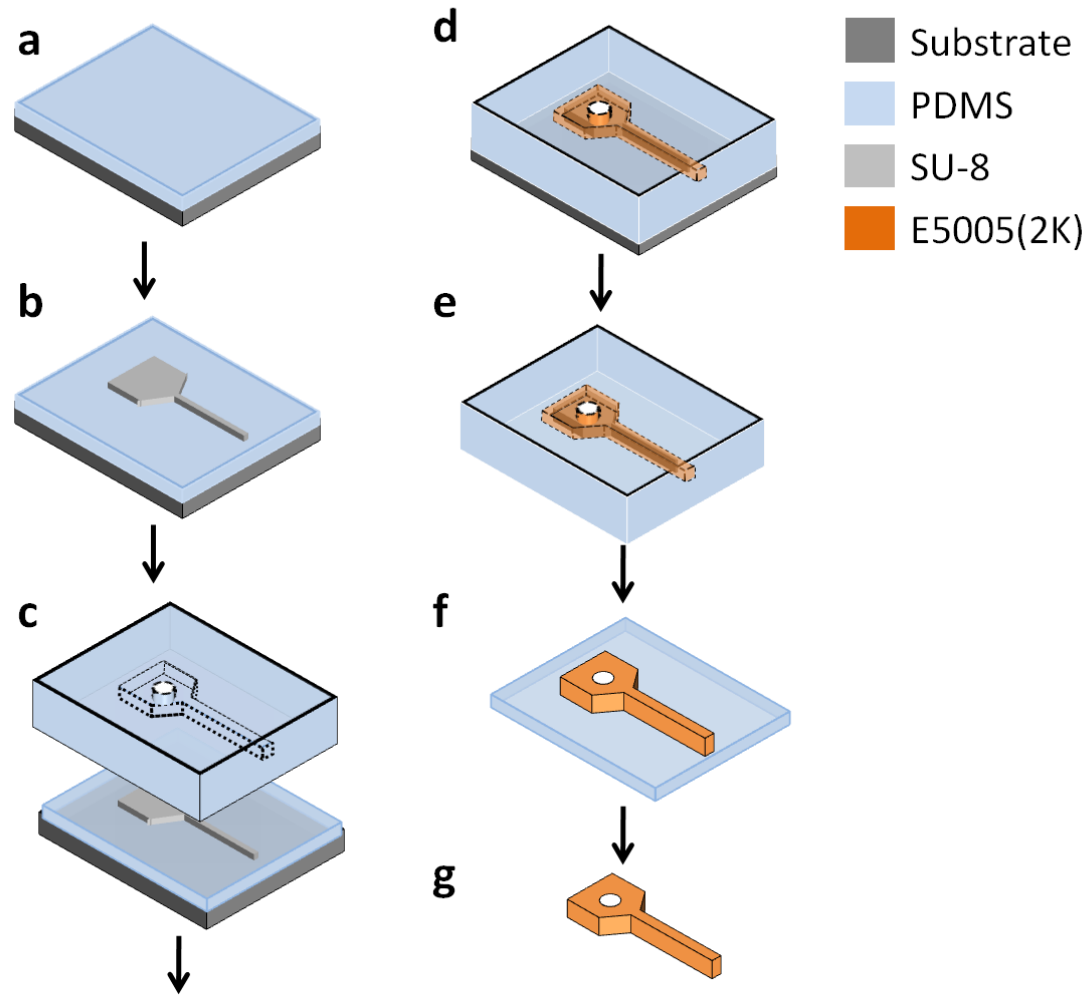

Figure 3-7: Schematic of the polymer coated probe fabrication process. a) A thin layer of PDMS (~65 µm) is spin coated on to a substrate. b) The probe geometry is patterned on top of the PDMS layer. c) The SU-8 probe is aligned with the molding structure. d) Polymer solution is infused through the inlet of the mold using MIMIC technique and the polymer solvent is allowed to evaporate. e) The device is released from the substrate. f) The device is released from the molding structure. g) The device is lifted mechanically off from the PDMS substrate.

Results and discussion

Different non-functional SU-8 probes with widths varying from 20 to 40 μm and thickness of 10 μm or 20 μm were fabricated. Figure 3-8(a) displays a SEM image of the non-functional SU-8 probe on a PDMS substrate. The prolonged, gradient, and low temperature soft baking recipe, which prevents SU-8 shrinkage on the PDMS substrate, did not affect the final probe integrity. The large pentagon shaped area defined the handling area for integration with other instrumentation, such as a mechanical support for handling or electrical integration for signal recording. The cross marks aided in aligning the molding structure for polymer coating. A weak point that caused fabrication failure was noted at the transition between the anchoring area and the probe shank, where most of the mechanical disruption occurred as the structure was peeled from the substrate. SU-8 probe integrity was therefore maintained by a smooth transition between the anchoring area and the probe shank. SU-8 exhibits a high residual stress following exposure that may result in a rough surface on the probe itself or distortion of the probe shaft once released from the substrate. Therefore, alternative and more biocompatible materials, such as parylene, were used in the future to fabricate functional probes.

The ideal polymer coating should yield a uniform coating and smooth surface to minimize the amount of tissue disruption upon insertion that can lead to both acute and chronic tissues responses. Figure 3-8(b) shows a light microscopy image of a polymer coated probe that has been lifted from the PDMS substrate and fixed on a glass slide. The SU-8 probe can be clearly identified in the middle of the polymer shank, without material

disruption or damage during fabrication and device lift-off. Figure 3-8(c) displays a SEM micrograph of the coated probe from the back. The bottom side of the SU-8 probe was not coated with polymer due to attachment between the probe and the substrate. The SU-8 probe shape can be identified within the polymer shank, and the polymer coating was smooth and rigid, indicating that there was no material disruption between the polymer coating and probe during encapsulation.

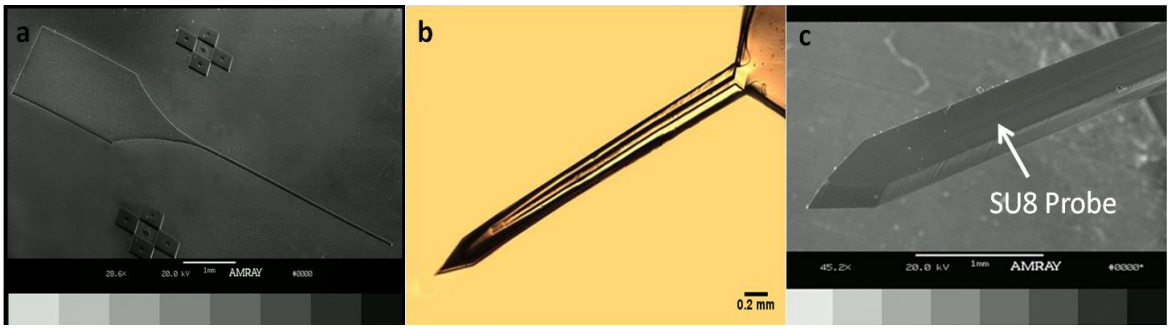

Figure 3-8: (a) SEM micrograph of a non-functional SU-8 probe. Probe dimension: 30 µm wide, 10 µm thick and 3 mm long. (b) Light microscope image of the coated probe. (c) SEM micrograph of the coated probe. Device dimension: polymer shank: 200 µm wide, 100 µm thick and 3.5 mm long. SU-8 probe: 30 µm wide, 20 µm thick and 3 mm long

One design consideration for this work is the need to ultimately remove the coated probe from the supporting substrate following fabrication. Most polymer neural probes are usually removed from their substrate through dissolution of a sacrificial layer patterned under the device. However, due to the chemical characteristics of the tyrosine-derived polycarbonate, most organic and aqueous solutions will cause the E5005(2K) polymer to degrade/erode. Therefore, releasing the final device through wet chemical etching of a

sacrificial layer has proved impractical, compared to mechanical lift-off methods. PDMS was used as the supporting layer, allowing the whole device to be mechanically peeled from the substrate[112]. However, mechanical peeling methods are not optimal as they could physically damage the coated probe. As an alternative, xenon difluoride etching of the substrate was also identified as a dry etchant to release the probe[113–115]. XeF_2 is a dry, isotropic, vapor-phase etch that is highly selective to silicon with respect to aluminum, photoresist and silicon dioxide. The etch rate is about 2 μm/minute. It is a white crystalline solid at room temperature and atmospheric pressure, but sublimates at its vapor pressure of 3.8 mmHg at 25°C. It will be investigated as a future release candidate due to its high selectivity and vapor-phase isotropic etching characteristics which allows undercutting of large structures.

3.3 Device characterization

3.3.1 Mechanical testing of the coated probes

Materials and methods

The coated probes were characterized ex-vivo by inserting the probe into chicken embryo brain to measure force and displacement over time. Fresh fertilized eggs (Charles River Labs, Wilmington, MA, USA) were incubated until embryonic day 18 and the brain was extracted. The excised brain was place in a petri dish containing 37°C PBS on a hot plate before measurement. The force measurements were performed with a uniaxial load-displacement apparatus (ELF 3200, Bose Corp., Eden Prairie, MN, USA) (Figure 3-9). The measuring platform was fixed to a 0.5 N cantilever-typed load cell (Entran Sensors and

Electronics, Hampton, VA, USA) that was held in position using a clamp to the bottom actuator of the Instron. The load cell was calibrated by a sequential set of known weights prior to testing. The probe was clamped on the top of the actuator with a height of 3 mm from the tip of the probe to the brain tissue. The top actuator mounted with the probe was displaced at a rate of 0.01 mm/s to a maximum of 6 mm. The buckling forces were obtained when the probes made contact to the bottom of the sample holder which was a rigid surface. Theoretical buckling force estimation assumed a solidly filled polymer shank without any probe encapsulation. Data acquisition was performed by WinTest software (Bose Corp., Eden Prairie, MN, USA) and forces, displacements with respect to time measurements were obtained. The buckling force was measured and defined as the force generated when the probe penetrated through the brain tissue and made contact with the rigid surface of the platform. A level was used to confirm the probe was perpendicular to the testing platform and positioned so that insertion occurred around the motor cortex region of the brain. When the testing began, different polymer coated probes were inserted into the same brain at different locations. After 15 minutes, the brain was discarded and a fresh brain was used to prevent possible dehydration of the sample that might change the material and mechanical properties. Twenty-two coated probes with different dimensions were tested for buckling force measurements. Four insertions were done per brain before the brain was discarded. Data were processed using MATLAB (Mathworks Inc, Natick, MA, USA) software to filter noise, and identify the buckling force point. The experimental measurements were compared with theoretical estimations (section 3.2.2) to verify the probe quality.

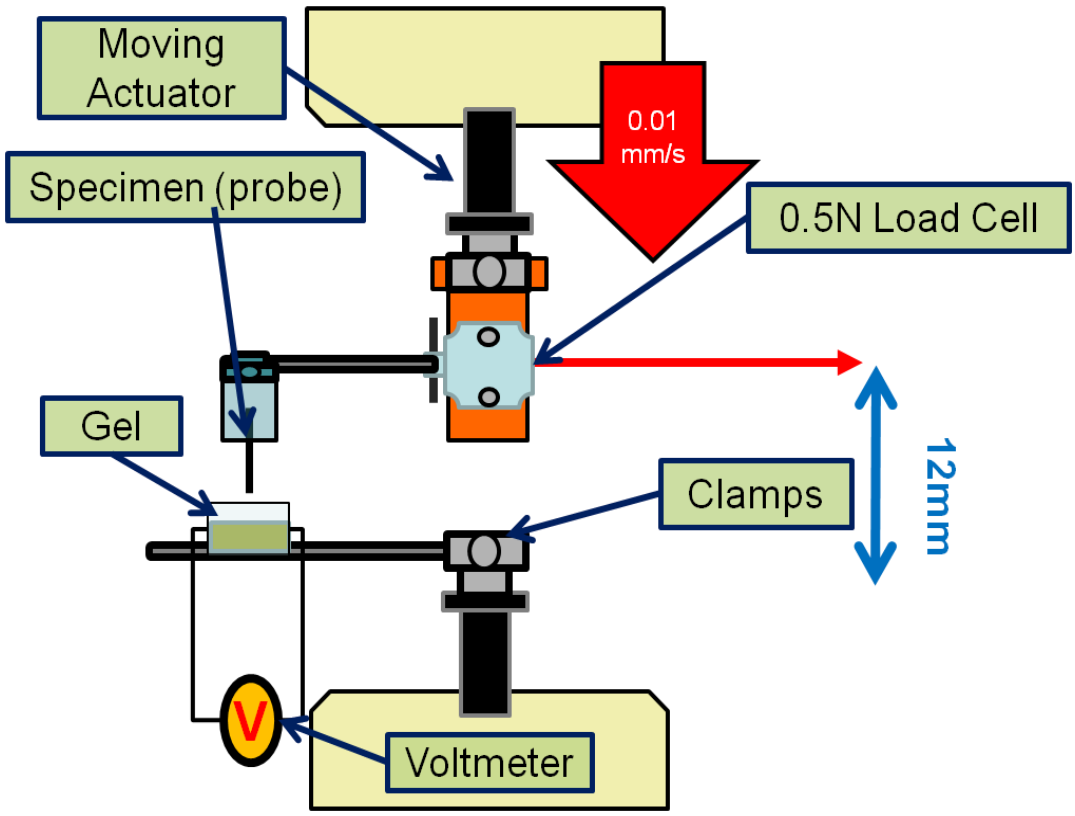

Figure 3-9: Schematic of the mechanical testing apparatus

Following the mechanical testing using chick embryo brain, the coated probes were also characterized ex-vivo by inserting them into a fresh rat brain to validate insertion capabilities (298 g female Sprague-Dawley rat; Charles River Labs, Wilmington, MA, USA). The animal was euthanized by asphyxiation in 100% CO_2 environment for at least 20 minutes under the IACUC protocol. The rat brain was then extracted and decapitated. The fresh rat brain was put on the Instron and different probes were tested with the same procedure described above to evaluate if the device succeeded in inserting into the tissue. Eleven uncoated SU-8 probes (30 µm wide × 10 µm thick × 3.0 mm long) and 12 coated probes (100 µm wide × 100 µm thick × 3.5 mm long coating) were tested. An air humidifier

was used to maintain the brain's hydration and prevent material property changes during testing.

Results and discussion

Figure 3-10 displays the experimental and theoretical buckling force measurements for varying polymer coating widths. The error bar corresponds to the standard error (n=22).The experimental buckling forces for 100 µm, 150 µm, and 200 µm coating widths were slightly larger than the theoretical values, while the experimental buckling forces for 250 µm coating width was less than the theoretical values. The differences between the theoretical and calculated buckling forces are more likely attributed to slight processing variations in coating dimensions. Since the E5005(2K) polymer is very sensitive to humidity, the polymer could also swell slightly. All of the coated probes were exposed to the ambient environment shortly before mechanical testing, therefore the coated probes might swell or alter the material and mechanical properties to result in larger buckling force measurements than theoretical estimations.

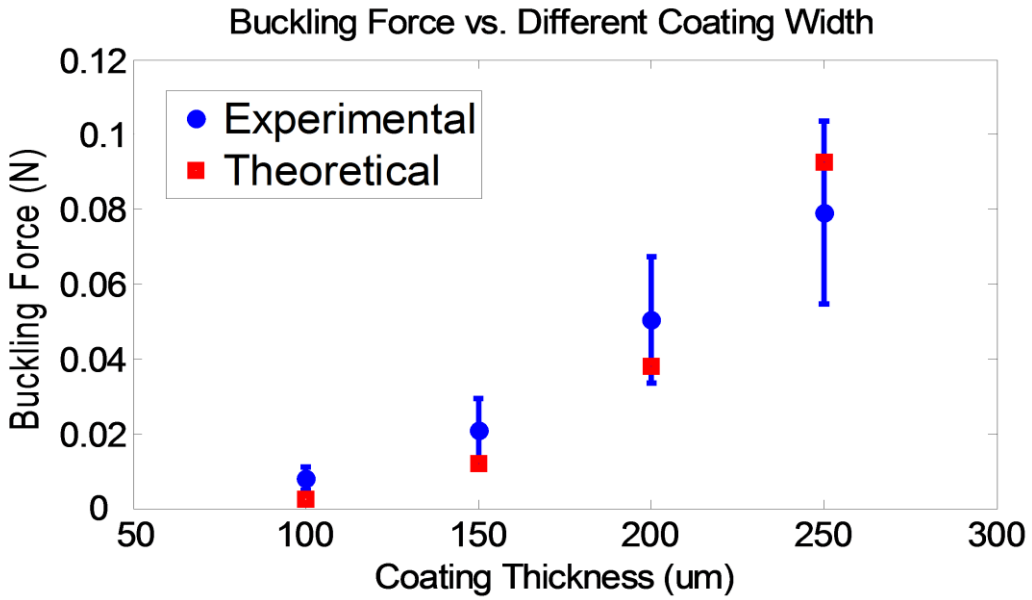

Figure 3-10: Experimental and theoretical buckling force measurements vs. different coating width. Device dimension: polymer shank: 100 µm thick and 3.5 mm long. SU8-probe: 30 µm wide, 20 µm thick and 3 mm long.

Buckling forces measured for the smaller polymer coatings (100 µm, 150 µm widths) were more accurate compared to the larger polymer coatings (200 µm, 250 µm widths). The coating quality of the smaller dimension devices was relatively smoother and exhibited fewer defects due to a more constrained cavity during the coating procedure, which made the polymer solution dry and solidify into a more uniform structure. However, despite the variances of coating qualities, the buckling force measurements fell within the standard deviation of the theoretical estimations with reasonable accuracy (<10%).

All of the polymer coated probes were able to penetrate the chicken embryonic brain tissue without buckling, indicating that at all coating dimensions, sufficient mechanical support was provided. Therefore, polymer coating dimensions can be further miniaturized and narrowed for SU-8 probes (e.g. down to 100 µm wide, 100 µm thick and 3.5 mm long or smaller).

To further validate the probe integrity, the probes were also characterized by inserting them into the rat brain. Table 3-1 displays the successful insertion rate for uncoated SU-8 probes and E5005 (2K) coated SU-8 probes. Approximately 55% of the uncoated SU-8 probes were able to penetrate brain without failing; similar to the chick brain, all of the E5005(2K) coated probe were able to do so. Even though some of the uncoated SU-8 probes were able to penetrate the tissue without buckling, the successful rate for insertion increased to 100% when the probes were coated with the polymer. Furthermore, the fact that some of the SU-8 uncoated probes were able to penetrate the tissue without buckling implies that even a more miniaturized device could be fabricated that would required the aid of polymer coating for insertion.

Table 3-1: Insertion success rate for uncoated SU-8 probe (40 µm wide, 10 µm thick and 3 mm long) and E5005(2K) coated SU-8 probe (100 µm wide, 100 µm thick and 3.5 mm long)

	Pass	**Fail**
SU-8 uncoated probe	**6**	**5**
E5005(2K) coated probe	**12**	**0**

The polymer coating dimensions were chosen according to our ex-vivo chicken embryo mechanical testing, which suggested 100 µm wide × 100 µm thick × 3.5 mm long devices would provide sufficient mechanical strength for insertion. The mechanical testing in fresh rat brains confirmed that such probes were successful, and that polymer coatings of smaller dimensions (< 100 µm wide × 100 µm thick) may be adequate.

3.3.2 Chemical characterization of the coated probes

3.3.2.1 Polymer erosion profile in PBS

Materials and methods

Two coated probe candidates (coating dimensions: 100 µm or 150 µm wide, 3.5 mm long, 110 µm thick; probe dimensions: 30 µm wide, 3 mm long, 10 µm thick) were evaluated to assess how quickly the polymer (E5005(2K)) erodes over time using a spectrophotometer (Varian Cary 50 Bio UV/Visible Spectrophotometer, Varian Inc, Palo Alto, CA, USA) to measure UV absorbance of the samples. A 3.5mL cuvette was filled with 3 mL of 10 mM Phosphate Buffered Saline (PBS; pH 7.4, Life Technologies, Grand Island, NY, USA),which was analyzed as a control before adding the probe to the cuvette. The sample was kept at 37°C in a water bath during the study except during data acquisition. Samples were retrieved from the bath and analyzed every 10 minutes until the UV absorbance reached a steady state absorbance. E5005(2K) is a tyrosine derived polycarbonate and therefore UV absorbance of the polymer is comparable to tyrosine, which is around 260 nm[116]. UV absorbance in the 240 nm to 300 nm wavelength range was

measured and monitored at each time point. The absorbance data was then processed and normalized against the maximum absorbance during the whole recording session.

Results and discussion

Figure 3-11 displays relative mass retention in percentage over time with the two different coated probe candidates (with 100 µm or 150 µm wide coatings). The relative mass retention percentage was calculated according to the UV absorbance that increases as the polymer dissolves within the PBS. Approximately 50% polymer dissolution occurred in PBS within 20 minutes. Steady state absorbance, indicating complete erosion/degradation of the polymer, was reached at nearly 60 minutes for both of the coated probes. There was no significant difference between the two samples on the rate of polymer degradation/erosion with coating size, at such a small scale. Moreover, the rate of degradation/erosion is proportional to the contact area between the probe and aqueous solution, which means the larger the polymer coating, the faster the degradation/erosion rate. This effect may offset the larger mass that would otherwise take more time to degrade.

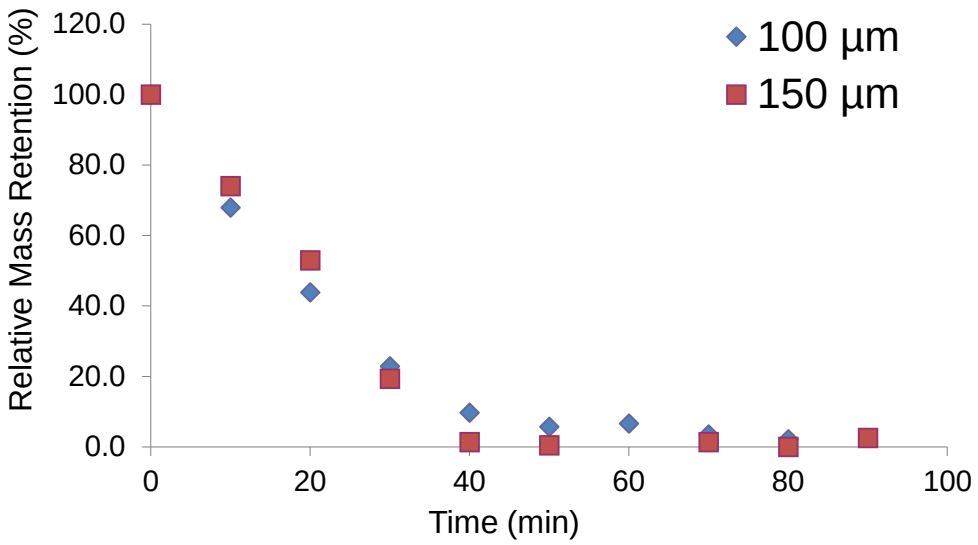

Figure 3-11: Relative mass retention of the E5005(2K) coated probe with different probe candidates. Device dimension: polymer shank: 100 or 150 µm wide, 100 µm thick and 3.5 mm long. SU8-probe: 30 µm wide, 20 µm thick and 3 mm long.

3.3.2.2 Polymer erosion profile in a brain tissue phantom

Materials and methods

The polymer erosion/degradation profile was further examined using an in vitro brain tissue phantom to simulate physiological conditions. To visualize the polymer degradation/erosion process, the polymer was first covalently labeled with a fluorescent dye, 1-pyrenyldiazomethane (PDAM), by dissolving 168 mg of E5005(2K) polymer in 5mL tetrahydrofuran (THF), adding 0.69 mg of PDAM in dichloromethane, and incubating overnight. The solvent was then evaporated at room temperature, and the polymer was further dried under vacuum for 3 days at room temperature. The fluorescently labeled polymer solution (9% w/w in anhydrous 1,4-dioxane) was used to coat the probe using the

procedure previously described, and the coated probes were covered with aluminum foil to prevent the fluorescent dye from photobleaching until testing. The coated probes were inserted into a 1% agarose gel phantom[117] slowly by hand and kept in a 37°C humidified incubator. Fluorescent images were obtained and monitored using an inverted microscope (Axio Observer-D1, Carl Zeiss MicroImaging GmbH, Göttingen, Germany) with a 10× objective in epifluorescent mode at different time points. The camera exposure was kept constant throughout the study. A similar procedure was used for labeling and monitoring a slow degrading control polymer E1001(1K) (E=1.8 GPa, T_g = 96°C, M_n=160K) with PDAM. The degradation profiles of E5005(2K) and E1001(1k) coated probes were quantified by performing intensity profile analysis over time using ImageJ. The intensity was normalized to the maximum intensity value within the same experiment for comparison.

Results and discussion

Polymer degradation/erosion profiles were compared between probes coated with E5005(2K) (ultrafast degrading) and E1001(1K) (slow-degrading). Figure 3-12 shows time lapse images of the SU-8 probes coated with each polymer, as well as quantitative intensity profiles indicating polymer degradation/erosion at different time points. Degradation and erosion can be seen in the intensity change over time. Meanwhile, diffusion of the polymer into the gel can be observed from the expansion of the fluorescent region surrounding the probe.

Rapid erosion/degradation was observed with the probe coated with E5005(2K) (Figure 3-12a). As shown in figure 3-12c, the E5005(2K) started to erode (intensity dropping from 100% to ~ 60%) as soon as the probe was inserted into the 1% agarose gel. 15 minutes after insertion, the polymer has eroded and diffused away from the center of the SU-8 probe with the peak intensity remained roughly the same. 60 minutes after insertion, the intensity has dropped to ~10 % and the profile was more diffuse wih the fluorescent boundary (~200 μm) from the center of the SU-8 probe. The polymer had completely eroded from the probe and diffused into the agarose gel with minimal fluorescence signal observed after 120 minutes. The SU-8 probe can be clearly identified in the image after 120 minutes without mechanical or material disruption indicating the polymer coating and erosion/degradation did not affect probe integrity.

In contrast, the intensity for E1001(1K) between 0 minute and 30 minutes was approximately the same, indicating minimal erosion 30 minutes after insertion (Figure 3-12b and 3-12d). The polymer remained 20 hours after insertion and was found to swell and expand, but did not diffuse away from the probe. Interestingly, the intensity was found to be higher 20 hours after device insertion. This may be due to differences in the degradation and erosion rates, which may have led to an observable overlap of fluorescence in different layers of the slow-degrading polymer. Regardless, the experiment confirmed that the E5005(2K) coated SU-8 probe was able to penetrate the phantom brain tissue surrogate without device disruption and polymer degraded/erode within 2 hours leaving the probe intact within the tissue.

The main mechanism for the polymer degradation is hydrolysis with the addition of water. 1% agarose gel was used as the brain phantom for this study and it contains less water compared to commonly used brain phantom agarose (0.6 % gel) [117]. Therefore, the polymer degradation time is considered to be slower than an in vivo environment. Chemical characterizations of the polymer coated probe within both PBS and a 1% agarose gel identify an estimated time window (60-120 minutes) for complete polymer degradation. Therefore, the experimental results can serve as a reference to inform a future *in vivo* polymer degradation study on when to sacrifice the animal for investigation.

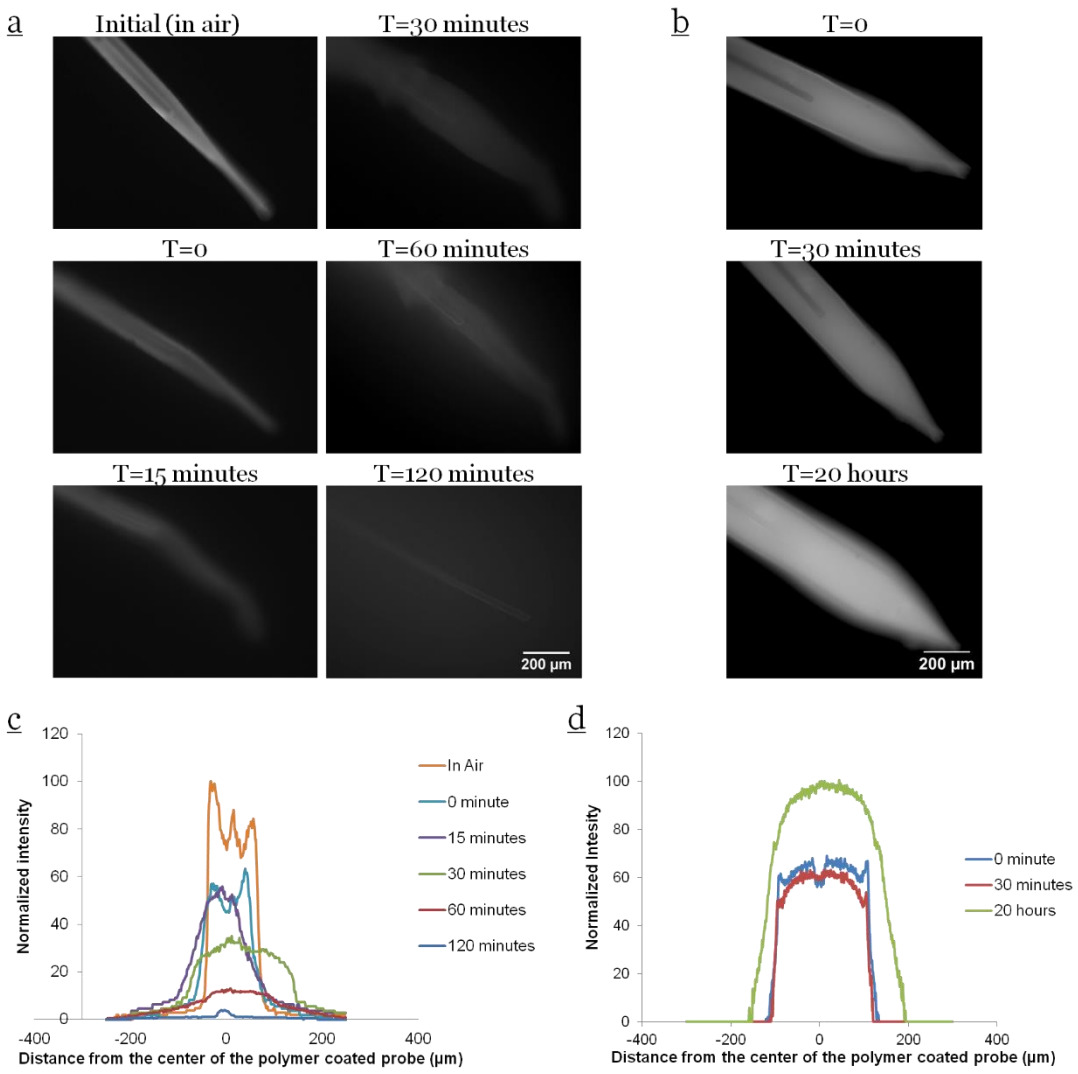

Figure 3-12: Time lapse fluorescent images of SU-8 probe coated with (a) E5005(2K) and (b) E1001(1K). Device dimension: (a) polymer shank: 100 µm wide, 100 µm thick and 3.5 mm long. SU8-probe: 30 µm wide, 20 µm thick and 3 mm long. (b) Polymer shank: 200 µm wide, 100 µm thick and 3.5 mm long. SU-8 probe: 30 µm wide, 20 µm thick and 3 mm long. (c) Intensity profile for E5005(2K) coated probe over different time points from the center of the probe.(d) Intensity profile for E1001(1K) coated probe over different time points from the center of the probe.

3.4 Extended polymer coated parylene probe fabrication procedure

3.4.1 Parylene deposition procedure

SU-8 was used as a test material for the probe because of ease of handling and access for process development. After the fabrication procedure has been designed and the polymer coated probes were characterized mechanically and chemically to ensure consistent and high yield products, the fabrication was extended and adapted to use parylene (poly(p-xylylene)) as the desired probe material. Some advantages of parylene over other conventional materials include 1) biocompatibility, 2) chemical inertness and moisture barrier, 3) conformal material (pin-hole free)[118] 4) optical transparency, 5) hydrophobic property, and 6) low dielectric constant[119]. Due to those characteristics, parylene has been widely used in many FDA-approved medical devices[120] and was chose as a probe material for this work.

The parylene deposition process consists of several different steps and the deposition is applied at room temperature and under vacuum using SCS Labcoater 2 Parylene Deposition System (Special Coating System, Indianapolis, IN, USA) (Figure 3-13). Briefly, a known mass of solid parylene dimers are heated to 150°C at 0.1 Torr and sublimed into gas phase. The gas-phased parylene dimers were then pyrolyzed at 690 °C, 0.5 Torr to cleave into monomer molecules. The parylene monomers are distributed to the deposition chamber where they polymerize and conformally coated any exposed surfaces including the probe substrate at room temperature. A cold trap at the chamber outlet condenses any excess parylene monomers and deposition by-products in order to prevent vacuum pump contamination. The coating thickness depends on mass of the loaded dimer

as well as the operating pressure during the process. For the deposition equipment at Rutgers, generally 15 grams of dimer with fine pressure control can produce a ~10 μm thick parylene film.

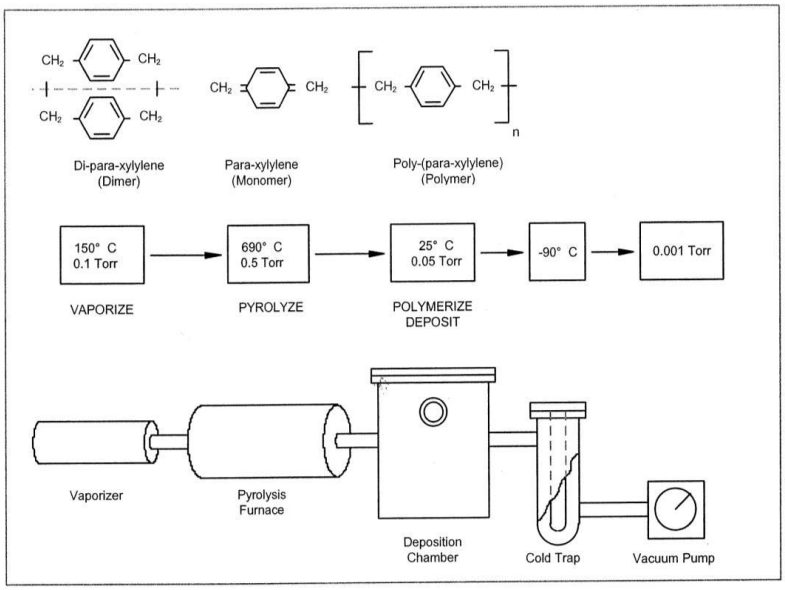

Figure 3-13: Schematic illustration of parylene deposition process.

3.4.2 Fabrication process for parylene a probe coated with the ultrafast degrading polymer

The parylene deposition process was adapted to the probe fabrication and polymer coating procedures (Figure 3-14) previously used. First, a substrate (glass slides or silicon wafers) was prepared. A thin layer (~5 μm) of parylene was deposited on the top of the substrate. A PDMS layer was not required for downstream release because parylene does not adhere to surfaces without chemical adhesion promotion. A lift-off method was used in order to define probe geometry. Briefly, a positive photoresist (Shipley S1818, Microchem Corp, Westborough, MA, USA) was deposited on the top of the parylene layer.

The probe geometry was then defined in the photoresist by photolithography. The exposed Shipley resist was dissolved by a photoresist developer (MF-319, Microchem Corp, Westborough, MA, USA). A thin aluminum metal layer was then sputtered onto the device using a physical vapor deposition system (PVD 75, Kurt J. Lesker Company, Jefferson Hills, PA, USA). Acetone dissolved the aluminum coated photoresist while the metal layer stayed adhered to the patterned areas without photoresist. The metal serves as a masking layer defining the probe geometry. An oxygen plasma was performed to the etch parylene that was not masked by the metal layer and the probe geometry can be defined. Finally, the metal masking layer was dissolved using an aluminum wet etchant. The parylene probe was coated using the same procedure as described in chapter 3.2.3. Finally, the whole device can be mechanically lifted off from the substrate using tweezers and stored for downstream process.

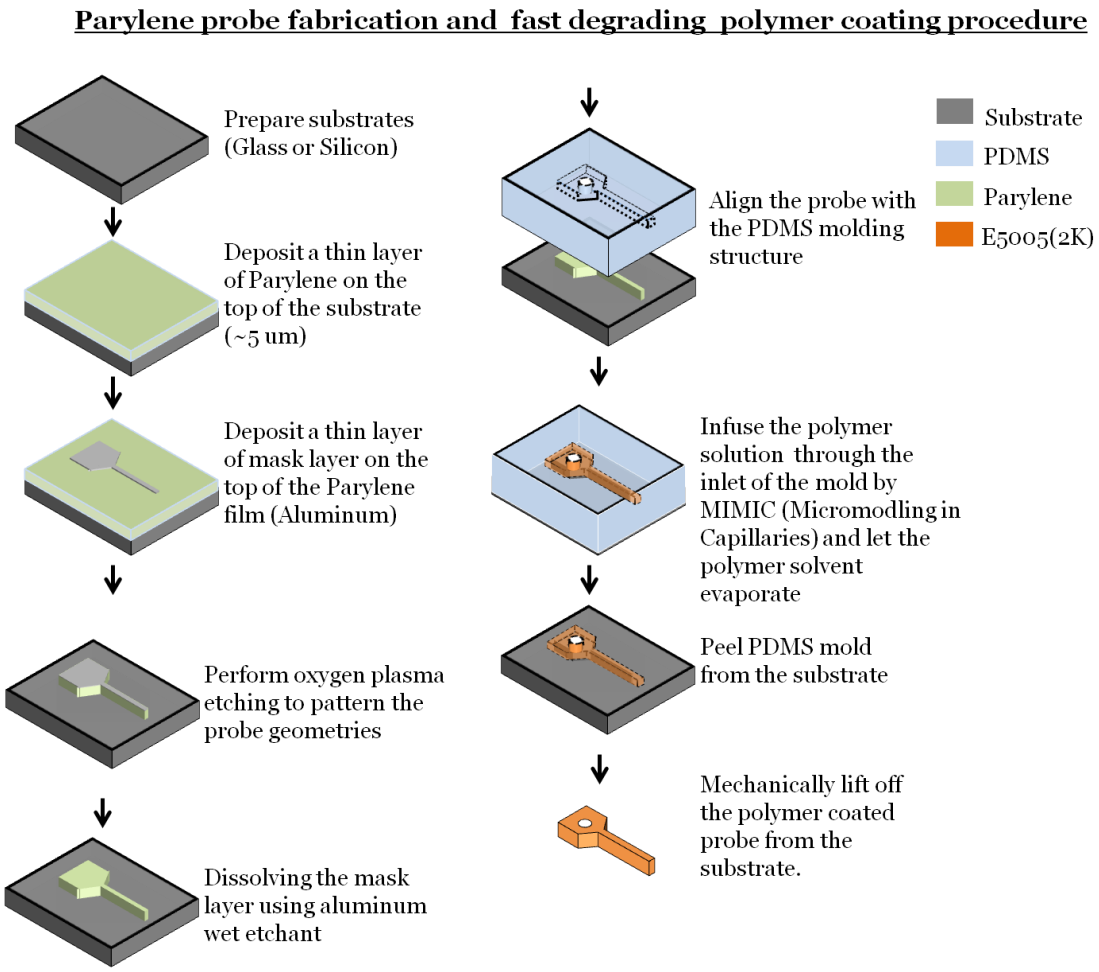

Figure 3-14: Parylene probe fabrication and polymer coating procedure. First, a thin layer of parylene was deposited. A thin aluminum mask layer that defined the probe geometry was deposited onto the top of the parylene layer through lift-off methods. Oxygen plasma etch was performed to pattern the probe. The mask layer was dissolved with a chemical etchant to complete probe fabrication. The polymer coating procedure was the same as described in the previous section (Chapter 3.2.2). The probe was coated with the polymer though micromolding in capillaries and the whole device was dried and released from the substrate.

Figure 3-15 (a) displays a parylene probe on a glass substrate. Figure 3-15 (b) displays a parylene probe coated with the E5005(2K) polymer. The polymer coating was uniform without any mechanical or material disruptions. Figure 3-15 (c) displays the zoomed-in image of the polymer coated probe from the bottom of device. The probe was located at the bottom of the substrate while being coated with the polymer; therefore the probe was encapsulated on the edge of the polymer coating. This coating procedure sometimes would cause an incomplete coating as displayed in figure 3-15 (c). However, the parylene probe can still be identified within the center of the polymer coating and there was no defect observed for both the polymer coating and the parylene probe. Moreover, the polymer coating is the main feature that withstands insertion resistance instead of the probe. Therefore, as long as the polymer coating is uniform and consistent, the probe should be able to penetrate the tissue.

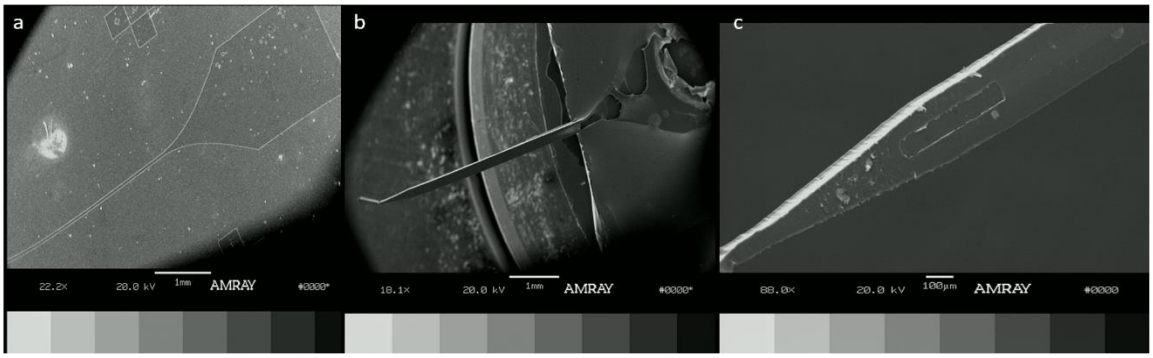

Figure 3-15: SEM micrograph of (a) a non-functional parylene probe. (b) a polymer coated probe (c) a polymer coated probe from the device backside. Device dimension: polymer shank: 100 µm wide, 100 µm thick and 4 mm long. Parylene probe: 30 µm wide, 5 µm thick and 3.5 mm long.

CHAPTER 4 IN VIVO ANIMAL STUDY

4.1 Overview

In this chapter, different probe candidates were evaluated in vivo using rat models. The purpose for the animal study is to investigate different design parameters' (probe and polymer coating dimensions) effects on tissue response progression. The study was divided into two different cohorts. First, a preliminary control experiment implanted the microwires, the ultrafast degrading polymer shanks (E5005(2K)) and the slow degrading polymer shanks (E1001(1K)). The preliminary control experiment provided insights on developing appropriate image analysis and staining protocols to properly identify implantation sites and analyze degree of cellular activation within the brain tissues by comparing the polymer shanks with the commercially available microwire devices. The second cohort implanted various probe candidates with probes encapsulated within the polymer coatings to evaluate the effect of different sized probes and encapsulation geometries on the electrode-cell interface.

For both experimental cohorts, the probe candidates were implanted. The rat brains were harvested at different time points and tissue damage (gliosis) was quantified immunohistochemically to label different cell types (astrocytes and microglia). Cell behaviors around the implantation sites were characterized by correlating image fluorescent intensity values with the cell quantity. Glial cells (astrocytes and microglia) were the main cell populations that affect probe performance during the course of

implantation. Less glial cells around the implantation sites imply better electrode-tissue incorporation and therefore are more desirable results.

4.2 Materials and Methods

4.2.1 Experimental design and device selection

The animal study was divided into two different cohorts: 1) Preliminary control experiment and 2) Probe candidate implantation experiment. The purpose for the preliminary control experiment was to compare the tissue response progression between different polymer shanks and commercially available microwires, as microwires produce predictable gliosis that has been widely characterized[121,122]. The preliminary control experiment also provided insights on how to identify specific implantation sites and confirmed the immunostaining techniques for the study.

For both experiments, 10 devices were implanted simultaneously into one single animal. In order to achieve the task, a surgical holder was designed using Solidworks to incorporate the holder with the stereotaxic apparatus, which was used to position the animals (Figure 4-1). The probes were fixed on the surgical holder using epoxy glue. Each probe was at least 2 mm apart from each other to prevent interference from adjacent tissue responses. The surgical holder along with the probes was sterilized under UV light (30 minutes on each side) to minimize infection after device implantation. The whole device was vacuum sealed and stored in – 20°C refrigerator until surgery. Each device was thawed

under vacuum 15 minutes prior to device implantation to prevent moisture and heat from damaging the polymer coatings.

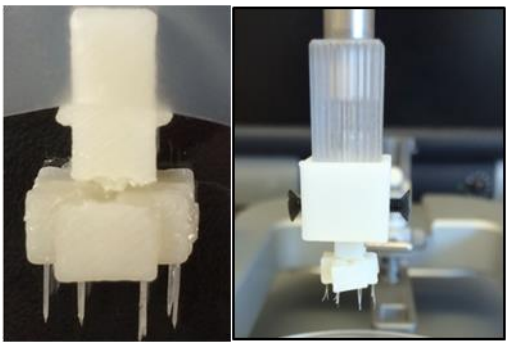

Figure 4-1: (Left) The customized surgical holder with 10 devices fixed on it. (Right) The customized surgical holder and headstage incorporated with a standard stereotaxic station.

For the preliminary control experiment, figure 4-2 displays the experimental design of different device types and their fixation locations on the surgical holder. Six microwires were fixed on the edge of the holder. Four polymer shanks with different dimensions and polymer types (E5005(2K) and E1001(1K)) were fixed at the center of the surgical holder.

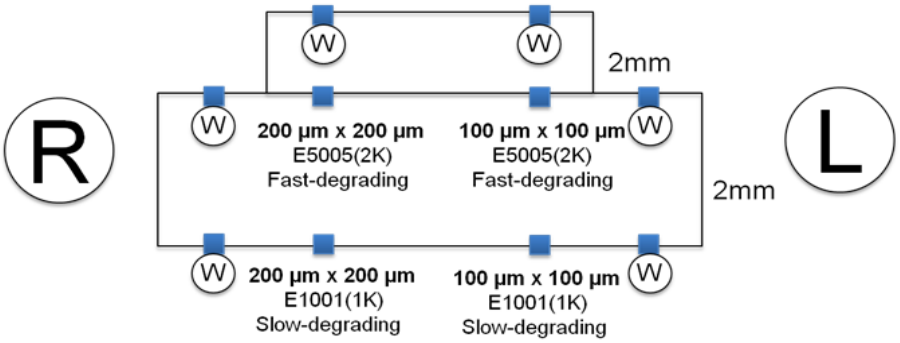

Figure 4-2: The experimental design of different device types and their fixation locations on the surgical holder. w: microwires dimension : 50 µm in diameter and 4 mm long. Polymer coating dimensions : various widths and heights as indicated ; 4 mm long.

For the probe candidate implantation experiment, five different groups with varying probe and polymer sizes were selected (Table 4-1). The polymer used for this study was the ultrafast degrading polymer (E5005(2K)). The goal for the study is to investigate how probe and polymer coating sizes affect gliosis. The larger and smaller polymer coatings with the same sized probe can help understand whether the initial mechanical trauma induced by the polymer coating plays a role in long term glial layer formation, as the polymer coating rapidly degrades within a couple hours following device implantation. On the other hand, the different sized probes (no probe, 30 µm and 80 µm wide) encapsulated within the same polymer coating size can help to understand how cells react to different sized probes from both short and long term tissue response. Probes with larger dimensions (group 5) matched the dimensions of several other parylene probes found in the literature[90,123] and was therefore selected as a control reference. One important aspect of the device design with different probe sizes is the trade-off effect between the device

consistency and efficiency. It is hypothesized that the smaller probes would induce less tissue response. However, the smaller probes would limit the number of electrodes that can be incorporated within the probe. Fewer electrodes imply less information can be extracted simultaneously from the device and therefore could decrease signal recording efficiency. Both smaller and larger probes would potentially induce tissue responses, so it is important to investigate whether the tissue response are significantly more severe for the larger devices. The ultimate desired outcome for this work would be to maximize the probe size allowing multiple electrodes incorporation for high signal recording efficiency while attenuating the tissue response for long term recording consistency. If the tissue response induced by the smaller probe is not significantly improved, a larger probe would be a more desirable candidate balancing the trade-off effect between the recording efficiency and consistency.

Most conventional neural probes have the impedances around 1 MΩ at 1 kHz. Previous studies have shown that a recording area of 400 to 600 μm^2 is typical in order to obtain approximately 1 MΩ impedance[77,124]. The width of the probe must be kept at least 20 µm to maintain the recording fidelity while minimizing the probe size, so that a 400 μm^2 recording electrode can be fabricated. Therefore, a 30 µm wide probe was considered the minimum size to support a 20 µm wide recording site. The probe width is a limiting factor due to the electrode patterning feasibility; however, the probe thickness can be further minimized to ~ 5 to10 µm to decrease probe rigidity.

Table 4-1: Polymer (E5005(2K)) coated parylene probe candidate for the animal study

Group	Parylene probe dimensions	Polymer coating dimension
1	30 µm × 5 µm × 3.5 mm	100 µm × 100 µm × 4 mm
2	80 µm × 5 µm × 3.5 mm	100 µm × 100 µm × 4 mm
3	30 µm × 5 µm × 3.5 mm	200 µm × 200 µm × 4 mm
4	None	100 µm × 100 µm × 4 mm
5	320 µm × 5 µm × 3.5 mm	350 µm × 100 µm × 4 mm

4.2.2 Surgical procedure

All the surgical procedures were approved by the Rutgers Institutional Animal Care and Use Committee (IACUC). 18 animals (Sprague-Dawley rat; Charles River Labs, Wilmington, MA, USA) were used for the study. For each implantation, the animal was first anesthetized by 5% isoflurane gas. Ketamine (100 mg/mL) and xylazine (10 mg/mL) were administered intraperitoneally for prolonged anesthesia (Figure 4-3). The animal's head was shaved from between the eyes to behind the ears and then fixed on a stereotaxic station. An incision was made through the midline of the calvaria. The bregma was identified as the reference point for the craniotomy. 4 craniotomies were drilled (Two anterior to bregma and two posterior to lambda) and fixed with screws for better head stage attachment to the calvaria. Two craniotomies (Figure 4-4) were drilled 1.5 mm from the midline on each hemisphere anterior to the bregma. The implantation location was selected due to the brain homogeneity in this region, and therefore tissue variability could be minimized between the different probes and animals.

The craniotomies were filled with saline to prevent dehydration. In order to minimize the contact between the humid-sensitive polymer coated probes to the ambient environment, a surrogate surgical holder with 10 non-degradable polymer coated probes was fixed on the stereotaxic manipulator. The implantation location was then adjusted using the stereotaxic manipulator to align with the craniotomies (x-y coordinates). Dura was removed prior to device implantation and the craniotomies were dried using gauze. The surrogate surgical holder was replaced with the holder containing the 10 probes of interest. The device was inserted manually (at a rate of ~ 2 mm/min) into the craniotomies. Dental cement (Stoelting Co., Wood Dale, IL, USA) was applied to fix the holder to the calvaria and the wound was sutured. The animal was placed on a water-perfused heating pad until recovery from anesthesia.

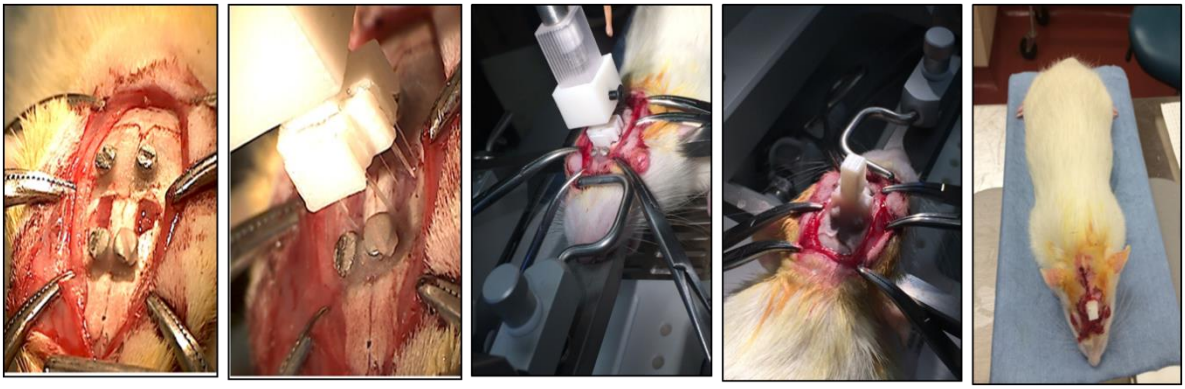

Figure 4-3: Surgical procedure for the animal study. Two craniotomies were drilled. 10 probes with different dimensions were implanted simultaneously via the customed designed surgical holder. Dental cement was used to fix the surgical holder and the wound was sutured. The animal was placed on warm heat pad until recovery from anesthesia.

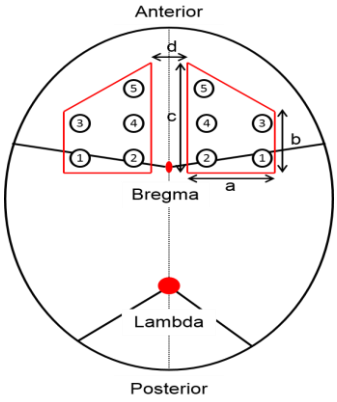

Figure 4-4: Location and dimension of the two craniotomy holes and the 10 probes (Table 4-1 for reference) with different dimensions. a= 4 mm ; b=4 mm; c= 6 mm; d=3 mm.

4.2.3 Tissue processing and immunohistochemistry

For the preliminary control experiment, surgeries were performed on two animals and sacrificed separately at two time points: 72 hours and 4 weeks. For the probe candidate implantation experiment, animals were sacrificed at six discrete time points (72 hours (n=3), 10 days (n=3), 3 weeks (n=3), 7 weeks (n=3), 12 weeks (n=3), 24 weeks (n=3)). The animal was first anesthetized using overdosed pentobarbital. Once the animal reached a surgical plane of anesthesia, it was perfused with room temperature PBS followed by 4 % paraformaldehyde (4°C). The animal was then decapitated and the surgical head stage was removed manually. The whole brain was extracted from the skull and fixed within 4% formaldehyde for 48 hours and then transferred into sucrose until sectioning.

Brain tissue was sectioned transversely into 30 µm slices. Slices were collected and stained 1.5 mm, 2 mm and 2.5 mm inferior from the surface of the brain. Immunohistochemistry was performed on three different consecutive tissue slices labeling

different cell types at different depths (Table 4-2). For slice one, primary antibodies were specific to astrocytes and endothelial cells 1) astrocytes, polyclonal chicken anti-Glial Fibrillary Acidic Protein (GFAP) (Cat#GFAP, dilution 1:500, Aves Lab, Tigard, OR, USA); 2) endothelial cells , polyclonal rabbit anti-human Von Willebrand Factor , (Cat#A0082, dilution 1:200 , Dako North America Inc., Carpinteria, CA, USA). Secondary antibodies were 1) goat anti-chicken IgY (H+L) (Alexa 647, Cat#A-21449, dilution 1:500, Life Technologies Inc, Grand Island, NY, USA); 2) goat anti-rabbit IgY (H+L) (Alexa 488 Cat#A11008, dilution 1:500, Life Technologies Inc, Grand Island, NY, USA). For slice two, the primary antibody was specific to neurons, polyclonal rabbit anti-NeuN (Cat # ab104225, dilution 1:500, Abcam Inc., Cambridge, MA, USA) and the secondary antibody is goat anti-rabbit goat anti-rabbit IgY (H+L) (Alexa 488 Cat#A11008, dilution 1:500, Life Technologies Inc, Grand Island, NY, USA). For slice three, the primary antibody was specific to microglia both activated and inactivated), polyclonal rabbit anti-Iba1 (Cat#CTK6675, dilution 1:200, Wako Inc., Richomond, VA) and the secondary antibody are 1) goat anti-rabbit IgY (H+L) (Alexa 568 Cat#A11011, dilution 1:500, Life Technologies Inc, Grand Island, NY, USA); 2) Fluoro-Gel with DAPI (Cat#17985-50, dilution 1:500, Electron Microscopy Sciences Inc., Hatfield, PA. USA). Sections were mounted on to glass slides for downstream fluorescent imaging.

The staining protocol was designed so that there were no more than two stains on each slice to prevent interference between different cell types during imaging. Astrocytes were imaged using a Cy5 filter. Microglia was imaged using a RFP filter. Both neurons and endothelial cells were imaged using a GFP filter and all cell nuclei were imaged using

a DAPI filter (Table 4-2, Figure 4-5). Neurons and endothelial cells were processed on difference slices to prevent interference. Astrocytes and endothelial cells were processed on the same slice due to the wide separation between the emission spectra of each secondary antibody used to label each cell types tagged on both cells.

Table 4-2: Immunohistochemistry staining protocol. Each depth included three consecutive slices stained with different cell types. Slice one stained astrocytes and endothelial cells. Slice two stained neurons. Slice three stained microglia and all nuclei.

Staining Combination	Depth (30 µm Slice #)	Cell Type	Protein/ Target	Antibodies	Fluorophore (nm)	Filter	Color Applied
1	1.5 mm (45) 2 mm (66) 2.5 mm (75)	Astrocytes	GFAP	Chicken polyclonal	Alexa 647	CY5 (far red)	RED
		Endothelial cell	vWF VIII	Rabbit polyclonal (Dako)	Alexa 488	GFP (green)	GREEN
2	1.5 mm (46) 2 mm (67) 2.5 mm (76)	Neuron nuclei	NeuN	Rabbit polyclonal	Alexa 488	GFP (green)	GREEN
3	1.5 mm (47) 2 mm (68) 2.5 mm (77)	Microglia	Iba-1	Rabbit polyclonal (Wako)	Alexa 568	RFP (red)	ORANGE
		All nuclei	DAPI	[Dye]	[345]	DAPI (UV)	BLUE

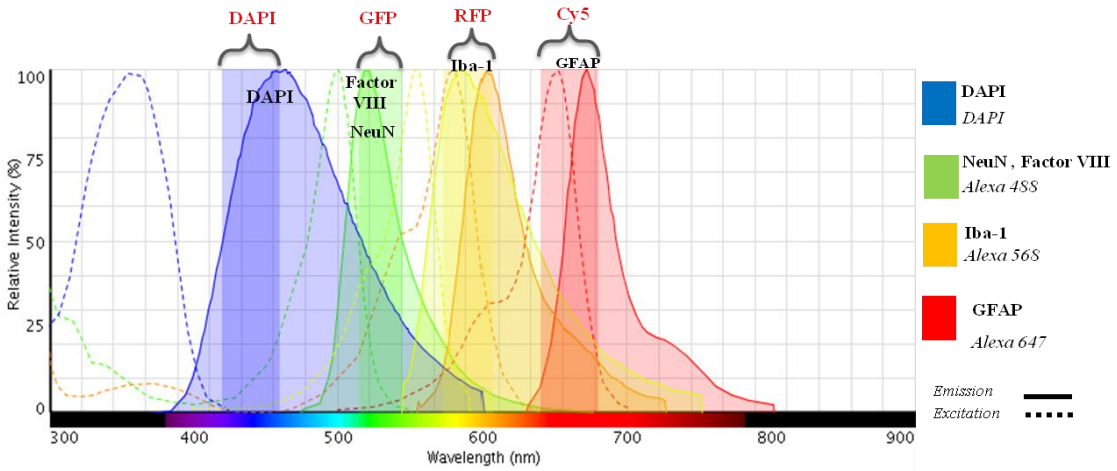

Figure 4-5: Fluorescent spectra of different secondary antbodies conjugated with different cell types and spectra range of different imaging filters (DAPI; GFP; RFP; Cy5).

Figure 4-6 displays representative images of the brain tissue staining with each cell types. Astrocyte is the main cell type of interest for this work because they migrate towards implantation site and form the encapsulation layer around the implants. Microglia was stained to monitor both the short-term wound healing process as well as the long term neuro-inflammation. Neurons were stained to investigate if there is any neuronal loss around the implantation sites that might affect the neural probe's functionality. The morphology of blood vessels on a horizontal brain slice is similar to a possible implantation site. Therefore, endothelial cells were stained to distinguish the implantation sites from blood vessels.

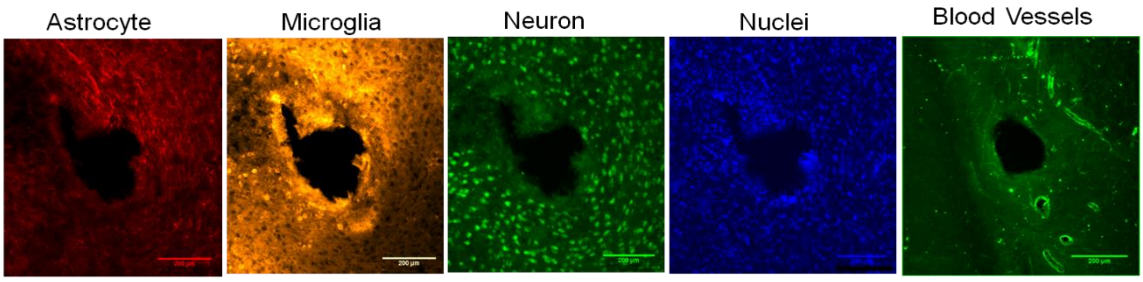

Figure 4-6: Representative images of tissue staining with different cell types (Astrocytes, Microglia, Neurons and Cell nuclei).

4.2.4 Imaging protocol

An imaging protocol was designed to process the brain samples which can be divided into different steps. All histological images were acquired by an inverted fluorescence microscope (Olympus IX-81, Waltham, MA, USA). The brain slice was first imaged. Due to the large size of the sample, it can be imaged by acquiring multiple images across the area of the brain and then stitching them into a montage image (Figure 4-7).

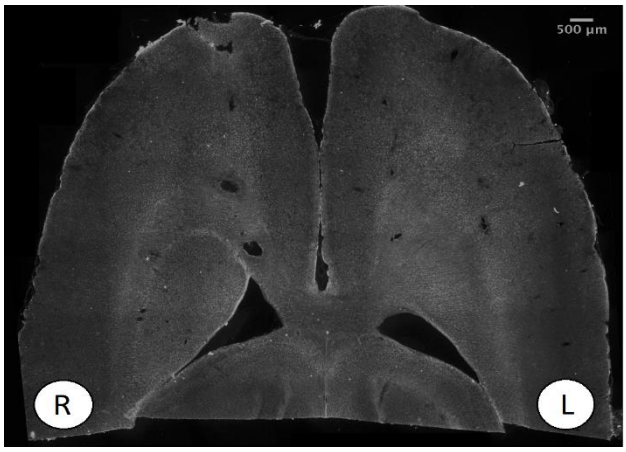

Figure 4-7: Representative image of a montage brain slices. Sample ID: 72-hour control animal at 2 mm deep from the surface of the brain stained with GFAP (astrocytes). R and L indicated right hemisphere and left hemisphere brain for the animal.

After the sample was imaged, a grid was applied to identify individual implantation sites (Figure 4-8). The grid was consist of ten 1 mm × 1 mm squares that were 1 mm separated from each other and oriented according to the surgical holder that was used to fix the probes. The midline of the grid was aligned with the midline of the brain slice and the square regions of interests (ROI) indicated possible implantation locations for each implanted probe. The ROI provides only an approximate location for the implantation sites. Different factors can affect the locations of the actual implantation sites. First, the probe candidates were both fixed on the surgical holder and inserted into rat brain manually and so there may be human errors involved causing a non-vertical device implantation. Second, when the brain sample was sectioned, it may not be positioned perfectly horizontal, which would cause the implantation site to shift its location if the tissue was sectioned at an angle. Despite these factors, the grid application is useful to help identify implantation sites for downstream image processing.

After the implantation sites were identified, magnified images at each site were obtained. These images were analyzed to quantify cell behaviors around implantation sites between the different probe candidates and cell types at higher microscopic resolution (10X).

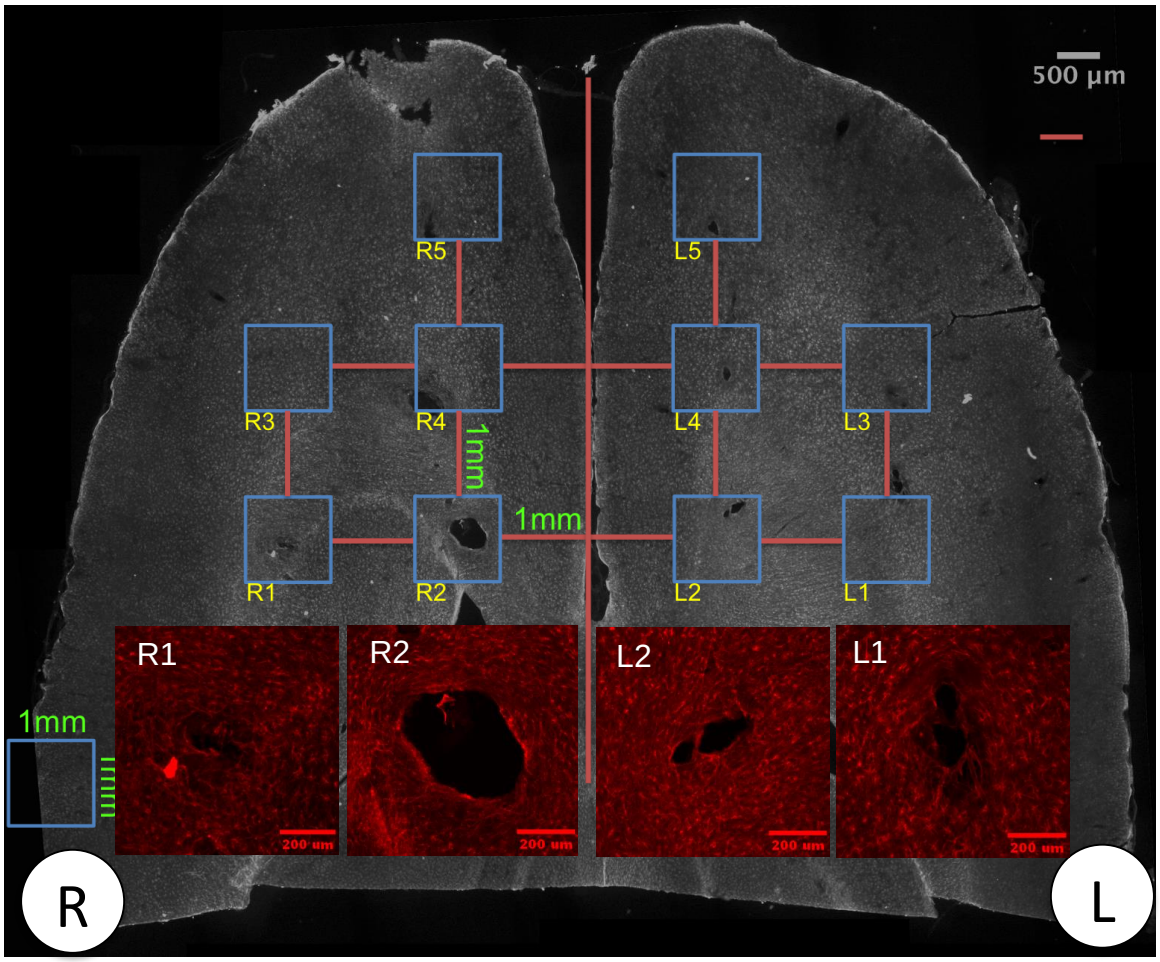

Figure 4-8: Representative image of 1) a montage of brain slices with a grid application for implantation site identification. 2) Magnified images of several implantation sites for downstream image analysis process. Sample ID: 72-hour control animal at 2 mm deep from the surface of the brain stained with GFAP (astrocytes). R and L indicated right hemisphere and left hemisphere brain for the animal.

4.2.5 Image and data analysis

Image analysis was performed to quantify cell behaviors by correlating immunohistological staining florescence image intensity with cell quantity, in which a higher intensity implies a larger number of cells at a specific location. A customized Matlab script was developed to perform a rotational intensity sweep profile analysis on each individual implantation site image (Figure 4-9). First, the implantation site was segmented by thresholding to identify the implantation site, which was usually a void shape with low intensity. The centroid of the implantation site was identified and set as the starting point for the analysis. An end point was defined at 800 μm from the starting point which reached into an undamaged brain region. The end point was selected so that the undamaged brain region intensity can serve as a control reference. Intensity values were obtained along at line trace defined from the starting to the end points. The intensity was averaged in a circular fashion by rotating the line with a small angle step and repeating the intensity quantification. The analysis was performed for a full circle sweep. The intensity values were then averaged between each different line trace and plotted with respect to the distance from the center of the implantation site.

The raw intensity data was further processed for comparison between different images/devices/rats. The intensity values were normalized to the undamaged area, which was obtained by averaging the last ~200 μm intensity values. The normalization was performed to accommodate different intensity values of the undamaged area between different images. Figure 4-10 displays a representative result obtained from the image

analysis algorithm. The intensity value at the center of the implantation site was usually lower than the undamaged area due to tissue damage by device implantation. Therefore, the distance over which the normalized intensity was less than 1 suggested the radius of the wound. The intensity values increased once the line reached the tissue layer. The cell behaviors around the implantation sites would be the region of interest since this can suggest the degree of gliosis. The results from figure 4-10 indicate a cell density increase of ~ 4.5 around the implantation site compared to the undamaged area. As the distance from the center of the implantation site increased, the intensity values diminished and eventually reached the steady state intensity comparable to the undamaged area.

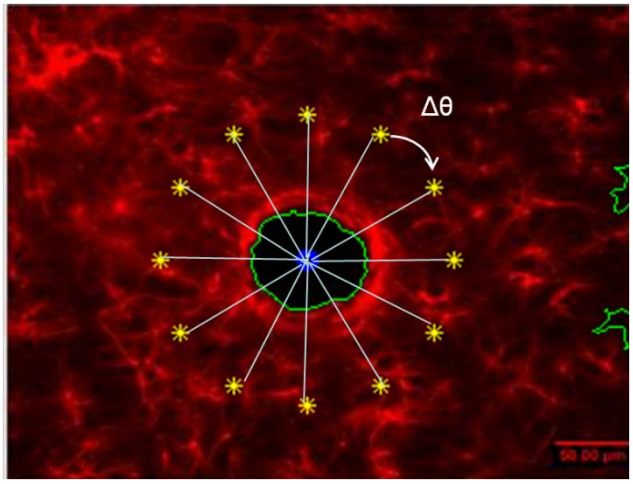

Figure 4-9: Rotational intensity sweep profile anaysis. The implantation site was ideintified through thresholding and the centroid was identified. An end point reaching the undamaged area was defined and an intensity profile along the line was obtained. The same analysis was repeated by rotating the line with small angle step in a full circle. The intesity values were averaged and plotted with respect to the distance from the center of the implantation site.

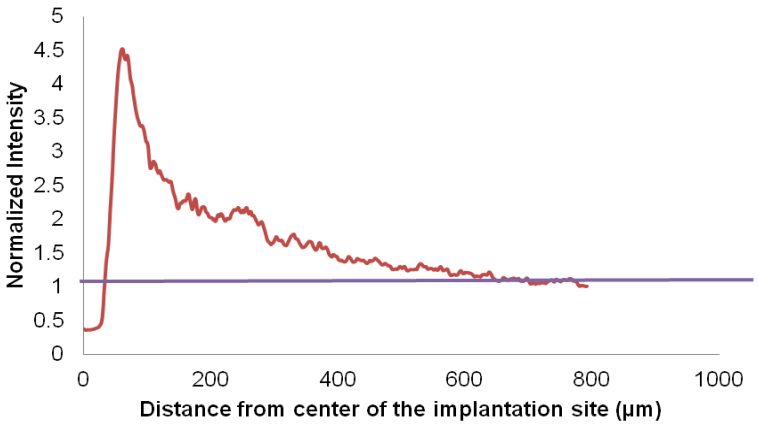

Figure 4-10: Represensative data showing normalized intensity vs. distance from the center of the implantation site. The intensity values were normalized by the undamaged area , which was denoted with a value of 1.

Results obtained from the method described above investigated the cell behavior around the implantation site for various probe and coating sizes with respect to the distance from the center of the implantation site. The data were further processed by obtaining a single representative intensity value for comparison between different devices, animals and time points. This value was obtained by calculating the area under the curve above a value of 1 (Figure 4-11), which indicates the image area where cell density is greater so that they have intensity values comparably larger than the undamaged area within the region of the interest.

Statistical analysis was performed to compare different parameters. Analysis of variance (ANOVA) with a p-value of 0.05 was performed between different animals within the same device and time point. An unequal variance t-test with p-value of 0.05 was

conducted to compare between different devices at the same time point and different time points for the same device.

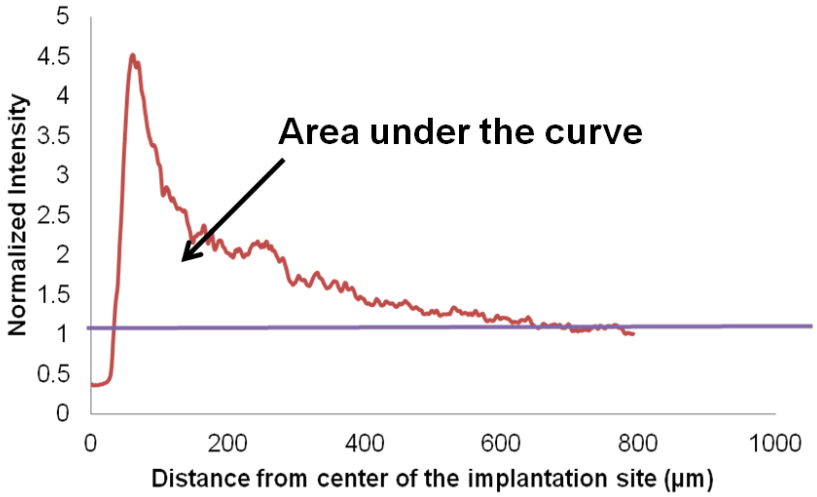

Figure 4-11: Represensative data showing normalized intensity vs. distance from the center of the implantation site. Area under the cruve above was obtained to represent the amount of cells that show comparably higher fluorescence than the undamaged area within the region of the interest.

4.3 Results and discussion

4.3.1 Preliminary control experiment

Figure 4-12 displays the GFAP staining (for astrocytes) images for the three devices (the microwire, the slow-degrading polymer shank and the fast-degrading polymer shank) at two different time points (72 hour and 4 week post device implantation). The dimension of the microwire was 50 μm in diameter and 4 mm long. The dimension of the polymer shanks were 200 μm wide, 200 μm thick and 4 mm long. 72 hour after device implantation, the wound size for the microwire (~ 80 μm) was much smaller than the polymer shanks (~ 350 μm) (Figure 4-13). This resulted from the much larger device dimensions for the polymer shanks. The initial mechanical trauma caused by device implantation played an important role at the early stage tissue response and therefore larger wound sizes were seen for the polymer shanks compared to the microwire as expected. Furthermore, the wound sizes for both the slow-degrading and fast-degrading polymer shanks were larger than the device dimensions. This may be due to the polymer swelling from water absorption within the tissue causing more severe tissue damage at early time points. 4 weeks after device implantation, the wound size for the microwire stayed approximately the same. However, the wound sizes for both polymer shanks decreased to similar sizes compared to the microwire. This was mainly due to wound healing process where the tissue started to recover from the mechanical insult during device implantation.

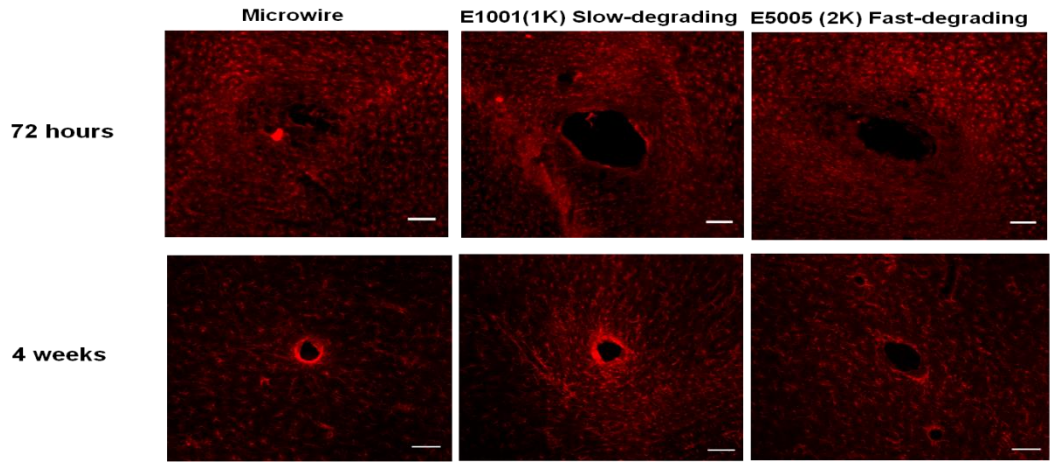

Figure 4-12: GFAP staining (for astrocytes) images for three difference devices (the microwire, slow-degrading polymer shank and fast-degrading polymer shank) at two different time points (72 hour and 4 week post device implantation). Device dimension: The microwire: 50 µm in diameter and 4 mm long. The polymer shanks: 200 µm wide, 200 µm thick and 4 mm long.

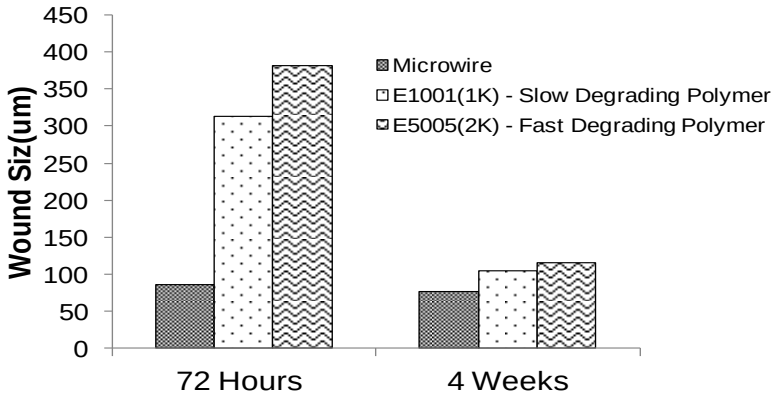

Figure 4-13: The wound size for the three devices (the microwire, slow-degrading polymer shank and fast-degrading polymer shank) at two different time points (72 hour and 4 week post device implantation). Device dimension: The microwire: 50 µm in diameter and 4 mm long. The polymer shanks: 200 µm wide, 200 µm thick and 4 mm long.

Figure 4-14 displays the normalized fluorescence intensity from the center of the implantation site following GFAP staining for astrocytes. At the 72 hour time point, the peak intensity values around the implantation sites for all three devices (the microwire, slow-degrading and fast-degrading polymer shank) were approximately the same at ~1.2, indicating approximately 20% more cell density than the undamaged area. Astrocytes are activated upon device implantation to trigger series of cascade tissue response. However, it usually takes couple weeks or months before astrocytes migrate toward the implantation sites to form glial scar, therefore, there were no distinctive differences between the three devices during the early stage response at 72 hours. At the 4 week time point, the peak intensity values for both the slow-degrading polymer shank and the microwire were ~5, indicating astrocyte density 5 times greater than the undamaged area. In comparison, the peak intensity value for the fast-degrading polymer shank was ~ 2, indicating an astrocyte density around the implantation site double the undamaged area.

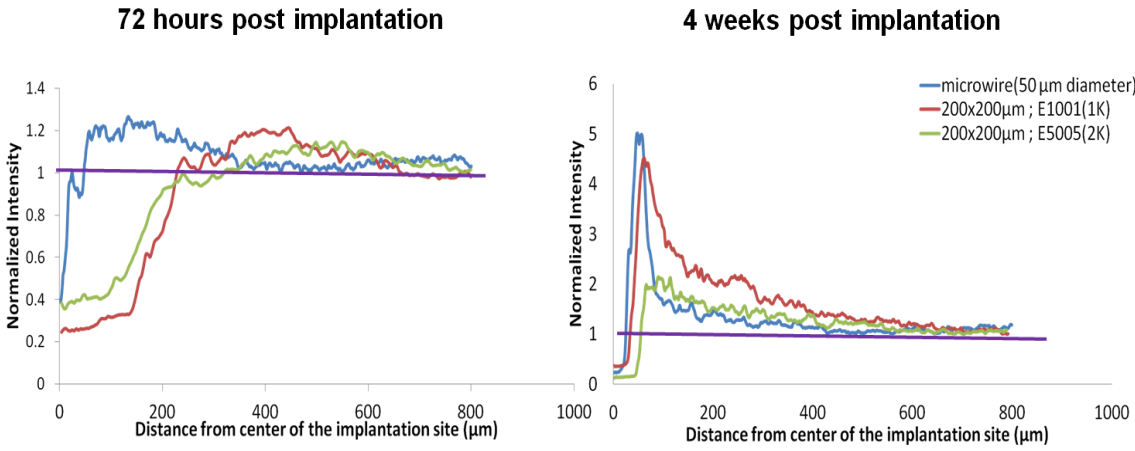

Figure 4-14: The intensity over the distance from the center of the implantation site with GFAP staining for three different devices (the microwire, slow-degrading polymer shank and fast-degrading polymer shank) at two different time points (72 hour and 4 week post device implantation). Device dimension: The microwire: 50 µm in diameter and 4 mm long. The polymer shanks: 200 µm wide, 200 µm thick and 4 mm long.

The fast-degrading polymer shank was observed to induce a diminished tissue response in terms of astrocyte aggregation compared to both the slow-degrading polymer shank and the microwire. The fast-degrading polymer shank degraded within couple hours following device implantation whereas the slow-degrading polymer would take approximately 8-12 months before completely degrading within the tissue. The slow-degrading polymer shank was not degraded at the 4 week time point and therefore astrocytes reacted to the undissolved shank and induced a more severe glial response. These results also suggested and confirmed that the fast-degrading polymer (E5005(2K))

would be a more ideal coating material compared to the slow-degrading polymer (E1001(1K)).

When initially implanted, the microwire caused less mechanical insult due to its smaller device dimension. However, the mechanical mismatch (high material modulus) and/or micromotion generated between the microwire and adjacent tissue had an effect in triggering a more severe astrocyte reaction and therefore a more severe glial response was observed. These results suggest that the pure fast-degrading polymer shank induce less glial scar response than the microwire up to 4 week following device implantation even with a larger initial device dimension.

The same analysis was performed to investigate microglia behavior in response to the three different devices at 72 hour and 4 week post device implantation (Figure 4-15 and Figure 4-16). The microglia serves as an indicator for both the short-term wound healing response (days after implantation) as well as the long term neuro-inflammation response. At the 72 hour time point, the peak intensity values around the implantation sites for the slow-degrading polymer shank and the microwire were ~ 2, indicating a doubling of the microglia density compared to the undamaged area. The peak intensity value for the fast-degrading polymer shank was ~ 1.5, indicating a 50% increase in microglia density than the undamaged area. At the 4 week time point , the peak intensity values around the implantation sites for the slow-degrading polymer shank and the microwire were ~ 3, indicating 3 fold increase in microglia density than the undamaged area whereas the peak

intensity value stayed approximately the same at 1.5 for the fast-degrading polymer shank at both time points.

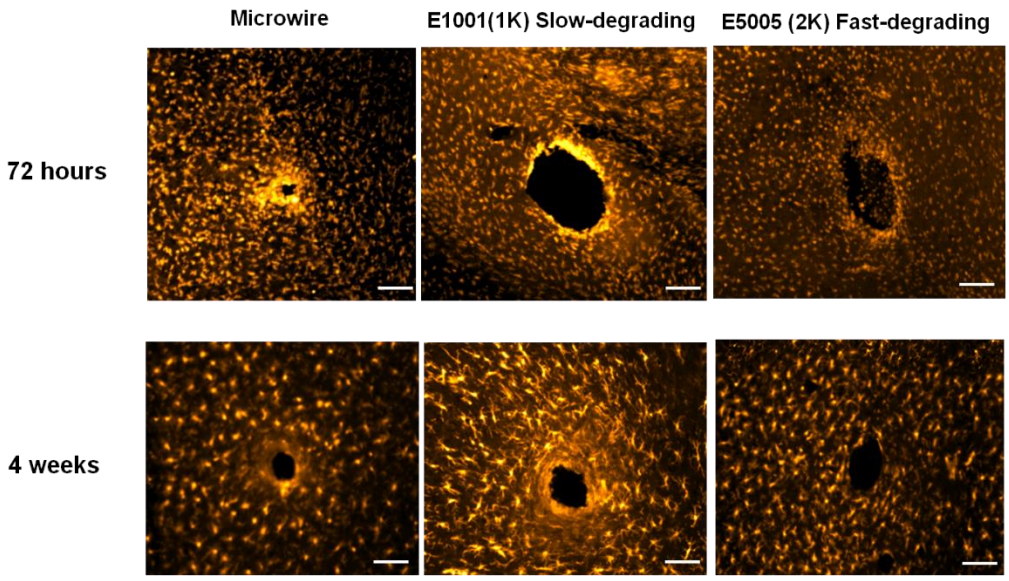

Figure 4-15: Iba-1 staining (for microglia) images for three different devices (the microwire, slow-degrading polymer shank and fast-degrading polymer shank) at two different time points (72 hour and 4 week post device implantation). Device dimension: The microwire: 50 µm in diameter and 4 mm long. The polymer shanks: 200 µm wide, 200 µm thick and 4 mm long.

At the early time point, the microglia is more active compared to astrocytes around the implantation site to aid in the wound healing response and to phagocytose damaged tissues. A higher peak intensity values was therefore observed across all three devices compared to astrocytes peak intensity values. The wound healing response is a short term effect that usually subsides couple of days/weeks following device implantation. A long term effect of microglia activation indicates neuro-inflammation, which can be observed

for all three devices 4 weeks following device implantation. However, the results shown in figure 4-16 agreed that both the slow-degrading shank and the microwire exhibited a more severe tissue response (more glial cells around the implantation sites) than the fast-degrading polymer shank, which is consistent with the conclusion drawn from the astrocyte staining.

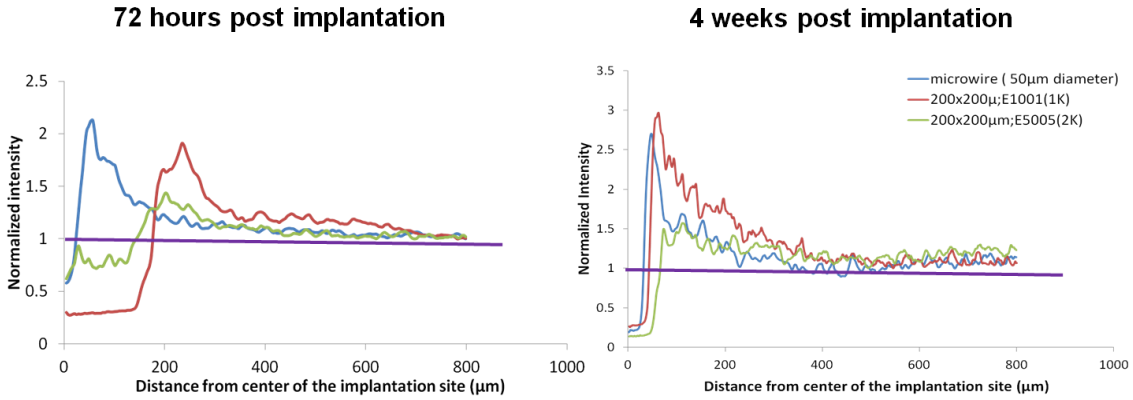

Figure 4-16: The intensity over the distance from the center of the implantation site with Iba-1 staining for the microwire, slow-degrading polymer shank and fast-degrading polymer shank at two different time points (72 hour and 4 week post device implantation). Device dimension: The microwire: 50 µm in diameter and 4 mm long. The polymer shanks: 200 µm wide, 200 µm thick and 4 mm long.

In summary, the preliminary control experiment compared the tissue response of pure polymer shanks with commercially available microwires that produce predictable gliosis to confirm the immunostaining techniques. The experimental results confirmed the polymer selection of E5005(2K) as an insertion shuttle material while suggesting E5005(2K) exhibited better electrode-cell incorporation up to 4 weeks following device implantation than the microwire even while using a larger device dimension.

4.3.2 Probe candidate implantation experiment

For the probe candidate implantation experiment, duplicate of five devices (total of 10) with different dimensions were implanted into one single animal's brain. Three animals were sacrificed at six time points (72 hour, 10 days, 3 weeks, 7 weeks, 12 weeks and 24 weeks post implantation) for histological analysis.

4.3.2.1 Glial cell response – Astrocyte

Astrocyte activation was quantified using Glial fibrillary acidic protein (GFAP). 72 hour after device implantation, the GFAP staining displayed small amount of astrocytes around the implantation sites for all five devices (Figure 4-17). The results were as expected. At early time points, astrocytes were activated but it would take couple days/weeks before the astrocytes began to form a glial scar around the implantation sites. Furthermore, at 72 hours the astrocytes were less condensed adjacent to the implantation sites (~ 100 μm) for all the devices compared to the undamaged area. This might result from 1) tissue necrosis caused by the insertion mechanical trauma or 2) other types of cells other than astrocytes occupying within the region (results presented in the next section). In general, there were no distinctive differences between devices 72 hours post implantation. 10 days after device implantation, the wounds began to heal and close for all the devices (Figure 4-18). All five devices experienced increase of astrocyte intensity around the implantation sites. The devices with larger polymer coatings , device 3 (200 μm × 200 μm coating) and 5 (350 μm × 100 μm coating) exhibited less condensed astrocyte density around the implantation sites than the devices with smaller polymer coatings , devices 1, 2

and 4 each with a 100 μm × 100 μm coating. The devices with larger coatings created larger wounds during device insertion, and therefore, the wound healing time course would be prolonged compared to the smaller polymer coating devices.

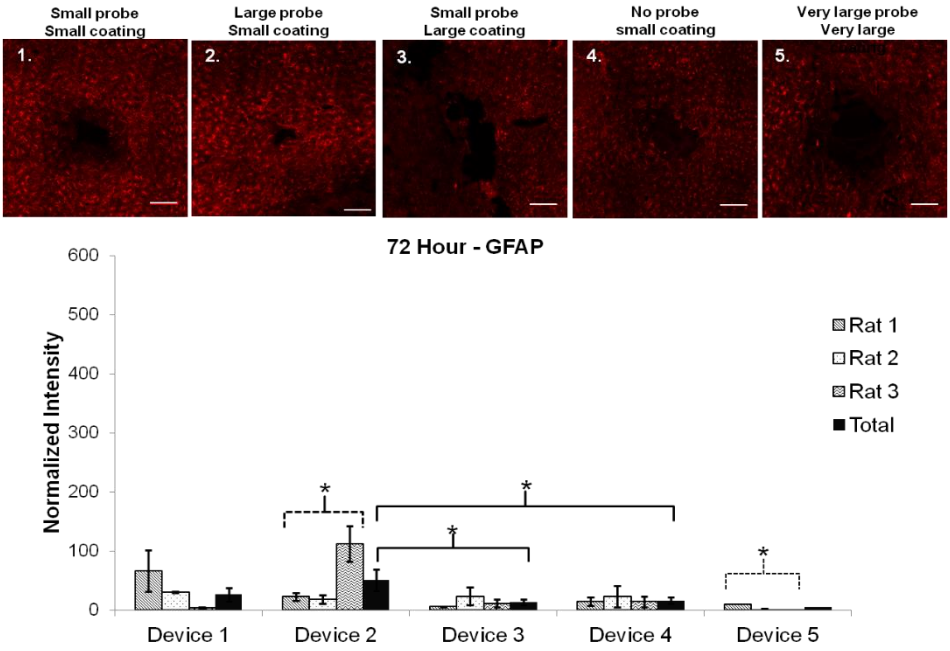

Figure 4-17: Normalized intensity of GFAP staining vs. different devices/rats 72 hour post implantation. Dashed line: statistical significance ($p<0.05$) between animals within an experimental group. Solid line: significance between devices across experimental groups ($p<0.05$). Scale bar : 200 μm.

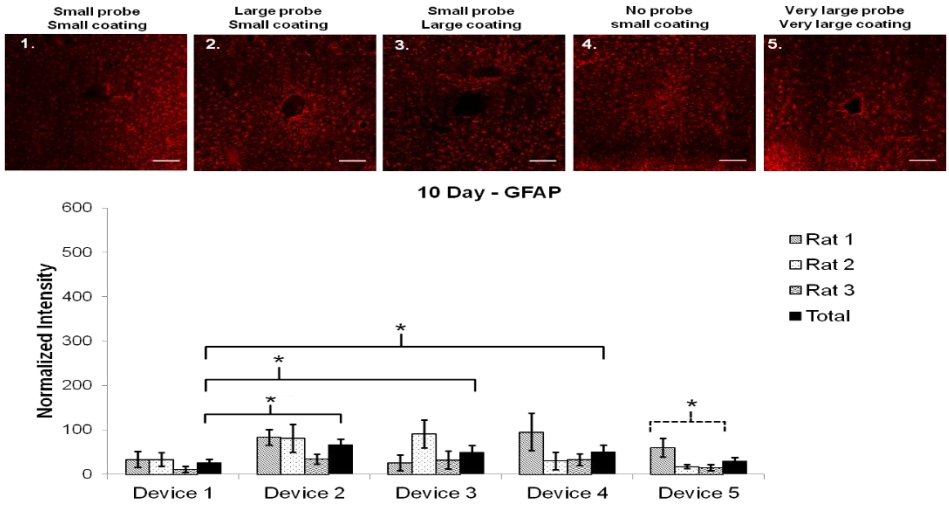

Figure 4-18: Normalized intensity of GFAP staining vs. different devices/rats 10 days post implantation Dashed line: statistical significance ($p<0.05$) between animals within an experimental group. Solid line: significance between devices across experimental groups ($p<0.05$). Scale bar : 200 µm.

3 weeks after device implantation, the astrocyte distribution started to vary between different devices (Figure 4-19). An astrocyte sheath layer formed around the devices containing the larger coatings (Device 3 (200 × 200 µm coating) and 5 (350 × 100 µm coating)). There was a statistical astrocyte intensity difference between device 1, the small probe (30 × 5 µm probe) with the small coating (100 × 100 µm coating) and device 3, the small probe (30 × 5 µm probe) with the large coating (200 × 200 µm coating), indicating the initial mechanical trauma induced by the polymer coating may affect glial scar formation 3 weeks post surgery. Device 2, the larger probe (80 × 5 µm probe) with the small coating (100 × 100 µm coating) exhibited a higher astrocyte intensity compared to

device 1, the smaller probe (30 × 5 µm probe) with the same coating dimension (100 × 100 µm coating) but the intensity difference was not significant at this time point.

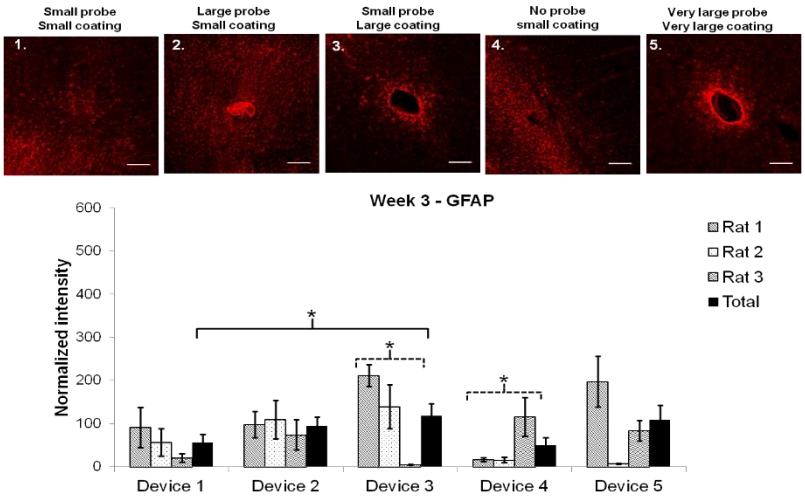

Figure 4-19: Normalized intensity of GFAP staining vs. different devices/rats 3 weeks post implantation Dashed line: statistical significance ($p<0.05$) between animals within an experimental group. Solid line: significance between devices across experimental groups ($p<0.05$). Scale bar : 200 µm.

By week 7 (Figure 4-20), device 1, the small probe (30 × 5 µm probe) with the small coating (100 × 100 µm coating) exhibited significantly less astrocyte density compared to device 2, the large probe (80 × 5 µm probe) with the small coating (100 × 100 µm coating), indicating the probe size began to have an effect on glial scar formation. There was no significant difference between device 1, the small probe (30 × 5 µm probe) with the small coating (100 × 100 µm coating) and device 4, the small coating (100 × 100 µm coating) without an encapsulated probe, suggesting the probe released from device 1 was small and flexible enough to attenuate astrocytes activation at this time point. However,

there was a significant difference between device 2, the large probe (80 × 5 µm probe) with the small coating (100 × 100 µm coating) and device 4, the pure small coating (100 × 100 µm coating). These results suggest that the 80 µm wide probe was too large and triggered the adjacent astrocytes to react to it, and therefore led to a more severe glial scar response than the smaller dimension probe (the 30 µm wide probe).

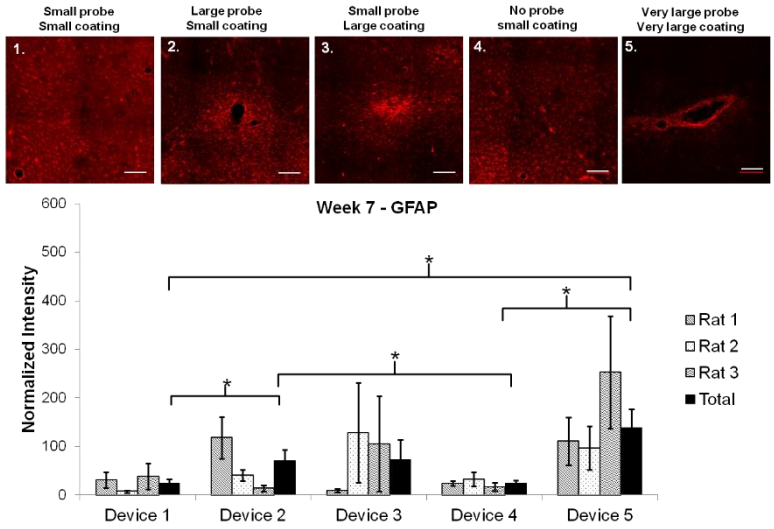

Figure 4-20: Normalized intensity of GFAP staining vs. different devices/rats 7 weeks post implantation. Dashed line: statistical significance ($p<0.05$) between animals within an experimental group. Solid line: significance between devices between experimental groups ($p<0.05$). Scale bar : 200 µm.

12 weeks after device implantation, the astrocyte glial scar response was distinct between all five devices (Figure 4-21). The astrocytes intensity was positively correlated to probe size for devices 1, 2 and 4, each encapsulated within the small coating (100 × 100 µm). Device 2, the large probe (80 × 5 µm probe) exhibited significantly higher astrocyte density around the implantation site compared to device 1, the small probe (30 × 5 µm

probe). At this time point, most of the devices in group 4, the pure polymer coating devices (100 × 100 μm coating) were healed and the wounds could not be identified around the implantation sites.

Within the small probe devices (Device 1 and 3), the astrocyte intensity was positively correlated to the polymer coating size. Device 3, the large coating probe (200 × 200 μm coating) exhibited significantly higher astrocyte density around the implantation site than the small coating probe (100 × 100 μm coating). Furthermore, the astrocyte intensity for device 3, the small probe (30 × 5 μm probe) with the large coating (200 × 200 μm coating) was higher than device 2, the large probe (80 × 5 μm probe) with the small coating (100 × 100 μm coating). This suggests that the polymer coating size may exhibit a more significant effect on astrocyte glial response than the overall probe size. Initial mechanical trauma was identified as a factor which may affect both the short and long term tissue response even though the polymer degrades after only couple hours following device implantation. It is thought, that the more severe initial trauma caused by implantation of devices with the larger coating may lead to a greater level of astrocyte activation, which leads to a more pronounced long term glial scar formation.

Device 3, the small probe (30 × 5 μm probe) with the large coating (200 × 200 μm coating) exhibited significantly higher astrocyte density around the implantation site than device 5, the very large probe (320 × 5 μm probe) with the very large coating (350 × 100 μm coating) at this time point. This may be due to the device geometry aspect ratio or cross

sectional area. The cross sectional geometry for Device 5 was wider but thinner and therefore may foster wound closure across the smaller dimension, which led to less severe astrocyte activation. Another explanation would be the larger cross-sectional area for device 3 (40,000 μm^2) compared to device 5 (35,000 μm^2), which led to a greater amount of tissue damage during insertion of device 3 and ultimately more severe astrocyte activation.

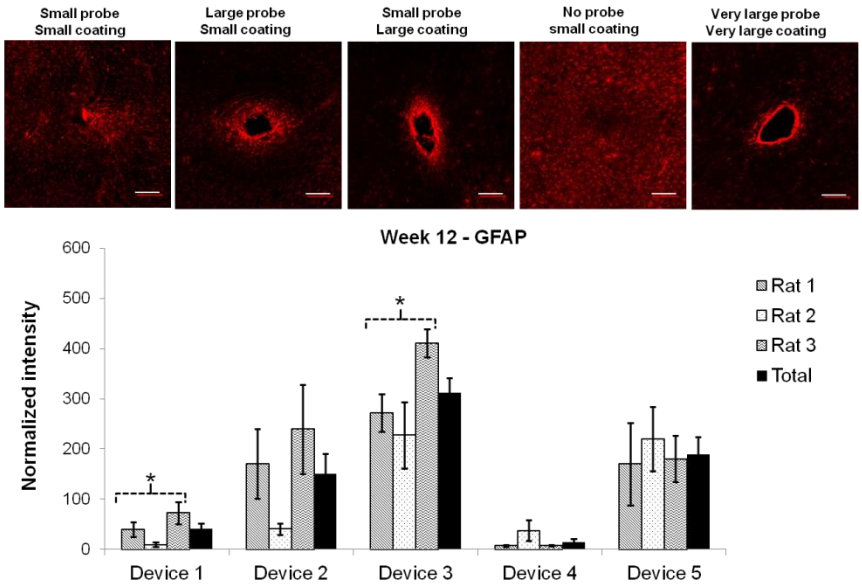

Figure 4-21: Normalized intensity of GFAP staining vs. different devices/rats 12 weeks post implantation. Dashed line: statistical significance ($p<0.05$) between animals within an experimental group. Solid line: significance between devices across experimental groups ($p<0.05$). Scale bar : 200 µm.

At 24 week following device implantation, the glial scar response stabilized and aligned with the results obtained from week 12 (Figure 4-22). Interestingly, the astrocyte intensity for device 1, the small probe (30 × 5 µm probe) with the small coating (100 × 100

µm coating) was not significantly different than device 4, the pure polymer shank (100 × 100 µm coating). This result suggests that over the 24 week period post device implantation, device 1 was small and flexible enough to avoid astrocyte recognition and activation and therefore the tissue response was comparable to that of device 4, the pure polymer shank.

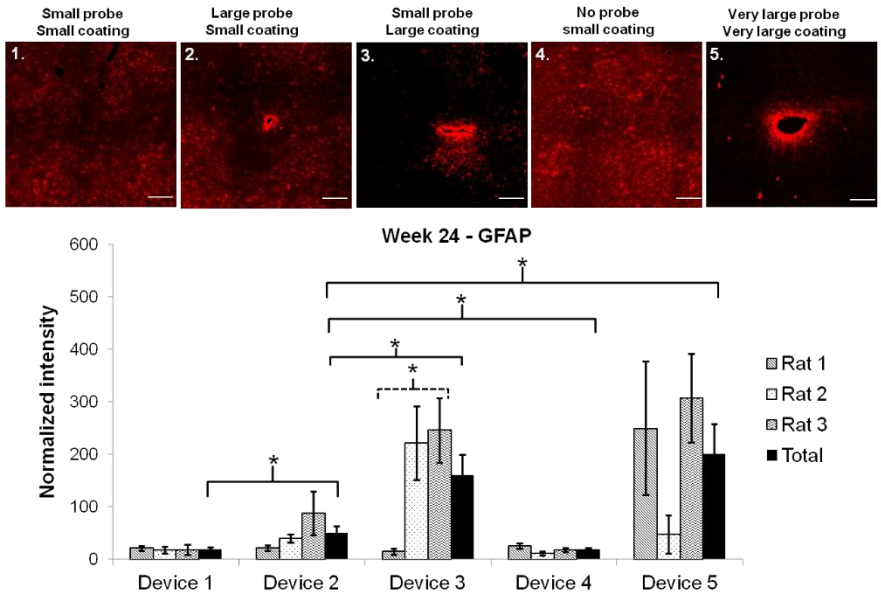

Figure 4-22: Normalized intensity of GFAP staining vs. different devices/rats 24 weeks post implantation. Dashed line: statistical significance ($p<0.05$) between animals within an experimental group. Solid line: significance between devices across experimental groups ($p<0.05$). Scale bar : 200 µm.

Figure 4-23 summarizes the astrocyte quantification by plotting the normalized intensity of GFAP staining with respect to different devices at the different time points. The astrocyte intensities increased significantly from 72 hours to 10 days for device 3 (30

× 5 μm probe, 200 × 200 μm coating) and device 5 (320 × 5 μm probe, 350 × 100 μm coating), which may be the result of the more serious tissue damage induced by the larger polymer coatings during implantation. Astrocyte intensity for device 4, the pure polymer coating (100 × 100 μm coating) reached a maximum at around 3 weeks post implantation and decreased at later time points, suggesting the wound healed and resolved itself during tissue recovery. In devices 1 (30 × 5 μm probe, 100 × 100 μm coating), 2 (80 × 5 μm probe, 100 × 100 μm coating) and 3 (30 × 5 μm probe, 200 × 200 μm coating), the astrocyte activation reached a maximum at week 12 but decreased and stabilized at week 24 with similar trends for devices 1, 2 and 3, although the degree of activation was more severe in devices 2 and 3. For device 5 (320 × 5 μm probe, 350 × 100 μm coating), the astrocyte activation increased consistently with the highest astrocyte intensity at 24 weeks compared to all other devices possibly due to the much larger probe dimension.

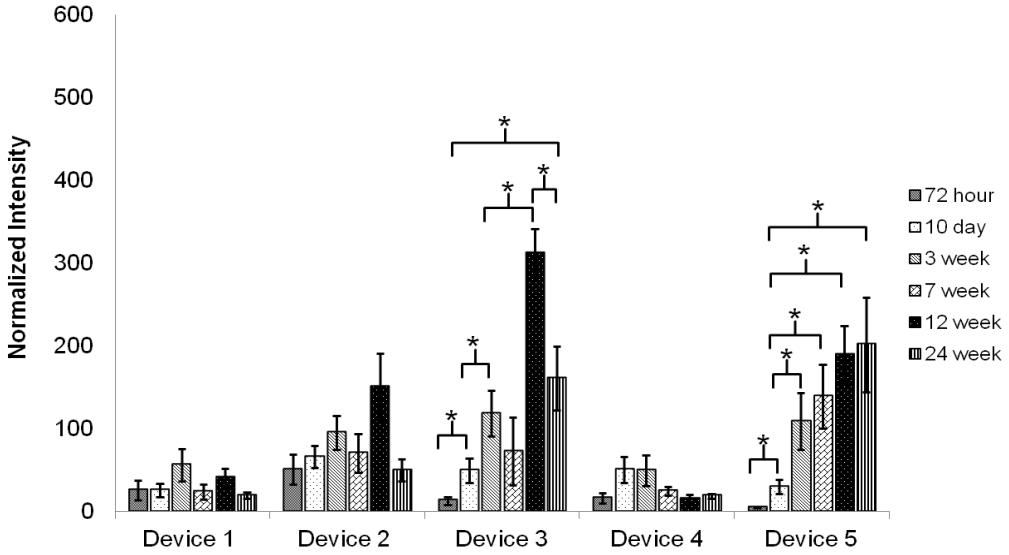

Figure 4-23: Normalized intensity of GFAP staining vs. different devices at different time points. Solid line: significance between different time points ($p<0.05$).

4.3.2.2 Glial cell response – Microglia

Microglia was quantified using Iba-1, which stained both resting and reactive states. The microglia has a highly branched morphology when in its resting state. Upon activation, they begin to proliferate and exhibit the amoeboid morphology. 72 hours after device implantation, reactive microglia can clearly been seen for all five devices (Figure 4-24). A compact layer of the microglia was observed for all the devices around the implantation sites, and there were no significant difference between all the devices in terms of microglia intensity at this time point.

Microglia is the main glial cell type residing around implantation sites during the acute tissue response. The mechanical insertion trauma activates microglia in order to phagocytose foreign matter and release inflammatory factors to aid in injury recovery. These results are consistent with the astrocyte staining at 72 hours post implantation, where a lower astrocyte density was observed around the implantation sites because the region was occupied by microglia for the wound healing response.

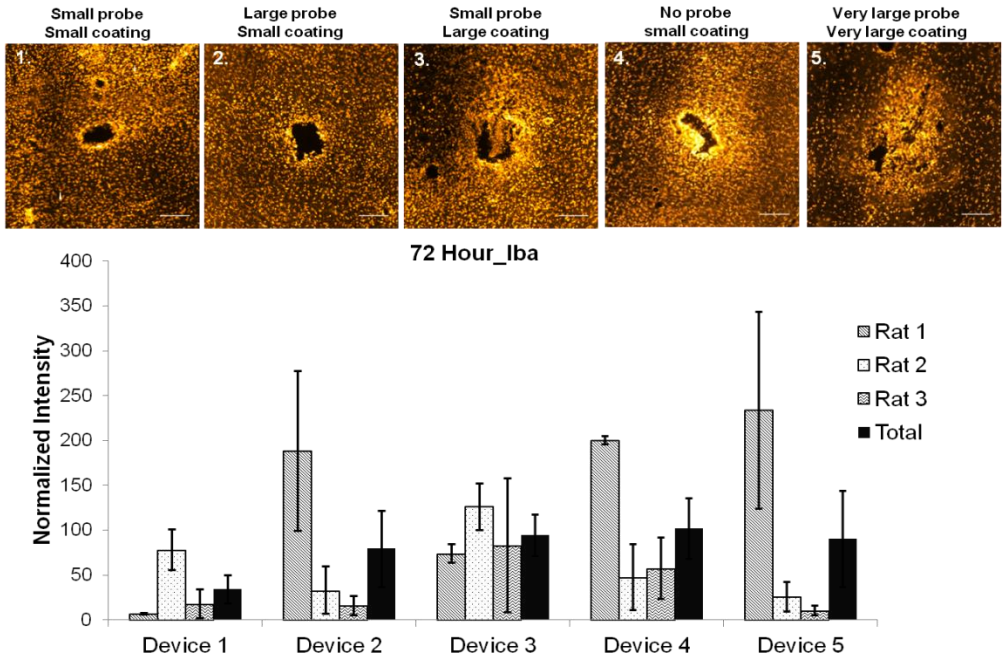

Figure 4-24: Normalized intensity of Iba-1 staining vs. different devices/rats 72 hours post implantation. Scale bar : 200 µm.

10 days following device implantation, the microglia behaviors began to stabilize (Figure 4-25). Amoeboid (Reactive) microglia could still be observed packed closely around the implantation sites, but the intensity decreased. Device 5 (320 × 5 µm probe, 350 × 100 µm coating), exhibited a higher microglia intensity compared to the other devices possibly due to the larger insertion wound that required a longer time to heal, but the difference was not significant. These results suggest that by this time point, the wound healing response triggered by the insertion mechanical trauma has declined considerably and the wound healing response had stabilized.

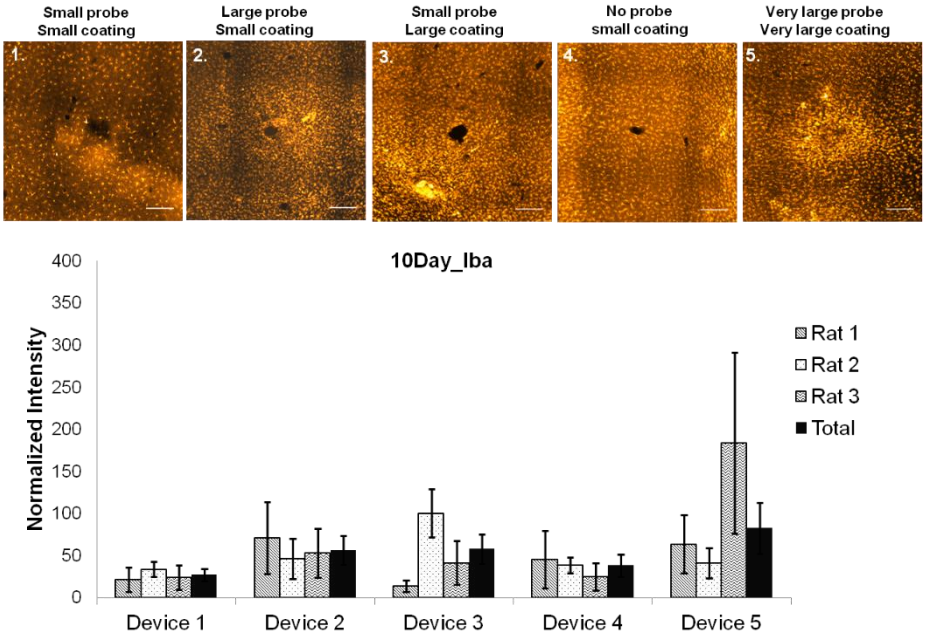

Figure 4-25: Normalized intensity of Iba-1 staining vs. different devices/rats 10 days post implantation. Scale bar : 200 µm.

3 weeks following device implantation, the microglia intensity increased for all the devices except device 4 (no probe, 100 × 100 µm coating) (Figure 4-26). Device 4 was the pure polymer shank without the probe encapsulation. These results suggest that in terms of microglia activation, the tissue reacts to both the parylene probes and the polymer coatings at this time point, but for just the polymer coating the wound has resolved. Microglia intensities were higher for device 2 (80 × 5 µm probe, 100 × 100 µm coating), and device 3 (30 × 5 µm probe, 200 × 200 µm coating), but the difference was not significant across all the devices. Microglia activation at this time point indicates a chronic foreign body response for neuro-inflammation and the time course observed aligns with other studies reported in the literature [6,45,125].

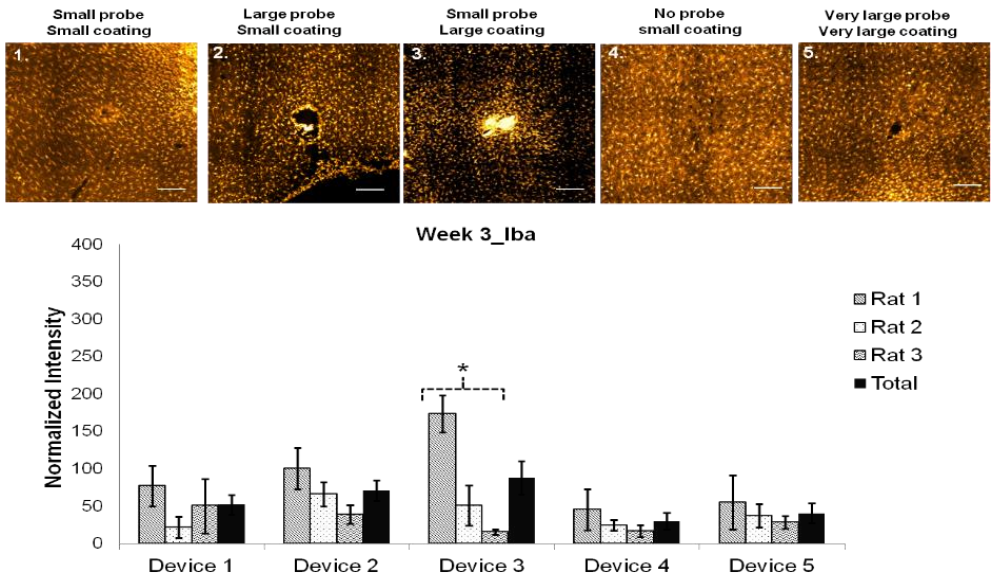

Figure 4-26: Normalized intensity of Iba-1 staining vs. different devices/rats 3 weeks post implantation. Scale bar : 200 µm. Dashed line: statistical significance ($p<0.05$) between

At week 7 (Figure 4-27), week 12 (Figure 4-28) and week 24 (Figure 4-29) post device implantation, microglia intensity decreased and stabilized. There was only a small level of activated microglia observed for both week 7 and week 12 across all the devices. At week 24, the microglia intensity for device 3 (30 × 5 µm probe, 200 × 200 µm coating), and device 5 (320 × 5 µm probe, 350 × 100 µm coating), were higher than the rest of the devices consistent with the observed astrocyte response. The microglia intensity was positively correlated to the astrocyte intensity at week 24. This result was expected because even though the glial scar consists of mainly astrocytes, activated microglia have also been observed in many other studies.

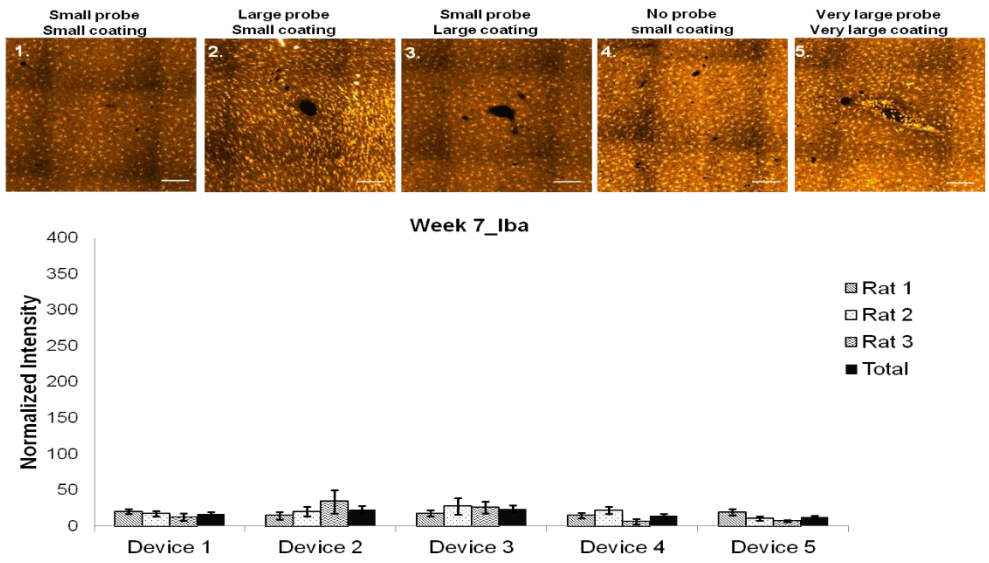

Figure 4-27: Normalized intensity of Iba-1 staining vs. different devices/rats 7 weeks post implantation. Scale bar : 200 µm. Dashed line: statistical significance ($p<0.05$) between

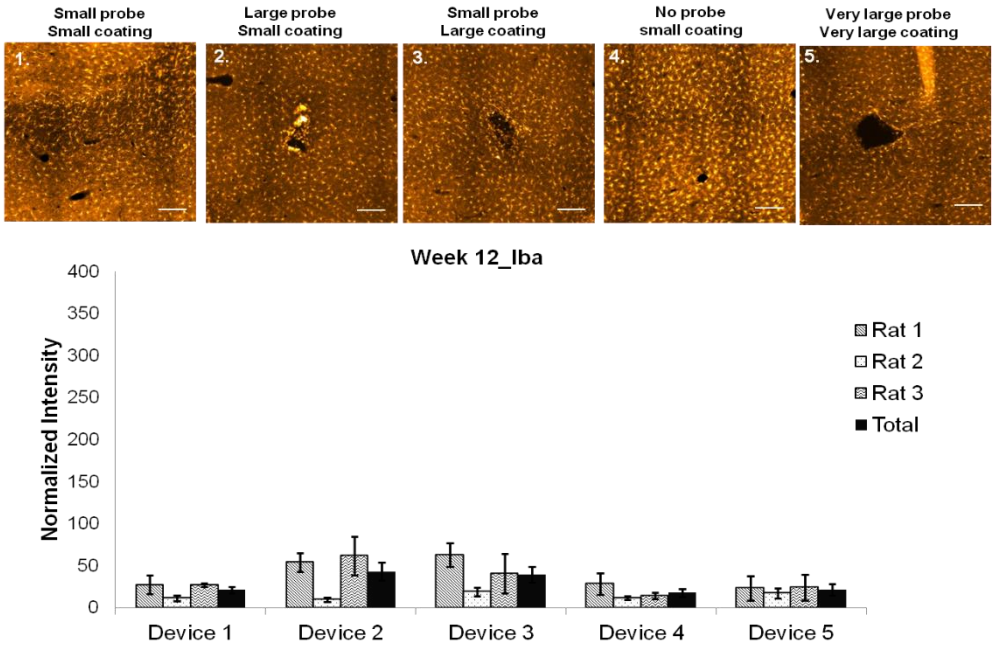

Figure 4-28: Normalized intensity of Iba-1 staining vs. different devices/rats 12 weeks post implantation. Scale bar : 200 µm.

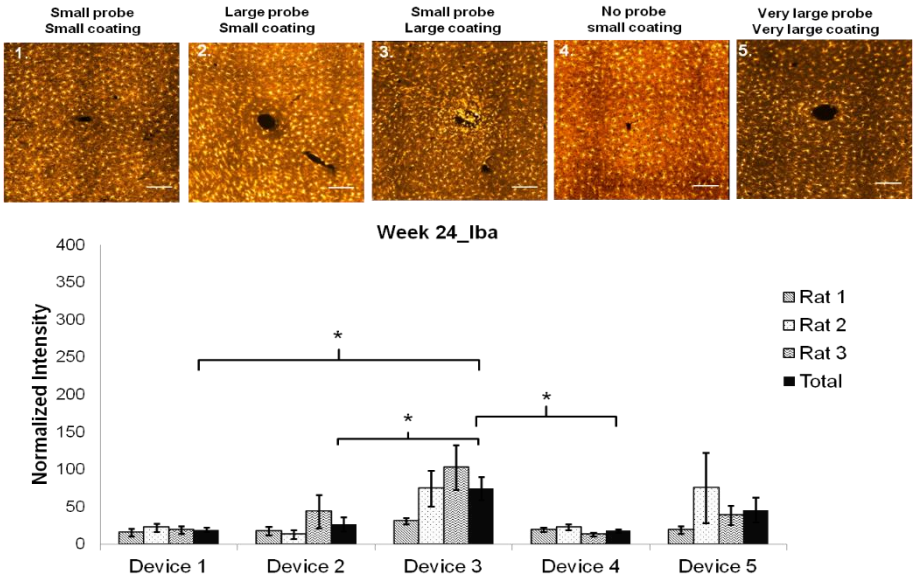

Figure 4-29: Normalized intensity of Iba-1 staining vs. different devices/rats 24 weeks post implantation. Solid line: significance between devices ($p<0.05$). Scale bar : 200 µm.

Figure 4-30 displays the normalized intensity of Iba-1 staining with respect to different devices at different time points. The microglia intensities were the highest across all the devices 72 hour post implantation due to the wound healing response. The acute response subsided 10 days post surgery, indicating tissue recovery from the initial mechanical insertion trauma. Devices 1 (30 × 5 µm probe, 100 × 100 µm coating), 2 (80 × 5 µm probe, 100 × 100 µm coating), and 3 (30 × 5 µm probe, 200 × 200 µm coating), experienced a microglia intensity increase at week 3. This might result from neuro-inflammation triggered by the parylene probes left within the tissue. The microglia tissue response reached stability around week 7. By week 12 and week 24, the microglia intensity was highly correlated to the astrocyte intensity. Devices 3 (30 × 5 µm probe, 200 × 200

μm coating), and 5 (320 × 5 μm probe, 250 × 100 μm coating), exhibited a thicker glial scar and larger number of activated microglia were observed. This was expected as activated microglia and reactive astrocytes were both the main components of the glial scar.

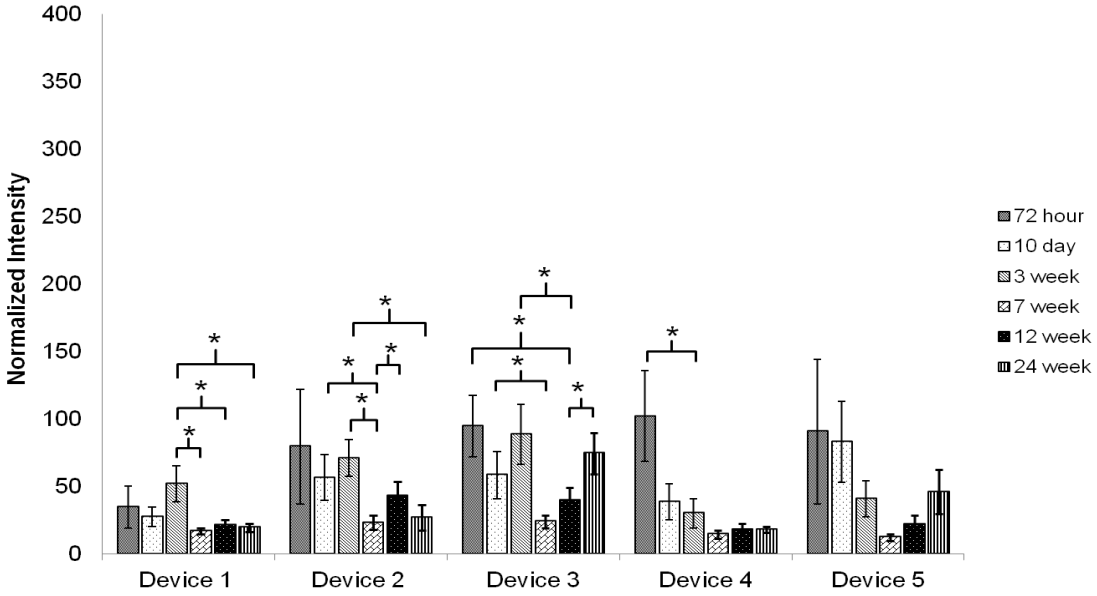

Figure 4-30: Normalized intensity of Iba-1 staining vs. different devices at different time points. Solid line: significance between different time points ($p<0.05$).

Figure 4-31 plots a ratio of the astrocyte to microglia intensity at each of the different time points for the different devices. This shows the relative contribution of each cell type over the time course of the study. As expected, it was observed that there was a higher percentage of microglia at the early times following implantation (ratio < 1) for all devices while after 10 days, astrocytes started to accumulate around the probes and form the glial scar layer around the implantation sites (ratio > 1). Microglia is the dominant cell type for the acute wound healing response and astrocytes are the dominant cell type for

chronic glial scar formation. These results imply that sometime between 10 days and 3 weeks post implantation the acute tissue response declined and the chronic tissue response becomes apparent. These dynamics match other studies reported in the literature[36,45,46]. It also shows that by 24 weeks the microglia and astrocyte density in device 1 (30 × 5 μm probe, 100 × 100 μm coating) and device 4 (no probe, 100 × 100 μm coating) are equal and the wound appears to be healed from the quantification of each cell type. Furthermore, it can be observed that it took longer time for the larger polymer coating devices (device 3 (30 × 5 μm probe, 200 × 200 μm coating) and 5 (320 × 5 μm probe, 350 × 100 μm coating)) to transition from having a higher density of microglia to more astrocytes around the implantation site. This may be the result of a more severe injury caused by the larger polymer coating during implantation which prolonged the acute tissue response. The relationship between astrocytes and microglia for each individual device at different time points is reported in appendix A.5.

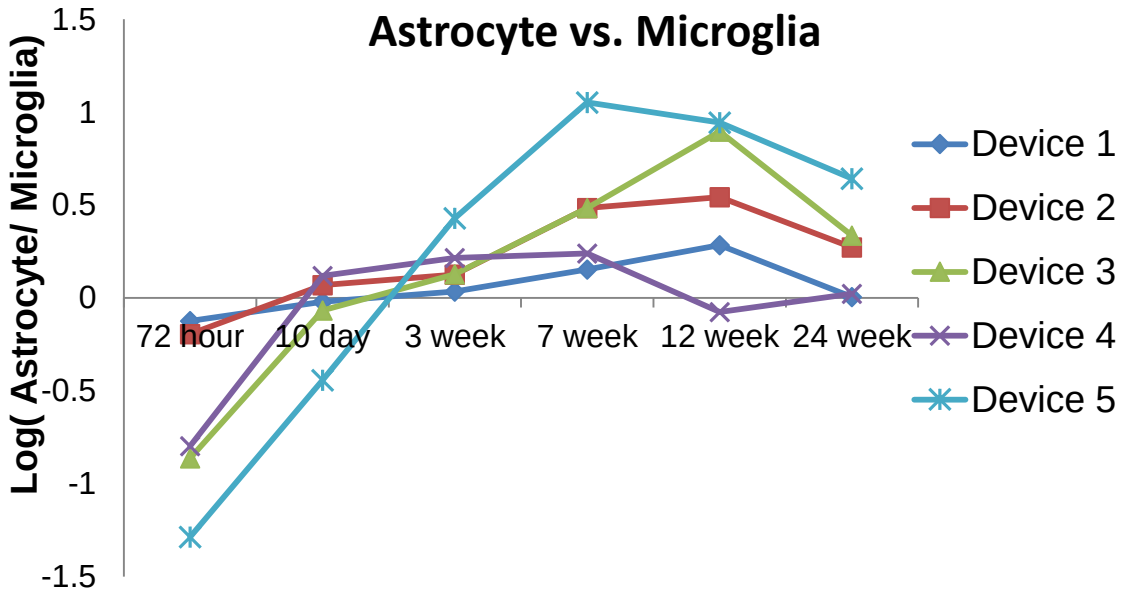

Figure 4-31: The relationship between microglia and astrocytes at different time points for different devices.

4.3.2.3 Discussion

Five devices with varying polymer and probe sizes were evaluated on glial scar formation at different time points ranging from short (72 hours) to long term (24 weeks) post implantation. The fast-degrading polymer used in this work degraded and was resorbed within a couple of hours following device implantation. Several device design parameters were identified to have possible effects on the tissue response progression.

Previously in our group, Lewitus et al. showed that the tissue response induced by the fast degrading polymer coated microwire and the uncoated microwire did not show any qualitative differences on tissue response[126], suggesting the polymer coating had minimal

or no adverse effects on the tissue response up to 4 weeks post implantation. In this study, the tissue response induced by a small fast degrading polymer shank (Device 4, no probe, 100 μm wide × 100 μm coating) were evaluated. It is showed that the small fast degrading polymer shank exhibited a minimal glial scar response and the wounds were mostly closed at 7, 12 and 24 weeks post implantation. The results further confirmed the polymer's long term biocompatibility within the brain tissue at a much extended time course. However, the size of the polymer coating is identified to affect tissue response and discussed in the next paragraph.

The larger polymer coating (Device 3, 30 × 5 μm probe, 200 × 200 μm coating) exhibited a more serious glial scar response than the same sized probe encapsulated within the smaller polymer coating (Device 1, 30 × 5 μm probe, 100 × 100 μm coating) even after 24 weeks post device implantation. These results were somewhat unexpected and suggest that the size of the polymer coating can affect the long term glial scar response even though each coating was only few hundred microns and was rapidly degraded. It is hypothesized that the initial trauma may adversely affect the longer term tissue response. If the initial mechanical trauma is too severe, the wound might not be able to heal and close, which could lead to the observed long term tissue response. The initial mechanical trauma may also cause greater activation of surrounding astrocytes so they are more sensitive to the presence of the probe. A similar phenomenon was observed by Kozai et al. using carboxymethyl cellulose (CMC) as the insertion shuttle[127]. The wound sites for the majority of the large CMC shuttles never closed within 12 weeks after implantation. It is therefore

concluded that the size of the polymer coating matters in both the short and long term tissue response.

The initial mechanical insertion trauma could also explain variability in response between animals even when implanting the same probes. If a probe happens to shear a larger blood vessel during insertion, it may lead to a more severe tissue reaction even for a smaller probe or implant size. However, the larger sized coatings are expected to be more likely to disrupt more blood vessels during insertion.

At week 12, the glial scar response was significantly more severe for device 3 (30 × 5 μm probe, 200 × 200 μm coating) than device 5 (320 × 5 μm probe, 350 × 100 μm coating). Device 5 was designed and chose as a control reference to match the size of many of the flexible probe dimensions reported in the literature. It was surprising to observe a more severe tissue response for device 3 than device 5 at later time point such as 12 weeks post device implantation. The results first agreed with the finding that the larger sized polymer coating affected both long and short term tissue response even though the polymer degraded fast. Second, cross sectional area and device geometry aspect ratio may be responsible for device 3 inducing a more severe tissue response. Device 3 had a cross sectional area of 40,000 μm^2 and a more square geometry whereas device 5 had a cross sectional area of 35,000 μm^2 and a 3.5:1 aspect ratio producing a more "flat" geometry. The smaller cross sectional area may produce less tissue damage during implantation and the flatter geometry might be beneficial for faster wound healing and closure across the

wound's 100 μm width. However, device 5 induced a more severe glial scar response than device 3 24 weeks following device implantation. Even though the difference was not significant, it implied the much larger, wider probe for device 5 may begin to play a role in the longer term tissue response. It is difficult to draw a clear conclusion as to whether device aspect ratio is a major contributing factor in affecting tissue response with the results obtained from the study. It is also not clear whether the tissue response was the effect of only the polymer coating or the probe or both. Future research can evaluate devices with the same cross sectional area but different geometry aspect ratio polymer coatings with the same sized probes to further investigate the role the coating dimensions, probe dimensions and shape each play in tissue response.

The probe size also played an important role in long term glial scar response. Device 2 (80 μm × 5 μm probe, 100 μm × 100 μm coating) induced significantly more glial scar response than device 1 (30 μm × 5 μm probe, 100 μm × 100 μm coating) 7 weeks following device implantation, with a similar trend observed for later time points. The trend was not observed at an earlier stage possibly because the brain tissue was affected by the mechanical insertion trauma from the degrading polymer shuttle, and so the effects of probe size on the tissue were not apparent until later. Both probes were made from the same flexible material, which helps minimize mechanical mismatch between the device and the tissue. However, the large sized probe (80 μm wide × 5 μm thick) should be ~ 2.67 times stiffer which may be enough to produce an appreciable interfacial strain caused by device

micromotion, leading to a more severe tissue response compared to the small sized probe (30 μm wide × 5 μm thick).

The tissue response induced by the 30 μm wide × 5 μm thick probe with the 100 μm wide × 100 μm thick polymer coating (Device 1) was similar with the pure small polymer shank 24 weeks after device implantation. These results suggest that the 30 μm wide × 5 μm thick probe (Device 1) was not recognized by the glial cells due to its small size and therefore would be a more ideal probe candidate. However, a wider probe is more desirable to maximize the number of electrodes which can be fabricated on the probe for higher signal recording efficiency. Future research can investigate probe sizes between 30-80 μm wide to identify the optimal size that can incorporate multiple electrodes without inducing a severe glial scar response.

10 probes were implanted into one single animal for each implant performed during this study. During the histological analysis, the possible implantation sites were identified by applying a grid that was corresponded to the surgical holder dimensions. However, sometimes there were difficulties in identifying exact location of a possible implantation site. First, the probes may not insert vertically but with a slight angle into the brain because they were fixed on the surgical holder and inserted into the brain manually. Second, when the brain was sliced for histological staining, it was difficult to ensure complete horizontal positioning of the brain prior to slicing. The human error introduced during the fixation, implantation and tissue slicing might cause the implantation site to shift and therefore

introduced difficulties in implantation site identification. Furthermore, 10 probes were designed and fixed at least 2 mm apart from each other to minimize tissue response interference. The implantation site misplacement sometimes caused very close sites, which may affect experimental outcomes. For future study, fewer devices can be implanted into one single animal in order to minimize interference between devices. It will also be easier to identify implantation sites if fewer devices were implanted regardless of human error in processing the samples. Furthermore, it will be beneficial to fluorescently label the polymer coating in order to aid in implantation site identification. Fluorescently labeled polymer can also help monitor and investigate the polymer degradation profile within the brain tissue, which can also be an important factor in tissue response progression.

Two craniotomy holes were drilled in order to implant 10 probes simultaneously into the rat brain. However, the brain tissue could be damaged from the invasive operation and a defect region was occasionally observed (Figure 4-32). The defect region caused loss of implantation sites and tissue response interferences, which might affect experimental outcomes. For future experiments, large craniotomy holes should be prevented by implanting fewer devices into the rat brain or making the smaller craniotomy holes in order to minimize tissue damage.

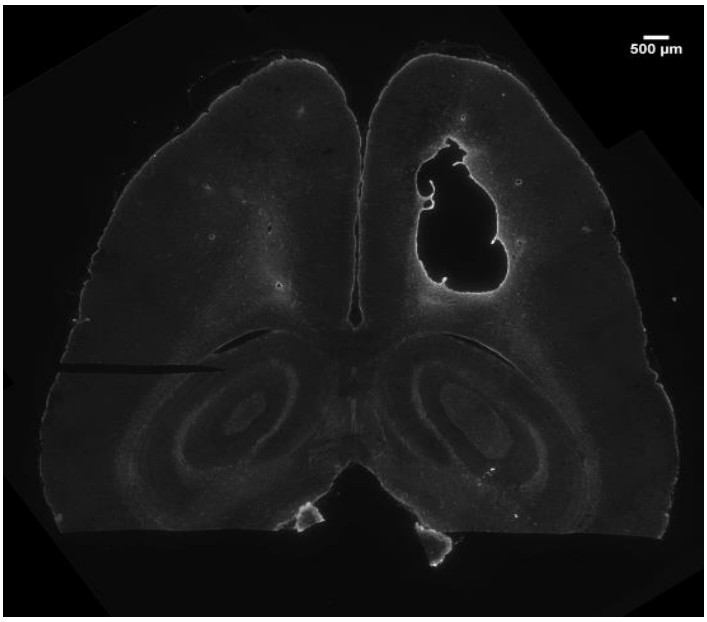

Figure 4-32: The brain defect caused by large craniotomy holes for device implantation.

CHAPTER 5 DEVICE FUNCTIONALIZATION

5.1 Overview

Non-functional polymer coated probes were developed and device design parameters were investigated using in vivo animal models. In this chapter, a functional probe, containing recording electrodes was developed and is discussed. Parylene was selected as the base layer support material and electrodes were patterned onto the parylene support via metallization. The electrodes were then passivated with a second layer of parylene and recording via opened in the passivation layer. The functional probe was examined physically using the bright field and SEM microscopy to ensure device integrity. The probe functionality was then evaluated through a series of different electrical characterizations. In phase 1, the probe was verified to be operational through impedance characterization (electrode current in solutions of varying conductivity, I-V curve, frequency sweeping testing, fixed volume current verification and evaporation testing). These tests were conducted to ensure probe functionality as well as to understand electrode characteristics such as sensitivity and durability. During phase 2, the effects of polymer degradation on the probe impedance was characterized. The functional probe was coated with the ultrafast degrading polymer using the methods described in chapter 3.2.3. The impedance of the functional probe was monitored within a physiological saline solution before and after polymer degradation to verify electrode integrity during polymer coating and degradation procedures. Finally, integration between the electrode and outer electrical

instrumentation was developed to integrate the probe to a commercially available data acquisition system to be ready for in vivo signal recording.

5.2 Functionalized polymer coated parylene probe fabrication

5.2.1 Electrical considerations for the probe design

As mentioned in the previous chapter (Chapter 4.2.1), most conventional microelectrodes have impedances varying from 50 kΩ ~1 MΩ at 1 kHz[128]. A 1 kHz acquisition frequency is widely used for impedance measurements as it is the fundamental action potential frequency and therefore exhibits physiological relevance[129–131]. Previous studies have also shown that a recording area of 400 to 600 μm^2 is typically used to obtain an electrode with an impedance of approximately 1 MΩ[77,129,132]. In order to maintain recording feasibility while minimizing the probe size, I aimed to design the electrodes with 20 µm × 20 µm or 30 µm × 30 µm square recording areas along the small probe shank. Besides the recording windows, connecting traces were designed to transmit the electrical signals to a larger connection pad made to integrate with an external electrical data acquisition system. Platinum was chose as the electrode material due to its inertness (resistance to corrosion), biocompatibility and high conductive properties[133].

5.2.2 Functional probe fabrication procedure

The functional probe was fabricated by patterning the electrodes, connecting traces and the connection pad between two thin layers of parylene films (Figure 5-1). The fabrication can be divided into several steps described as follows:

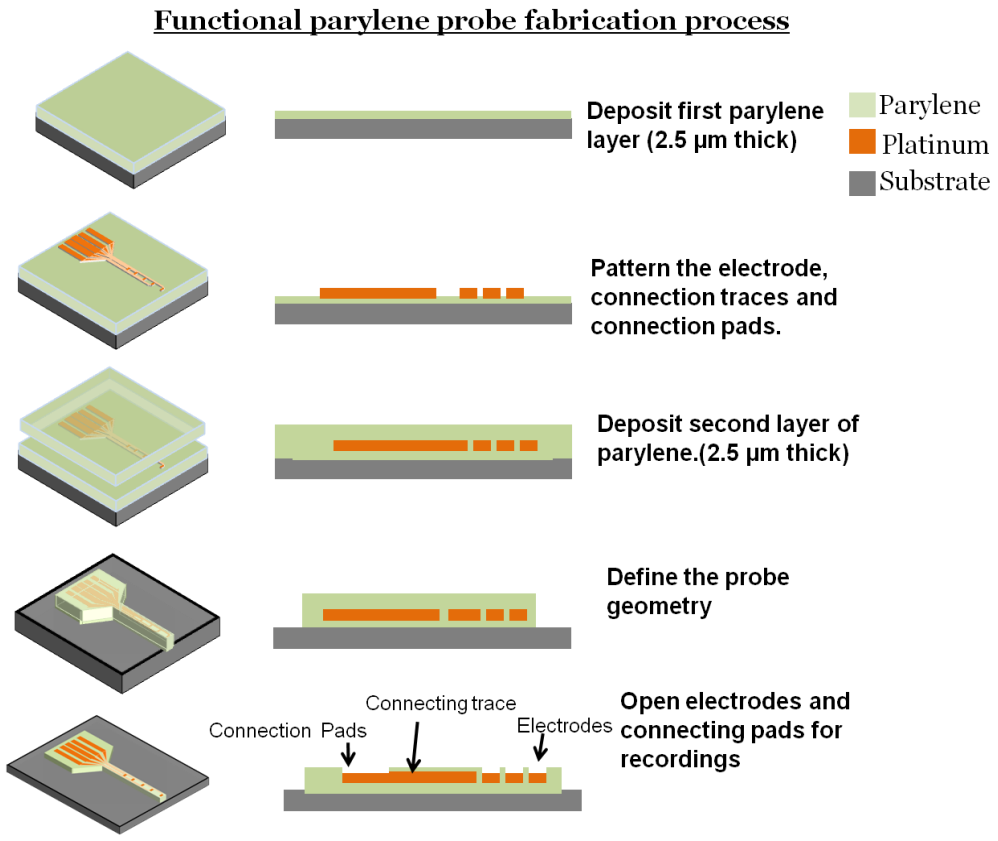

Figure 5-1: Fabrication process of the parylene functional microelectrode. A thin layer of parylene film (5 µm) was deposited onto a substrate. Ti/Pt electrodes were defined using the lift-off method. Another layer of parylene film (2.5 µm) was deposited to insulate the electrical traces. An aluminum mask defined the probe geometry and patterned electrode openings/connecting pad. Finally, oxygen plasma was used to etch the un-masked parylene and the aluminum mask was dissolved using an aluminum etchant.

- Substrate preparation

A substrate (glass slides or silicon wafers) was prepared and cleaned using acetone, isopropanol and water. An aluminum metal layer was deposited onto the substrate via physical vapor deposition system (PRO Line PVD75, Kurt J. Lesker Company, Hudson Valley, PA, USA) as a sacrificial layer to lift off the completed probe from the substrate.

- Base parylene layer deposition

Following the aluminum metal layer deposition, a thin layer (~5 μm) of parylene was deposited via a SCS Labcoater 2 Parylene Deposition System (Special Coating System, Indianapolis, IN, USA). The backside of the substrate was taped for easy removal of excess parylene film following deposition. The adhesion between the parylene film and electrode material (platinum) is a mechanical process instead of a chemical bond and is therefore weak which can lead to electrode delamination from the parylene substrate. In order to enhance the adhesion strength between the metal layer and the parylene film, the substrate was exposed to an oxygen plasma (PX-500 Plasma treating system, Nordson Corporation, Westlake , OH, USA) (600 mTorr, 100W) for 1 minute. The oxygen plasma etching roughens the parylene surface which can also enhance the metal attachment onto the substrate.

- Electrode patterning

Photolithgraphy was performed to pattern the electrode geometry. A thin layer of positive photoresist (Shipley S1818, Microchem Corp, Cambridge, MA, USA) was spin-coated onto the supporting parylene-coated substrate (3000 rpm) to the desired thickness (3 μm). The substrate was then soft baked at 120 °C for 4 minutes to evaporate the solvent. The electrode geometry was defined by LWUV exposure at 130 mJ/cm^2 (EVG®620 Automated Mask Alignment System, Tempe, AZ, USA). The exposed Shipley was dissolved using photoresist developer (MF-319, Microchem Inc., Cambridge, MA, USA). The whole device was then baked at 120 °C (hard baking) to enhance the bonding between the photoresist and the substrate. The photoresist served as a mask layer for probe feature definition.

- Electrode fabrication via metal sputtering

In order to further increase the bonding strength between the electrode and the parylene film, the slide was treated with an adhesion promoter, A-174 silane (Gamma-Methacryloxypropyltrimethoxysilane, CAS# 2530-85-0, Special Coating System, Indianapolis, IN, USA), by soaking the sample within a solution with equal parts of isopropanol and DI water with 0.5% v/v of the A-174 silane added. The silane molecules form chemical bonds on the surface of the parylene film to enhance the bonding strength between the electrode metal and the parylene film. The slides were placed in a metal sputtering system (Kurt Lesker PVD 75, Kurt J. Lesker Company, Pittsburgh, PA, USA) to deposit titanium and platinum metal layers. The titanium metal

layer was sputtered first for 9 minutes at 200W to a thickness of ~2000 Å. The titanium serves as an adhesion layer for better attachments of the platinum metal layer. The platinum metal layer was then sputtered for 9 minutes at 200W to a thickness of ~2000 Å as the conductive layer to record signals from neurons. Finally, the metal-coated photoresist (Shipley S1818) was removed by dissolution of the photoresist within an acetone bath using a sonicator. The process removes both the photoresist layer and the metal on top of the photoresist which is not in contact to the unmasked areas of the substrate in a 'lift off' procedure.

- Parylene insulation layer deposition

  Following metal deposition onto the substrate, another parylene layer was deposited. The purpose of the second parylene layer is to insulate the connecting traces and part of the connection pad from making electrical contact to the ambient environment, which might interfere with signal acquisition. The thickness of the parylene layer was optimized (first layer: 5 µm; second layer: 2.5 µm) to prevent water permeation from damaging the metal traces.

- Probe geometry , recording windows and connecting pad patterning

  The probe geometry, recording windows and the connection pad were also defined though a lift-off process. A thin positive photoresist (Shipley S1818, Microchem Corp, Cambridge, MA, USA) was spin-coated on the parylene-coated substrate (3000 rpm) to the desired thickness (3 µm). The substrate was then soft baked

at 120 °C for 4 minutes to evaporate the solvent. Figure 5-2 displays the transparency mask used to pattern the desired features. The white regions of the mask were transparent and therefore the photoresist could be cross-linked with LWUV light. The exposed photoresist were then dissolved by the photoresist developer (MF-319, Microchem Corp, Cambridge, MA, USA). The slides were placed in a metal sputtering system (Kurt Lesker PVD 75, Kurt J. Lesker Company, Pittsburgh, PA, USA) to deposit an aluminum metal layer. Aluminum was sputtered for 15 minutes at 200W to a thickness of ~5000 Å to ensure an uniform metal coating. Finally, the photoresist (Shipley S1818) was removed by dissolution of the substrate within acetone bath using a sonicator. After the process, an aluminum metal layer defining the probe geometry, recording windows and connecting pad was patterned.

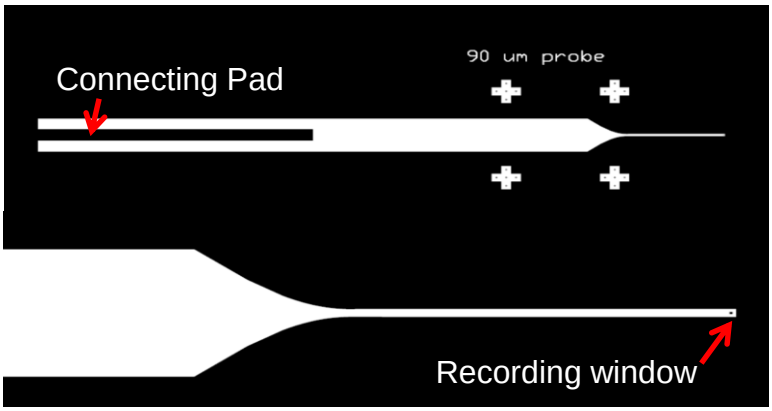

Figure 5-2: Schematic of the mask layer defining (Top) the recording windows and the connection pad, and (Bottom) the probe geometry. The cross marks are alignment mark for aligning the probe with the electrode. Device dimension: The probe: 90 µm wide and 4 mm long. The recording window: 30 µm × 30 µm square. The connecting pad: 1 cm long and 1.5 mm wide.

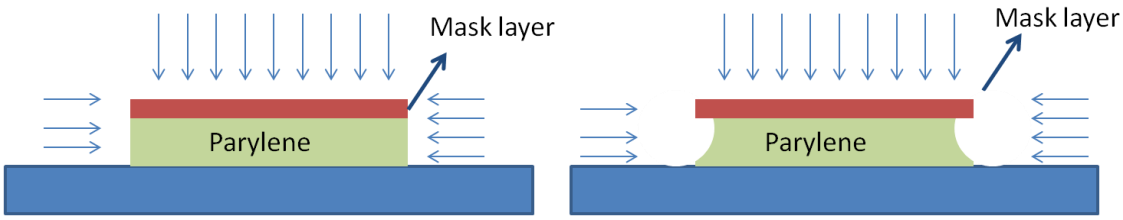

Figure 5-3: Oxygen plasma etching of a parylene layer. It is an isotropic process that removes material at an equal rate in all directions.

- Parylene etching and the device lift off

  The substrate was then etched using an oxygen plasma (250W for 30 minutes) to remove the unprotected parylene and patterned the probe shape. The protocol etched through the total 7.5 µm thickness of the two parylene layers. The aluminum metal layer served as a masking layer to protect regions or features that were lithographically defined during the previous step. The oxygen plasma etching is an isotropic process, in that the etch rate is expected to be the same in the vertical direction as it is in the horizontal direction. The aluminum mask served as a vertical stop for the etching but becomes undercut in an isotropic etch in the horizontal direction (Figure 5-3). In order to investigate the horizontal etching rate, a SEM image was taken after the device was etched using an oxygen plasma (Figure 5-4). The parylene layer was found to be etched 2 µm from the edge of the mask layer. Therefore, the features defined at previous steps were patterned to be ~5 µm (2.5 µm each side) wider from the desired probe geometry and ~5 µm narrower from the desired dimensions for recording windows and

connecting pad to compensate the horizontal etching during the oxygen plasma treatment.

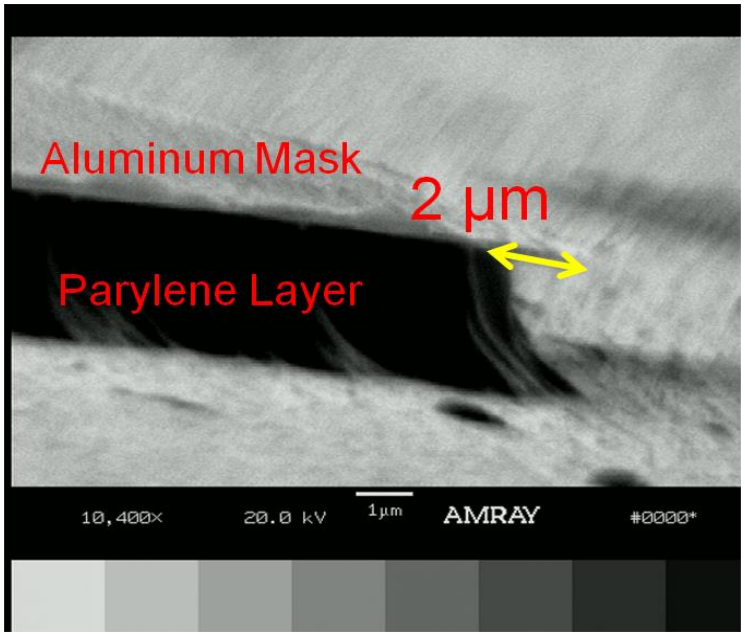

Figure 5-4: SEM image of a parylene probe masked by an aluminum layer post oxgygen plasma etching treatment. The vertical etch rate is ~7.5 µm and horizontal etch rate is ~2 µm at 250W for 30 minutes.

The etching process not only defined the final probe geometry but also exposed the recording windows to make contact with adjacent cells once the probe is implanted for signal acquisition and the connection pad for the external electrical instrumentation incorporation. Finally, a chemical aluminum etchant was used to dissolve the aluminum mask layer as well as the underlying sacrificial aluminum layer to lift the probe from the substrate.

5.3 Functionalized polymer coated parylene probe characterization

5.3.1 Physical examination of the functional parylene probe

The functional probe was imaged to evaluate its integrity. Figure 5-5 displays bright field microscopy images of the functional probe. The parylene layer was transparent and therefore only the outline of the probe geometry can be seen due to the edge contrast during imaging. The black features defined the electrical traces patterned on the probe. A single 30 × 30 μm electrode can be seen at the tip of the probe. The electrode recording area was opened to be used to record signals from surrounding neurons following implantation. Connecting traces delivered electrical signals recorded from the recording window. The large and flexible connection pad could be used as a cable to connect to an external data acquisition system. All of the electrical traces must be continuous without breakage to ensure recording capability. The single-electrode probe was fabricated for preliminary evaluation to ensure fabrication feasibility and device integrity. After the fabrication procedure was confirmed, it can be expanded to increase the number of electrodes patterned along the probe shank. Multiple-electrodes probes are desirable to enable simultaneous recording within regions of interest for better recording efficiency. However, each electrode requires its own connecting trace and connection pad and there is therefore a limit on number of electrodes that can be patterned on a single probe while keeping the probe dimensions as small as possible (Figure 5-6). Producing more compact and a larger number of electrodes increases the fabrication difficulty for alignment between the electrical traces and the probe shank. A slight lithographic misalignment can lead to

electrodes not perfectly patterned on the probe shank, while a rotational misalignment can lead to the traces not being supported along the probe length. Based on the results from the animal study, the 80 µm wide probe, which can contain two or three electrodes, induced significantly more severe glial scar response compared to the 30 µm wide probe. However, the 30 µm probe can only contain one electrode that will limit the recording efficiency. Therefore, future studies may be needed to evaluate probes that are wider than 30 µm but narrower than 80 µm, to see if they are capable of containing at least two electrodes while attenuating the long term glial scar response.

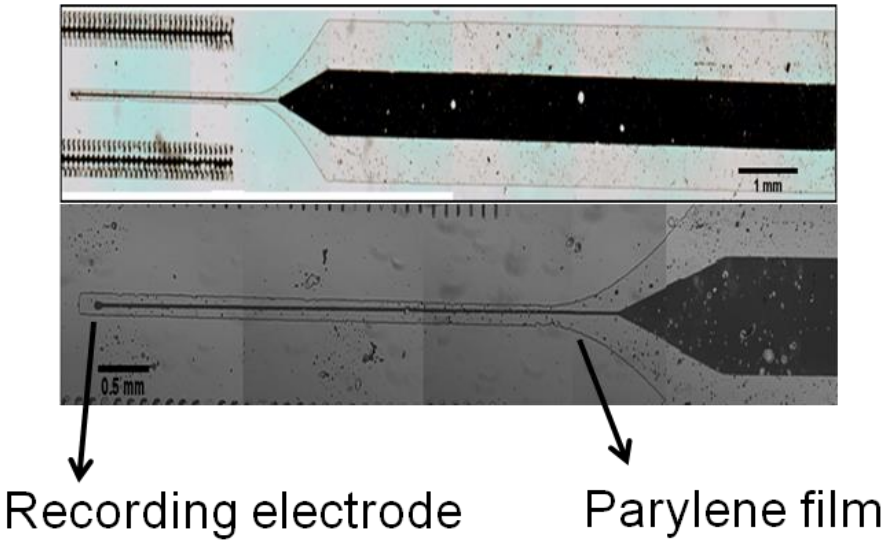

Figure 5-5: Bright field microscopy images of the funationalized probe with connecting traces, a recording window and the connecting pad for outer electrical instrumentation incorporation. Device dimension : The probe: 90 µm wide, 5 µm thick and 4 mm long. The recording window: 30 µm x 30 µm square. The connecting pad: 1 cm long and 1.5 mm wide.

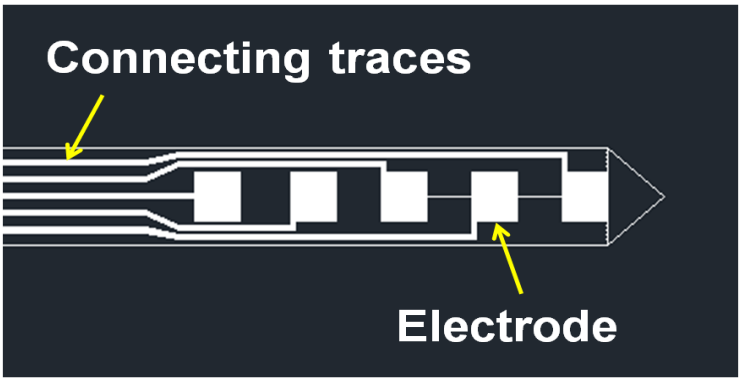

Figure 5-6: A represensative mask design with multiple electrodes patterned along a single shank of the probe. Each electrode requires individual trace connection for signal delivery to the outer data acquisition system.

Figure 5-7 displays a SEM image of the polymer coated functional probe. The polymer coating was uniform without mechanical or material disruption and therefore confirmed successful polymer coating recipe adapted from the non-functional to the functional probe.

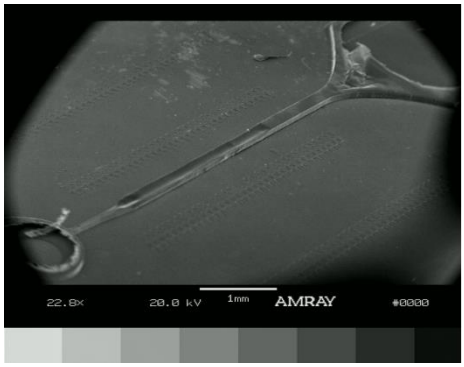

Figure 5-7: The SEM micrograph of a polymer coated functional probe. Device dimension: The probe: 90 µm wide, 5 µm thick and 3.5 mm long. The polymer coating: 100 µm wide, 100 µm thick and 4 mm long.

5.3.2 Preliminary packaging design for the functional probe

One of the design considerations which needed to be thought through was connecting the flexible exposed connecting pad of the probe to any external electrical data acquisition system (Figure 5-8). A zero-insertion-force (ZIF) connector (FH26-33S-0.3SHW(05); Hirose Electric USA Inc., Simi Valley , CA ,USA) was used to interface with the external instrumentation system. The exposed connection pad was thickened using a polyimide film placed under the connecting end of the probe in order to match the required contact thickness for the ZIF interface. The thickened region can then be inserted into the locking area of the ZIF connector. The connecting pad was aligned with the desired electrical pin and the cable lock (black lever) was flipped to fix the probe in place. The other side of the ZIF connector consists of arrays of standard electrical pins that can be connected to a printed circuit board for further interfacing with other equipment.

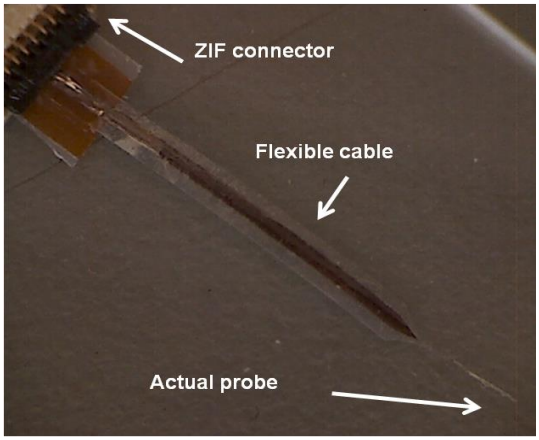

Figure 5-8: Photograph of a packaged functional probe. The zero-insertion-force (ZIF) connector was used to incorporate parylene probe with electrcal pins for interfacing.

5.4 In vitro electrical characterization for the functionalized microprobes

5.4.1 Experimental methods

After finalizing the fabrication process for the functionalized probe, the device was then electrically evaluated to ensure functionality. The performance of the functional probe was verified using a signal acquisition system from Zurich instruments (HF2LI Lock-in Amplifier, Zurich Instruments, Zurich, Switzerland). The signal acquisition system has several advantages: 1) the measurement bandwidth is from 80 μHz to 200 kHz and therefore provides broad spectrum for operation; 2) the input sensitivity is minimal at ~1nV which is highly sensitive to the testing environment for detecting signals of interest as well as having low input noise voltage (5nV/√Hz); 3) neural signals are very small and usually buried within a noisy background environment and therefore isolation of the signal requires a very accurate detection method such as the phase sensitive lock-in approach used by this signal acquisition system.

Figure 5-9 displays the experimental set up for the probe electrical characterization. Signals buried within the noisy background environment were recorded from the probe and first band-passed amplified prior to the phase sensitive processing algorithm. The phase sensitive process algorithm takes the input signal and multiplies it by a reference signal that exhibits the same frequency characteristics as the stimulus signal. The multiplied signals are then attenuated to zero if they are either not at the same frequency as the reference signal or out of phase. In other words, the reference signal helps pin point the

signal of interest while filtering out noise. The resultant signal is further amplified and sampled by a fast analog-to-digital converter and then processed in a real-time internal processing unit to display the data of interest.

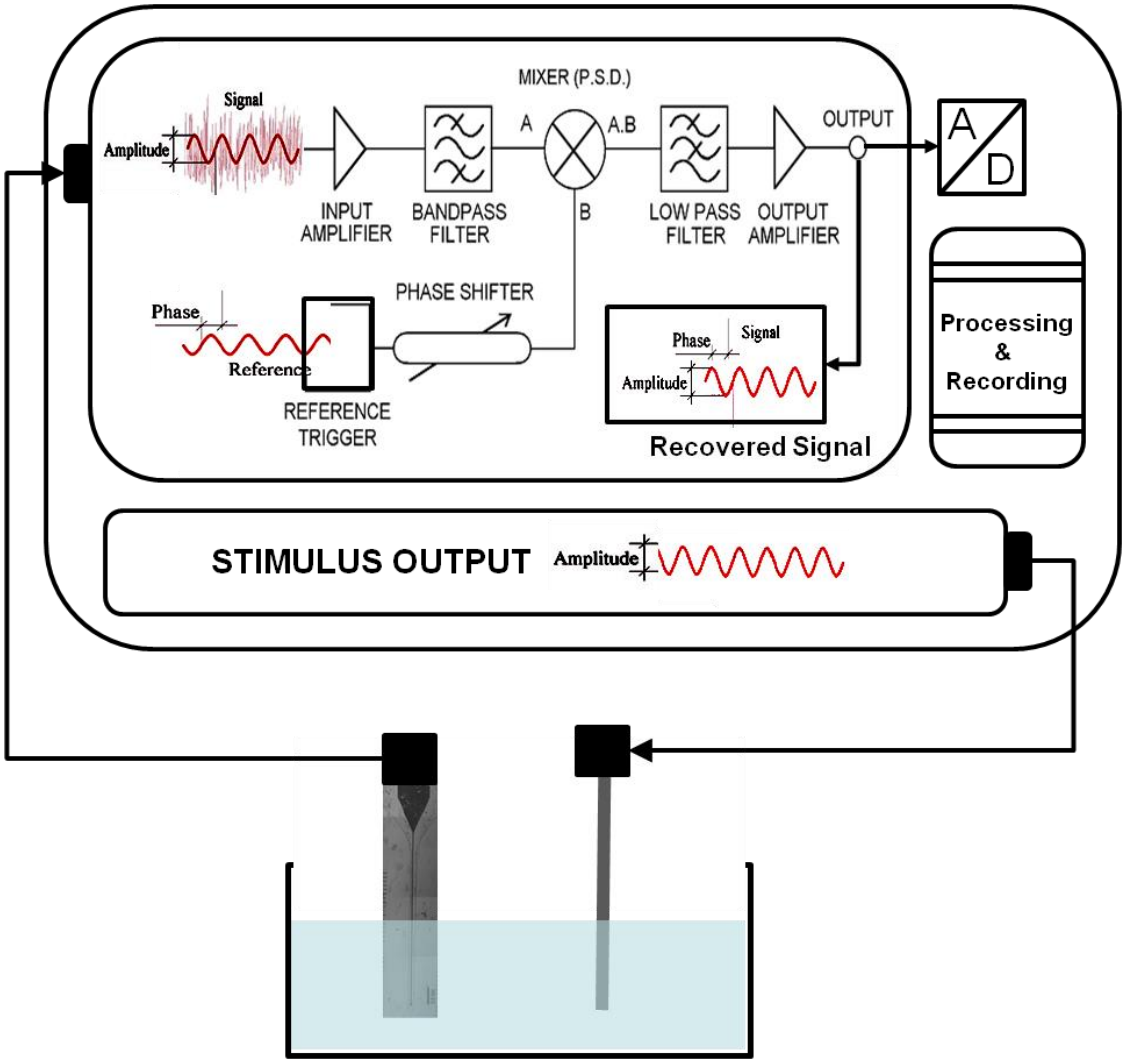

Figure 5-9: Experimental set up for the in vitro probe electrical characterization.

In order to connect the functional probe with the signal acquisition system, a copper wire was fixed onto the connection pad using the conductive glue (Conductive Epoxy, Circuirworks Inc., Somerville, NJ, USA). The whole device was fixed within a 24-well cell plate. A ground wire was fixed in the same well with a fixed distance between the wire and the electrode. The ground wire was connected to the stimulating end of the signal acquisition system and the electrode was connected to the receiving end of the signal acquisition system. Various experiments can then be performed adjusting parameters such as frequencies, voltages, different solution types, etc.

5.4.2 Phase 1: The functional probe operational verification

Series of experiments were performed to characterize the functional probe developed in this work. First, a conductivity experiment was performed. The probe was placed within solutions of varying conductivities (empty, 100, 500 and 1000 μS/cm). The solutions consist of sucrose, HEPES, and MgCl2.The solution conductivity was measured using a Conductivity/TDS Meter (Oakton Instruments, Vernon Hills, IL, USA). The pH of the buffer solution was measured with a Beckman 340 pH/Temp Meter (Beckmann Coulter, Inc., Fullerton CA) and maintained at 7.4. The electrode was stimulated with 200 mV @ 45 kHz and the current was recorded. Figure 5-10 displays the results for the conductivity experiment. The recorded currents were proportional to the solution conductivity values and the probe was capable of transmitting the signals with minimal fluctuations over a period of 1 minute. These results suggest the electrode was capable of acquiring accurate electrical signals within different solutions. Furthermore, the electrode

was able to sustain the signal over a period of time, therefore confirming signal recording stability.

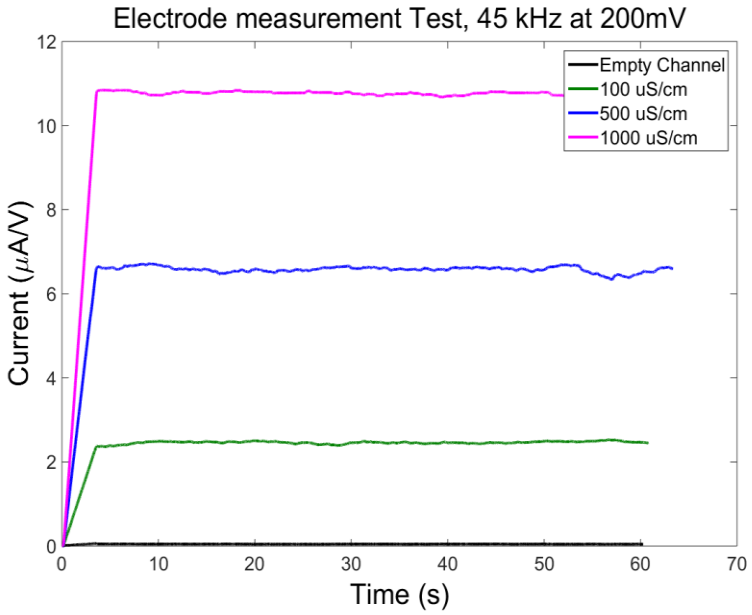

Figure 5-10: The conductivity experiment for the functional parylene probes. The electrode was stimulated at 200 mV @ 45 kHz within different solutions (100, 500 and 1000 µS/cm) and current readings were recorded.

The second experiment performed was an I-V curve evaluation. The purpose of the experiment was to evaluate the electrode sensitivity. The electrode was stimulated with a steadily increasing voltage (500-600 mV in 10 mV increments; 600-1000 mV in 100 mV increments) at 1 kHz. The current was then recorded for 10 seconds at each voltage value. These experiments were also performed using solutions of varying conductivities (100, 500 and 1000 µS/cm) to evaluate the probe sensitivity limits. Figure 5-11 displays the current values for the I-V curve experiments. The current readings were proportional to the

stimulating voltages and linearly tracked the incremental voltage changes. The results implied the electrode was sensitive to detect both smaller (10 mV increment) and larger (100 mV increment) voltage changes. Furthermore, the conductivity values of the solutions used in the experiments (1000, 500 and 100 µS/cm) were much lower than physiological relevant solutions such as PBS (15 mS/cm). The electrode's performance was stable (sustaining I-V cure proportionality) even within the solutions with low conductivities, and therefore confirmed the electrode's ability to detect small signals such as those produced from neurons. In summary, the I-V curve experiment concluded the electrode was sensitive to both small voltage changes and within small conductive environments.

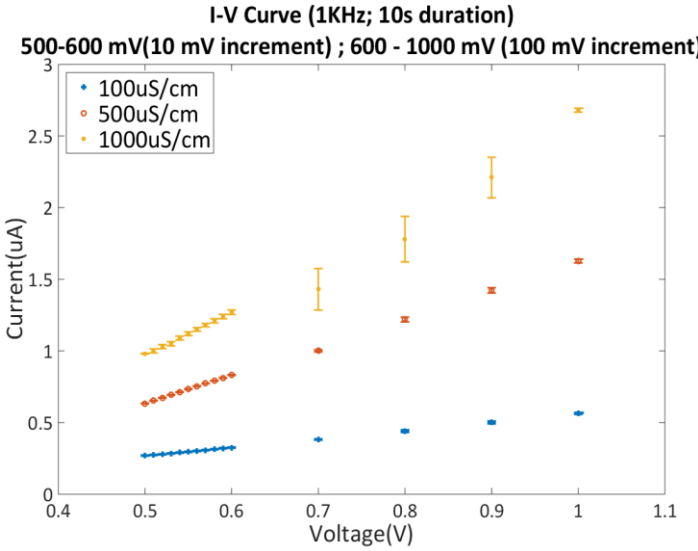

Figure 5-11: The I-V curve experiment. The electrode was stimulated at an increasing voltage recipe (500-600 mV with 10 mV increments; 600-1000 mV with 100 mV increments) at 1 kHz and current readings were recording. The experiments were also repeated within solutions of different condictivities (1000, 500 and 100 µS/cm)

The electrode was characterized by performing frequency sweeping experiments within different solutions. The electrode was placed within 1 mL of solution of varying conductivities (100, 500 and 1000 µS/cm). The electrode was then stimulated at 500 mV with a frequency sweep from 100 – 10 kHz and the impedance was monitored. For a solution using PBS (15 mS/cm), the electrode was stimulated at 50 mV with a frequency sweep from 100 – 10 kHz and the impedance was monitored. Figure 5-12 displays the recorded impedance vs. frequency within different solutions. The impedance values were compared to other probe devices described in the literature in order to access its feasibility for neuronal recording. The impedance at 1 kHz was chosen for comparison as it is the firing frequency for neural action potentials and therefore is physiologically relevant. The impedance values at 1 kHz for most neural probes range from ~50 kΩ to 1 MΩ in the literature[128,129,134]. The impedance values for the electrode within the 100, 500 and 1000 µS/cm solutions were within the MΩ range. The impedance value for the electrode within PBS solution was in the kΩ range. For both conditions, the impedance values were all within the desirable range for neural recording.

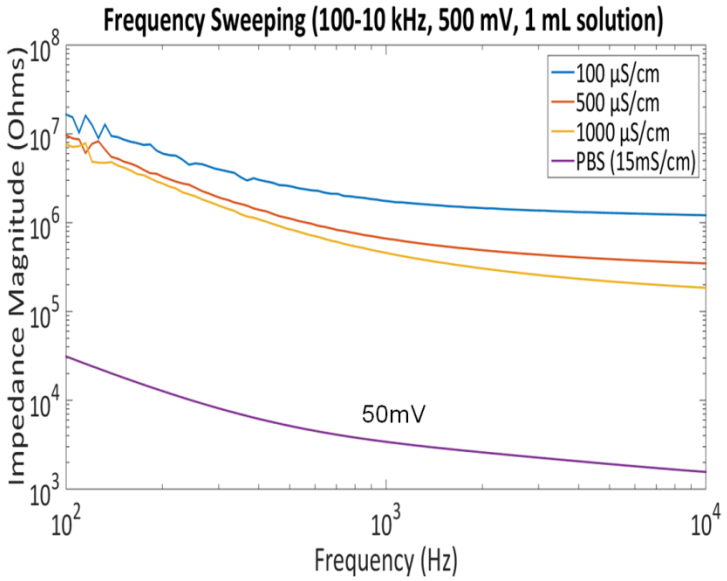

Figure 5-12: The impedance magnitude vs. frequncy within different solutions. The electrode was stimulated at various voltage (500 mV for 1000, 500 and 100 µS/cm solutions and 50 mV for PBS solutions). The freqeuncy was swept from 100 Hz to 10 kHz and the impedance was monitored.

In order to confirm the probe's sensitivity and functionality in complex biological environments such as the brain, identical electrical characterization previously performed in simple buffers was carried out in a more physiological relevant environment made of 0.5% electrophoresis grade agarose gel (Sigma-Aldrich Corp., St. Louis, MO, USA). 0.5% agarose gel has been widely characterized and identified as an ideal in vitro surrogate for the brain tissue[135]. Using this phantom, I aimed to simulate and elucidate how the electrode performs within the brain tissue. In the I-V curve experiment, the electrode was first stimulated with an incrementing voltage at a 5 mV step from 5-30 mV, followed by a 10 mV step from 30-100 mV at 1 kHz. Both the electrode and the reference wire was spatially

fixed using epoxy to prevent unwanted movement which may lead to inconsistent readings. In the frequency sweeping experiment, the electrode was stimulated at 50 mV with a frequency sweep from 100 – 1200 Hz and the impedance was monitored within the PBS solution and agarose gel.

Figure 5-13 (A) displays the results of the I-V curve experiments in both the 1X PBS buffer and 0.5% agarose gel. The electrical current response is linearly proportional to the voltage increments. The electrode correctly detects a lower current reading for agarose gel due to the increased density and structural hindrance of the agarose gel in the PBS solution. For the frequency sweeping experiment, the impedance readings were ~4189 Ω within the 0.5% agarose gel and ~ 3758 Ω within the PBS solutions at 1 kHz (Figure 5-13(B)). The higher impedance reading within the agarose gel was expected as it is a more heterogeneous environment compare to the PBS solution. These electrical characterizations within the PBS and the agarose gel were comparable to each other, which indicate that the electrode maintained its characteristics even within a more complex environment.

In conclusion, the phase 1 electrode characterization evaluated and confirmed that the electrode exhibited satisfactory properties required for neural recording (stability, sensitivity and capability). A phase 2 characterization was performed to investigate the effects of the polymer coating fabrication and degradation procedures on device electrical properties.

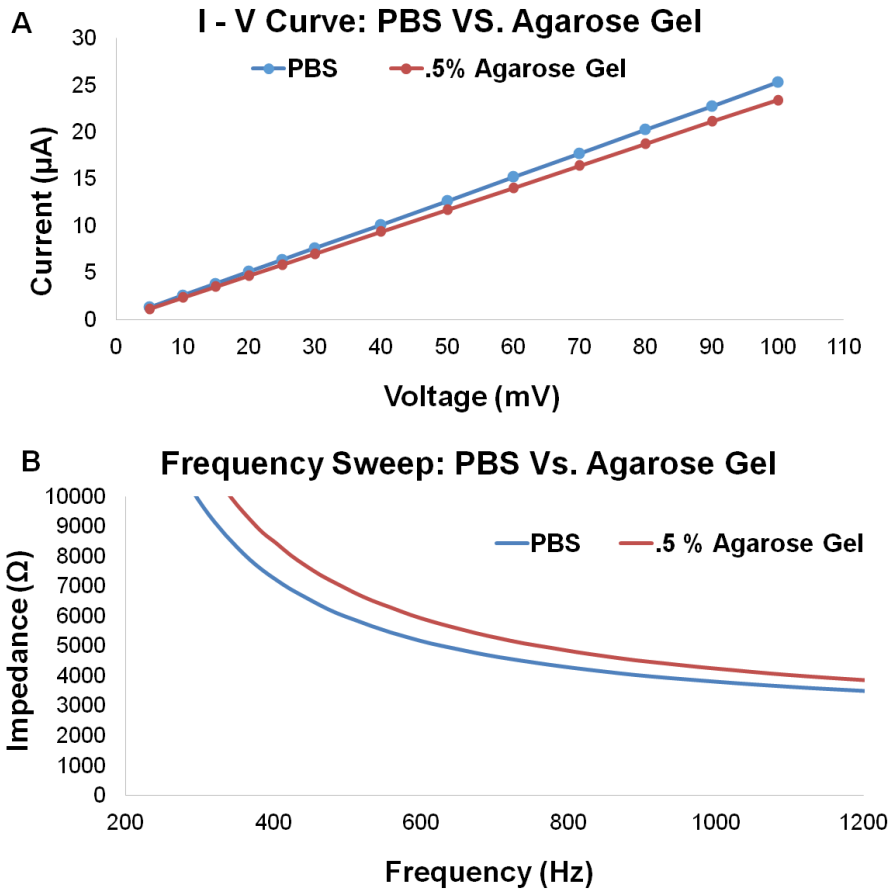

Figure 5-13: (A) The I-V curve experiment within the PBS solution and 0.5% agarose gel. The electrode was stimulated with a steadily increasing voltage (5-30 mV in 5 mV increments; 30-100 mV in 10 mV increments) at 1 kHz. (B) The impedance magnitude vs. frequncy within PBS and 0.5% agarose gel. The electrode was stimulated at 50 mV. The freqeuncy was swept from 100 Hz to 1200 kHz and the impedance was monitored.

5.4.3 Phase 2: Polymer degradation characterization

The phase 2 characterization investigated the effects of the polymer coating procedures and degradation on electrode properties. The purpose of the experiments was to evaluate whether the electrode was intact to sustain recording performance following polymer treatments.

The experimental set up was the same as described in the previous section (Chapter 5.4.1). The electrode was fixed within one of the wells of a 24-well cell culture plate. A ground copper wire was placed within the same well so that the distance between the electrode and the copper wire was fixed throughout the experiment. The well was filled with 5 mL of PBS at 37°C and the whole plate was covered with parafilm to minimize solution evaporation that might affect the impedance recording. An uncoated probe was first recorded at 50 mV and 1 kHz for 30 minutes as the baseline control impedance. The same probe was then coated with E5005(2K) using the procedure described previously (Chapter 3.2.3) and fixed in the recording cell well. The recording began when the PBS solution was added to the well and the impedance values were monitored continuously until the polymer coating degraded/eroded from the electrode.

Figure 5-14 displays the electrode impedance over time during the polymer degradation/erosion. The baseline control impedance for uncoated probe was ~3.5 kΩ. For the coated probe, an initial impedance of 6 kΩ was recorded when the PBS solution was added to the recording reservoir. A higher impedance was expected since the E5005(2K)

polymer is an insulating dielectric material. The measured impedance dropped rapidly over the first 30 minutes following PBS addition, indicating polymer resorption/degradation allowing contact of the probe recording window with the adjacent solution. 80 minutes following PBS addition to the recording reservoir, the impedance reached a steady state value of ~ 3.5 kΩ, which closely agreed with the original measured impedance of the uncoated probe.

These results imply that the polymer erosion/degradation occurred rapidly, and the probe was capable of recording (with higher impedance) without complete polymer dissolution. Second, the impedance reading reached to steady state ~ 80~120 minutes after the probe was immersed with PBS solution, implying complete polymer dissolution. This result agrees with the previous polymer degradation characterization using fluorescent dye (Chapter 3.2.2.2), which indicated complete polymer dissolution 120 minutes after insertion into a brain phantom agarose gel. Agreement between the two experiments confirms the polymer degradation behaviors, which can be useful for future animal study designs. Finally, agreements between coated probe impedance at steady state and the uncoated probe (both ~ 3.5 kΩ) also implies the electrode remained intact during the polymer coating and degradation, which confirms the functional polymer coated parylene fabrication procedure.

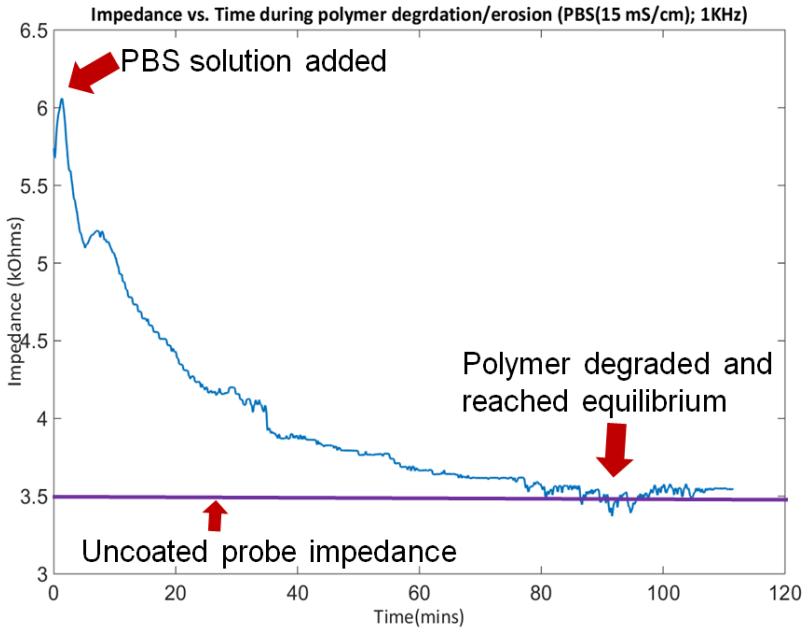

Figure 5-14: Impedance vs. time during polymer degrading/erosion. Device dimension: The probe: 90 µm wide and 3.5 mm long. The polymer coating: 100 µm wide, 100 µm thick and 4 mm long.

CHAPTER 6 CONCLUSION AND FUTURE WORK

Smaller and more flexible neural probes are hypothesized to allow better long term integration with neural tissue, which limits the mechanical disruption of tissue and long-term shearing by being flexible enough to deform with the surrounding brain tissue during movement. However, such devices require insertion aids to provide enough mechanical support to penetrate the brain. In this work, I developed miniaturized parylene probes with a tyrosine-derived polycarbonate coating which provides sufficient rigidity for device insertion while degrading quickly (within hours) to enable long-term neural signal recordings. PDMS was used as the substrate to provide sufficient bonding to conduct photolithography for probe fabrication and polymer coating, while still allowing mechanical lifting off of the device. The polymer coated probes were mechanically characterized *ex vivo* to confirm probe integrity. They were also characterized chemically to confirm that the polymer coatings eroded within 2 hours while leaving the probe intact. This work also demonstrates the ability to reproduce consistent polymer-coated probes.

I also investigated effects of different design parameters on tissue response progression. Probe candidates of varying probe and polymer coating sizes were implanted into rat brains. The brains were harvested at different time points ranging from short (72 hours) to long (24 weeks) terms. Tissue damage was evaluated using immunohistochemistry to monitor glial cell (astrocytes and microglia) response.

Experimental results demonstrated that both polymer coating and probe sizes played roles in glial scar response with respect to different glial cell types.

Microglia was extensively activated at the early post implantation stages (couple of days) to trigger a wound healing response. This early tissue response was independent from the probe and polymer coating sizes. Microglia activation subsided within 10 days after device implantation for smaller coating sizes. The microglia was activated again 3 weeks after device implantation for larger probe and/or coating sizes, indicating neuro-inflammation and the onset of the chronic tissue response. The level of microglia activation was correlated to polymer and probe sizes where larger coating/probe sized devices exhibited more activated microglia around the implantation sites. On the other hand, reactive astrocytes were not observed around the implantation sites at the early post implantation stage , mainly because the injury site were pre-occupied by microglia and macrophage cells for the wound healing response. As the time progressed, astrocytes formed glial scar around the implantation sites. The level of astrocyte activation was also highly correlated to the polymer and probe sizes where the larger probe and polymer coating devices introduced a thicker glial scar formation 24 weeks following device implantation.

Experimental results showed that the larger coating devices (200 μm wide × 200 μm thick) with the same sized probe encapsulation exhibited significantly more activated astrocytes and microglia around the implantation sites than the smaller coating devices

(100 μm wide × 100 μm thick) at both short and long term time points. This was an unexpected result that the polymer coating size in this range would have such a significant effect on the long term tissue response as the polymer degrades after only couple hours following device implantation. These results imply that if the initial mechanical trauma caused by device insertion is too severe, the wound might not be able to be healed and recovered properly and may therefore promote a longer term glial scar response. Future investigation can be performed to implant a large polymer coated probe into the rat brain and extract the device soon after implantation to create a "stab wound". The animal will then be sacrificed at different time points ranging from short and long term to investigate how the glial cells respond to the mechanical trauma caused by the device implantation and whether 1) the small probe encapsulation and/or 2) polymer dissolution within in the tissue play effects in tissue response progression.

Device cross sectional area and geometry aspect ratio might also be parameters that affect tissue response. A 200 μm wide × 200 μm (cross sectional area of 40,000 μm^2) thick polymer coating with a 30 μm wide × 5 μm thick probe introduced more astrocytes and microglia activation 12 weeks after device implantation compared to a 350 μm wide × 100 μm (cross sectional area of 35,000 μm^2) thick polymer coating with a 320 μm × 5 μm thick probe. These results were unexpected as the latter device incorporated a much larger probe within the polymer coating. It was hypothesized that cells may heal more easily if the wound geometry is flatter and/or the larger the cross sectional area induces a more severe tissue response. Future experiments would be needed to insert polymer coated devices with

the same cross sectional area but different geometry aspect ratios with and without probe encapsulation in order to further confirm the hypothesis.

Most importantly, a 30 μm wide × 5 μm probe with a 100 μm thick × 100 μm wide polymer coating exhibited a significantly less amount of tissue response compared to a 80 μm wide × 5 μm probe with 100 μm thick × 100 μm wide polymer coating, indicating that probe size is also an factor that affects the long term glial scar formation. Furthermore, the tissue response induced by the small probe coated with the small coating was statistically the same as a pure small polymer coating device without any encapsulated probe at 24 weeks. These results suggest that the 30 μm wide × 5 μm thick probe is the ideal size candidate for long term signal recording because it is able to attenuate long term tissue response. However, a wider probe is more desirable as it can incorporate more electrodes to increase recording efficiency. Future studies would evaluate the tradeoff between size and electrode placement in the tissue response induced by devices that are wider than 30 μm but smaller than 80 μm for more ideal recording efficiency.

From the in vivo animal study, I have evaluated glial cells response (microglia and astrocytes) to devices with different dimensions in both the short and long term. For future studies, different cells can be stained and monitored. Neurons can be stained to investigate if there is any neuronal loss around the implantation sites during device implantation. Loss of neurons around the implantation sites increases difficulties for electrode to record neural action potentials and therefore is less desirable. Immunoglobulin-G (IgG) can also be used

to stain for vascular leakage, which is normally not seen within the brain tissue. IgG can be an important indicator for blood brain barrier (BBB) leakage induced by device implantation. Nestin and Doublecortin (DCX) can be used to investigate tissue regeneration as they are indicators for neuronal differentiation within the central nervous system. It is essential to understand whether or how the tissues recover from the mechanical insult by device implantation. It will be beneficial to monitor different cell types along with the glial cells and investigate interactions between different cell types for a more systematic understanding in electrode-tissue interface.

Finally, the parylene probe was functionalized by patterning electrodes along the probe shank. Single electrode probes were fabricated and physically examined to ensure device integrity. The functional probe was evaluated to confirm that the electrode exhibited satisfactory properties required for neural recording (capability, stability and sensitivity). The probe was also characterized by monitoring the electrode impedance change within a PBS solution before and after polymer dissolution. The electrode exhibited an impedance of ~3.5 kΩ at 1 kHz after complete polymer dissolution and this value is within the desired impedance range for neural action potential recording. Experimental results also showed the electrode impedance was comparable before and after polymer degradation, which implies the electrode remains intact during polymer coating and polymer degradation, which validated the functional polymer coated parylene fabrication procedure. Future work will expand the fabrication process from one single electrode to multiple electrodes. Technical challenges for electrode expansion will be the device dimension limitation and

fabrication difficulties. First, the in vivo evaluation suggests that a 30 μm wide probe is the ideal probe candidate to minimize long term tissue response. However, the 30 μm wide probe would most likely only allow a single electrode. It will be more desirable to fabricate at least two electrodes on the probe, and therefore an additional study might be needed to evaluate if a probe that has a width between 30-80 μm can still help minimize the tissue response. Second, multiple electrodes require multiple connecting traces and connection pads. A higher resolution mask would be required for feature alignment in order to achieve high product yield.

In conclusion, the development of a flexible miniaturized neural probe coated with an ultra fast degrading polymer as a temporary insertion aid was demonstrated. Effects of different device parameters on tissue response progression using non-functional probes have also been investigated. Future work for this project will focus on evaluating the in vivo electrical recording performance. I have evaluated the probe using an in vitro model for feasibility and functionality. The polymer coated probe will be implanted into a rat brain to first validate device recording capability by extracting single-unit action potentials or local field potentials (LFP). The final probe candidates with different dimensions will then be implanted within the rat brains for longer period of time to evaluate signal recording consistency. The long term recording experiment will also aim to confirm the hypothesis that a smaller and more flexible probe is capable of attenuate tissue response and therefore exhibits prolonged recording performance with high signal-to-noise ratio and low impedance.

APPEDIX A ANIMAL STUDY

A.1 Individual device intensity vs. time points (GFAP Staining)

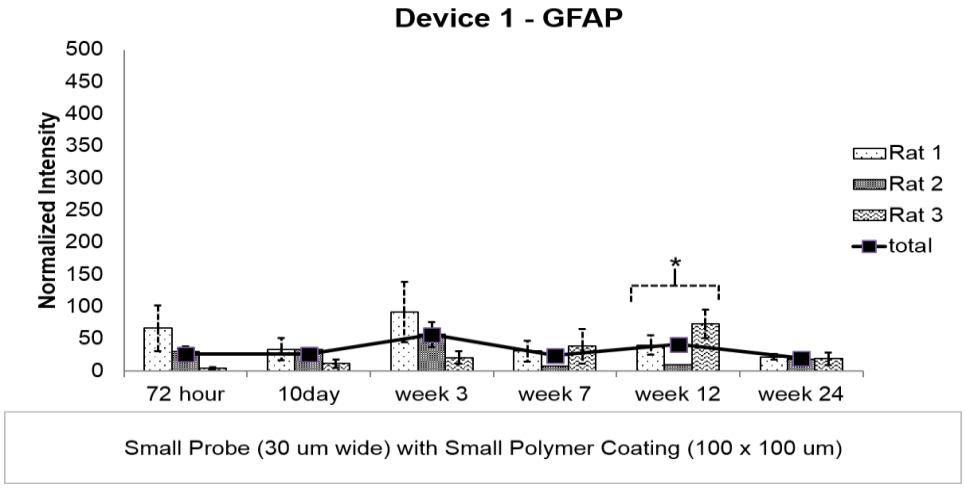

Figure A.1.1 : Normalized intensity for GFAP staining vs. time points for Device 1. Device dimension : The probe : 30 µm × 5 µm × 3.5 mm. The polymer coating: 100 µm × 100 µm × 4 mm.

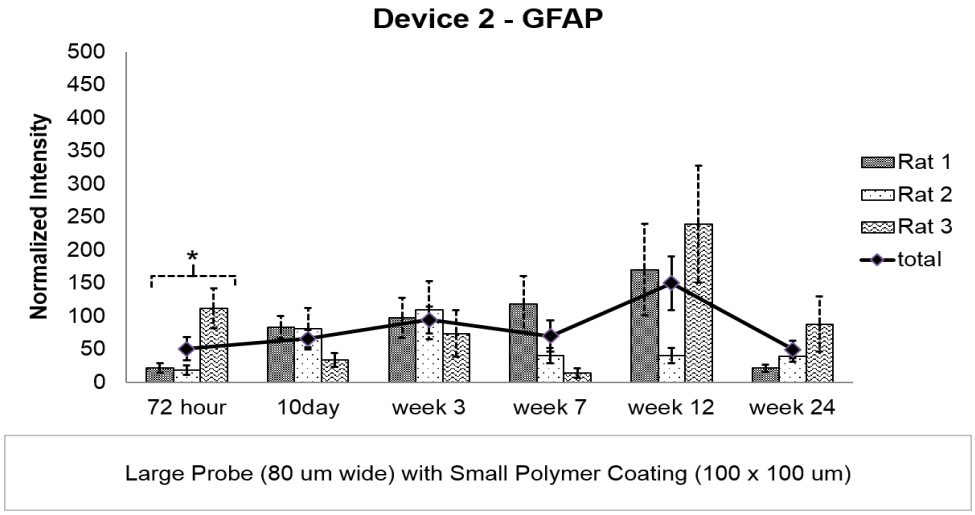

Figure A.1.2 : Normalized intensity for GFAP staining vs. time points for Device 2. Device dimension : The probe : 80 µm × 5 µm × 3.5 mm. The polymer coating: 100 µm × 100 µm × 4 mm.

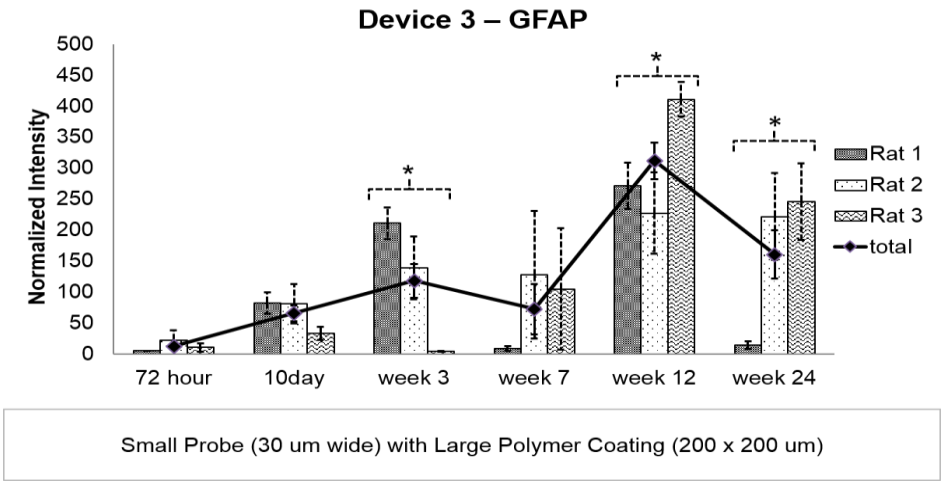

Figure A.1.3 : Normalized intensity for GFAP staining vs. time points for Device 3. Device dimension : The probe : 30 µm × 5 µm × 3.5 mm. The polymer coating: 200 µm × 200 µm × 4 mm.

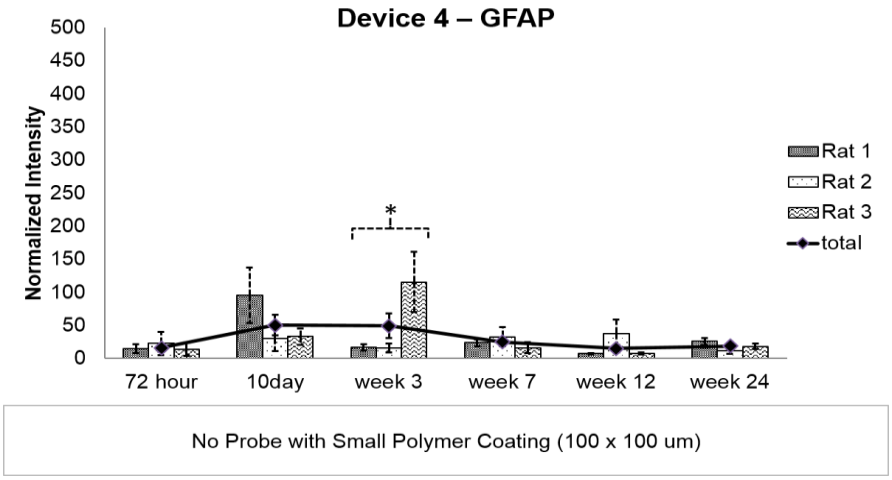

Figure A.1.4 : Normalized intensity for GFAP staining vs. time points for Device 4. Device dimension : The probe : no probe. The polymer coating: 100 µm × 100 µm × 4 mm.

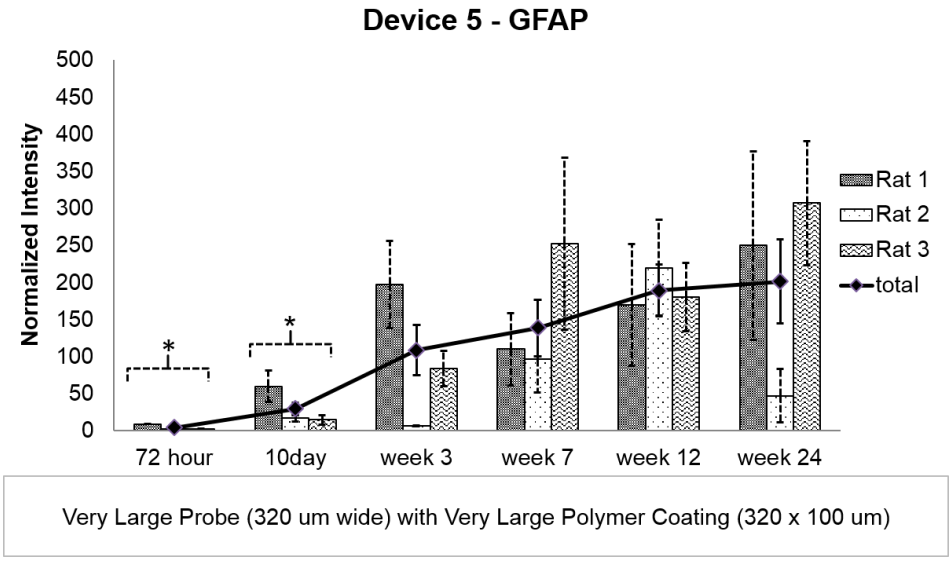

Figure A.1.5 : Normalized intensity for GFAP staining vs. time points for Device 5. Device dimension : The probe : 320 µm × 5 µm × 3.5 mm. The polymer coating: 350 µm × 100 µm × 4 mm.

A.2 Normalized intensity vs. distance from the center of the implantation site (GFAP staining)

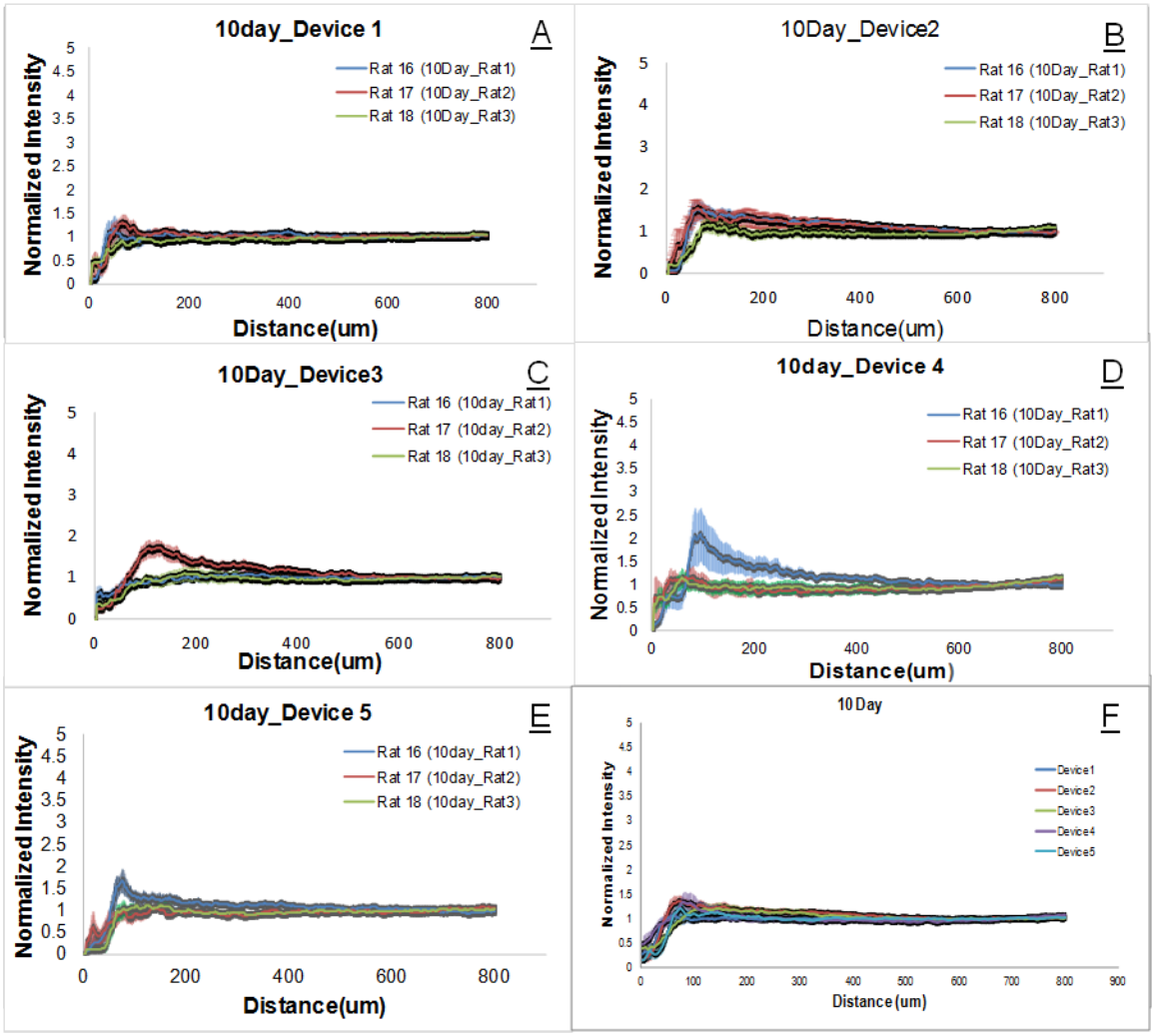

Figure A.2.2 : (A-E) Normallized intensity of GFAP staining vs. distance from the center of the implantation sites for 5 devices at 10 Days. (F) Normallized intensity of GFAP staining vs. distance from the center of the implantation sites. The intensity values were averaged across 3 animals within the time point.

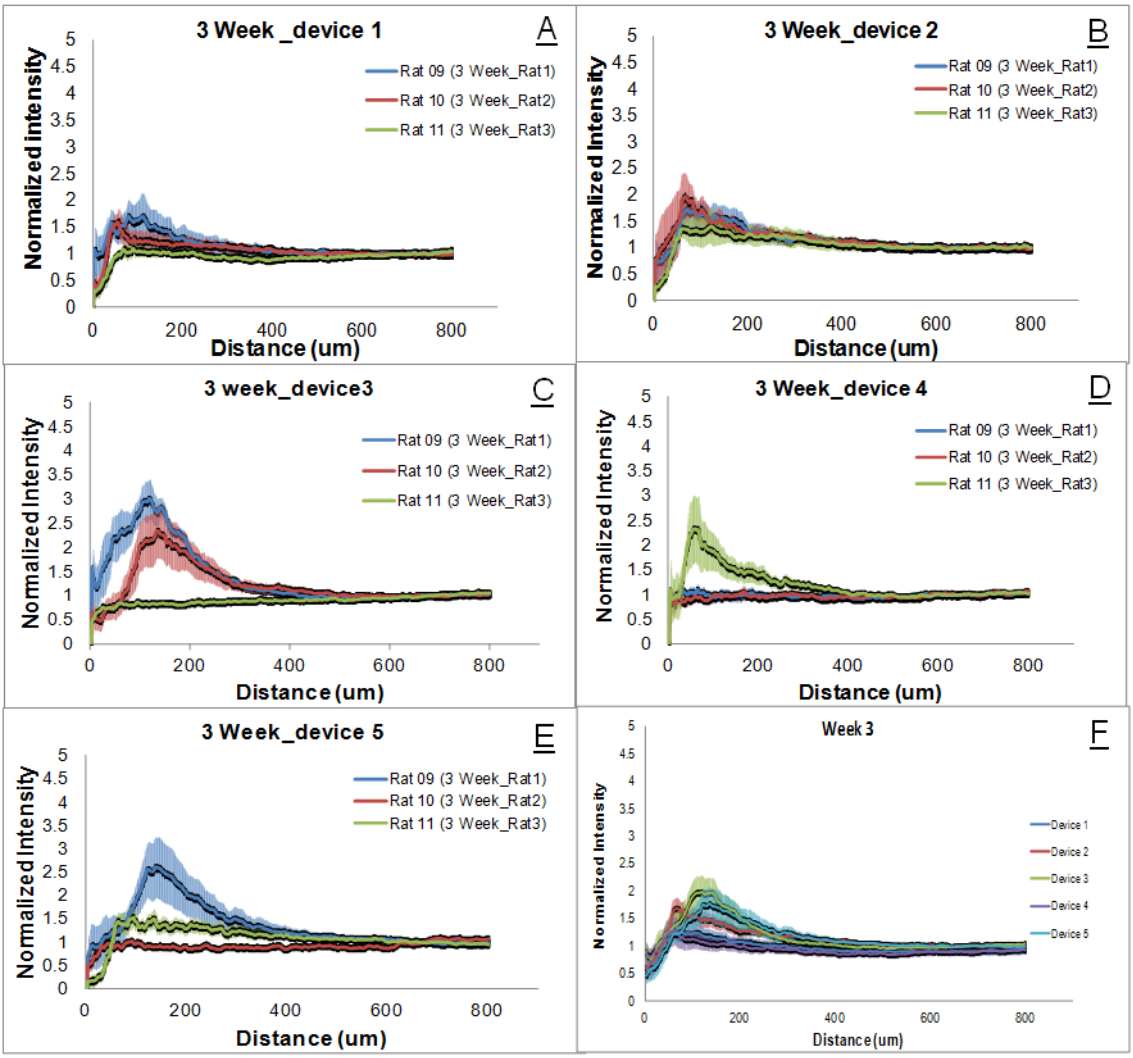

Figure A.2.3 : (A-E) Normallized intensity of GFAP staining vs. distance from the center of the implantation sites for 5 devices at 3 Weeks. (F) Normallized intensity of GFAP staining vs. distance from the center of the implantation sites. The intensity values were averaged across 3 animals within the time point.

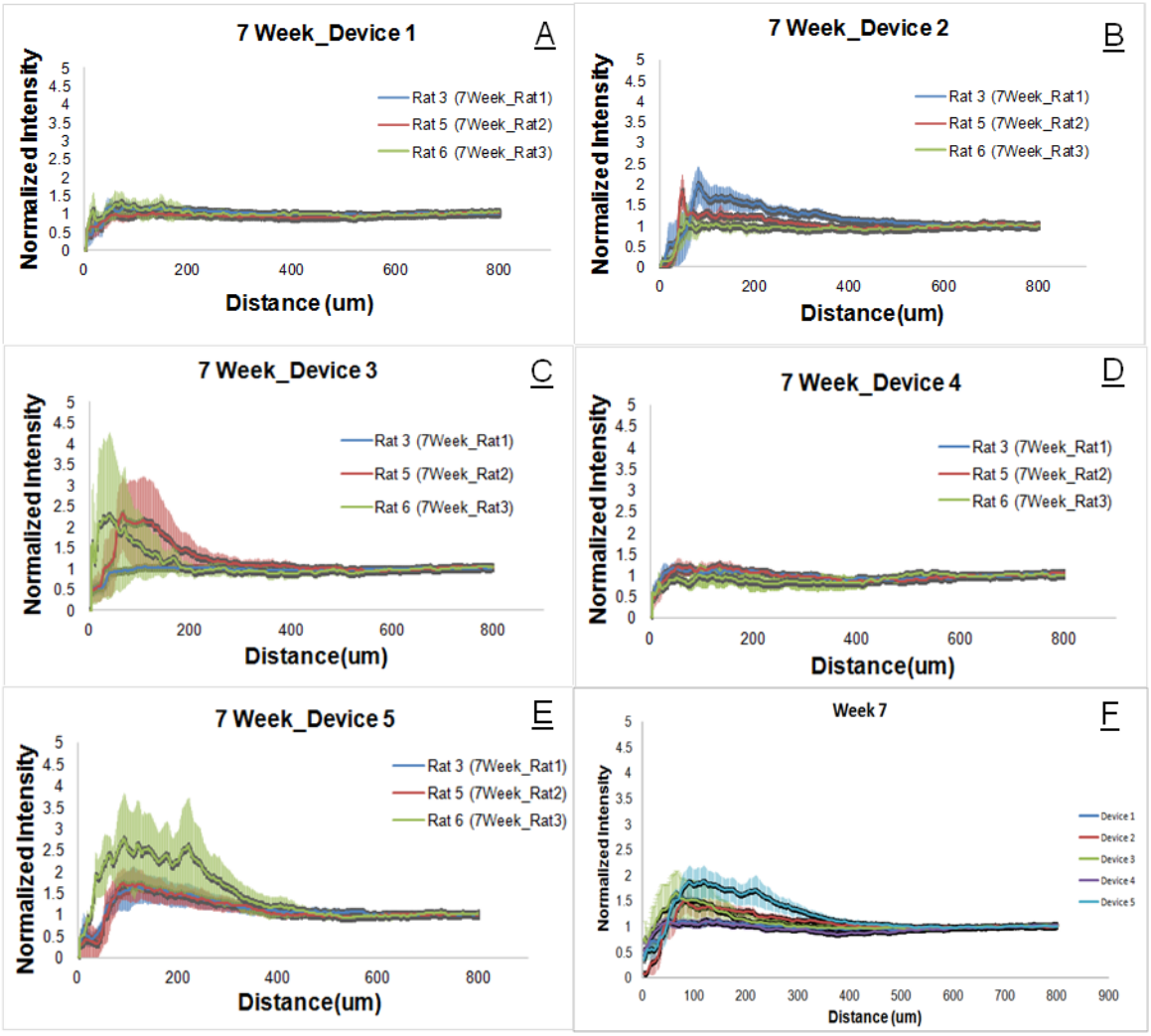

Figure A.2.4 : (A-E) Normallized intensity of GFAP staining vs. distance from the center of the implantation sites for 5 devices at 7 Weeks. (F) Normallized intensity of GFAP staining vs. distance from the center of the implantation sites. The intensity values were averaged across 3 animals within the time point.

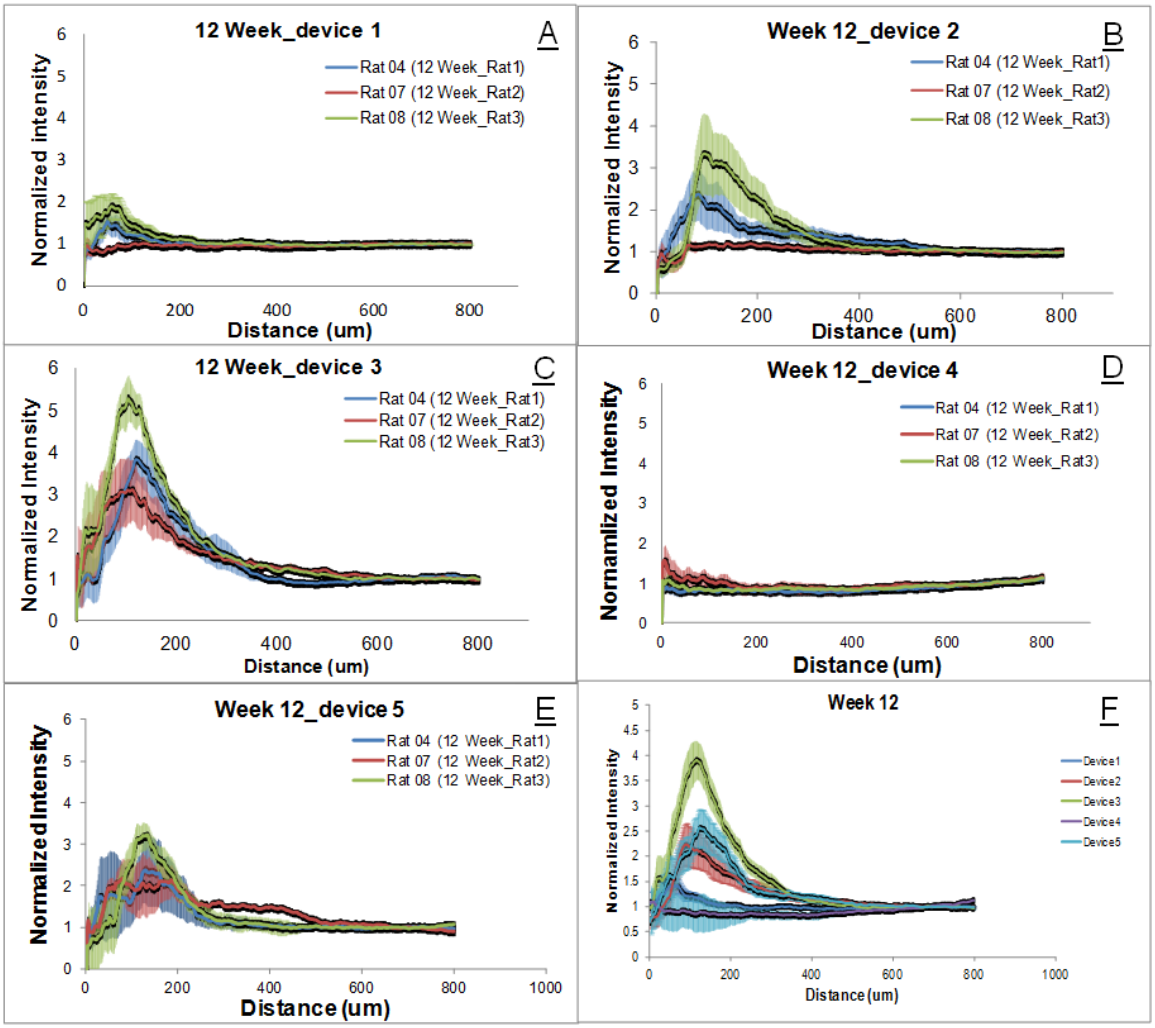

Figure A.2.5 : (A-E) Normallized intensity of GFAP staining vs. distance from the center of the implantation sites for 5 devices at 12 Weeks. (F) Normallized intensity of GFAP staining vs. distance from the center of the implantation sites. The intensity values were averaged across 3 animals within the time point.

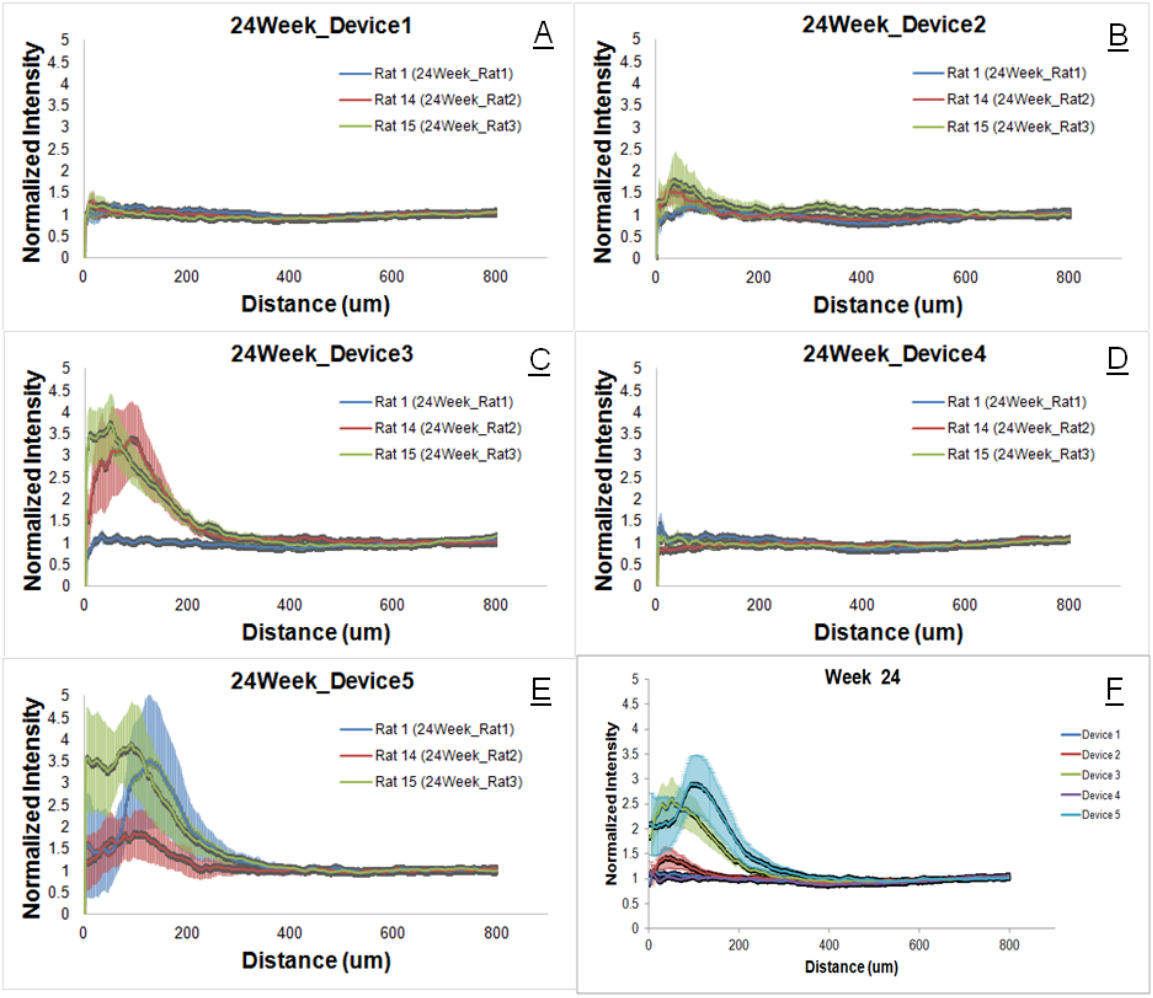

Figure A.2.6 : (A-E) Normallized intensity of GFAP staining vs. distance from the center of the implantation sites for 5 devices at 24 Weeks. (F) Normallized intensity of GFAP staining vs. distance from the center of the implantation sites. The intensity values were averaged across 3 animals within the time point.

A.3 Individual device intensity vs. time points (Iba-1 Staining)

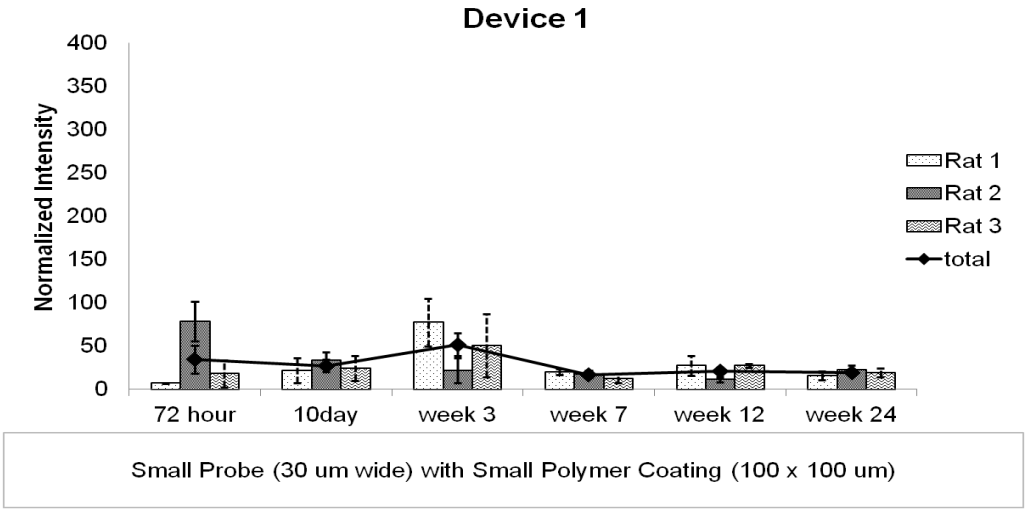

Figure A.3.1 : Normalized intensity for Iba-1 staining vs. time points for Device 1. Device dimension : The probe : 30 µm × 5 µm × 3.5 mm. The polymer coating: 100 µm × 100 µm × 4 mm.

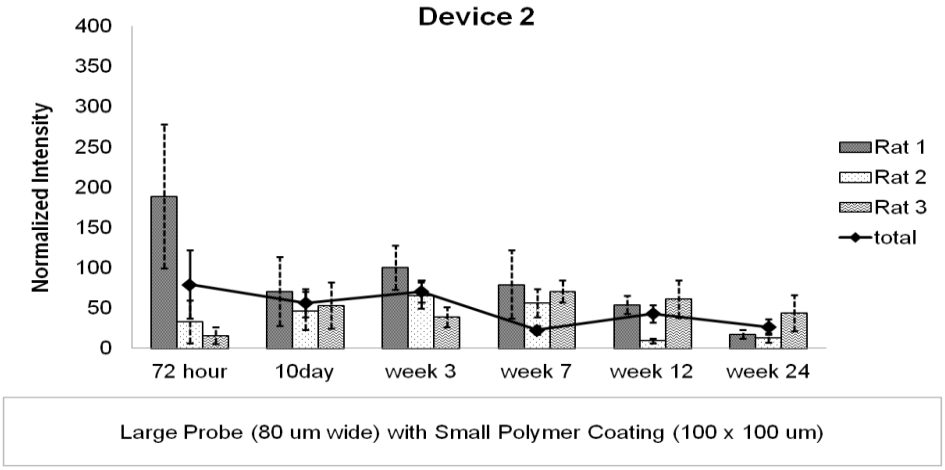

Figure A.3.2 : Normalized intensity for Iba-1 staining vs. time points for Device 2. Device dimension : The probe : 80 µm × 5 µm × 3.5 mm. The polymer coating: 100 µm × 100 µm × 4 mm.

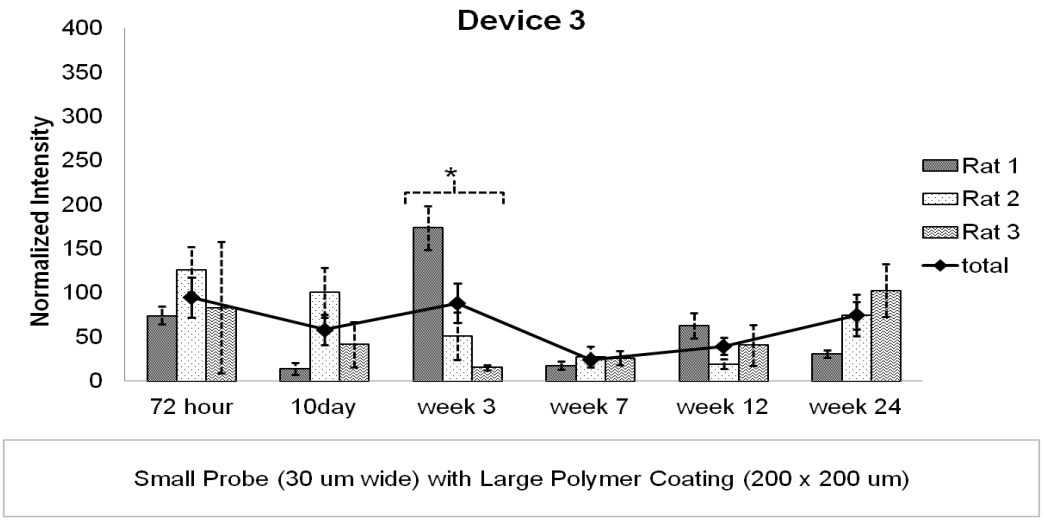

Figure A.3.3 : Normalized intensity for Iba-1 staining vs. time points for Device 3. Device dimension : The probe : 30 µm × 5 µm × 3.5 mm. The polymer coating: 200 µm × 200 µm × 4 mm.

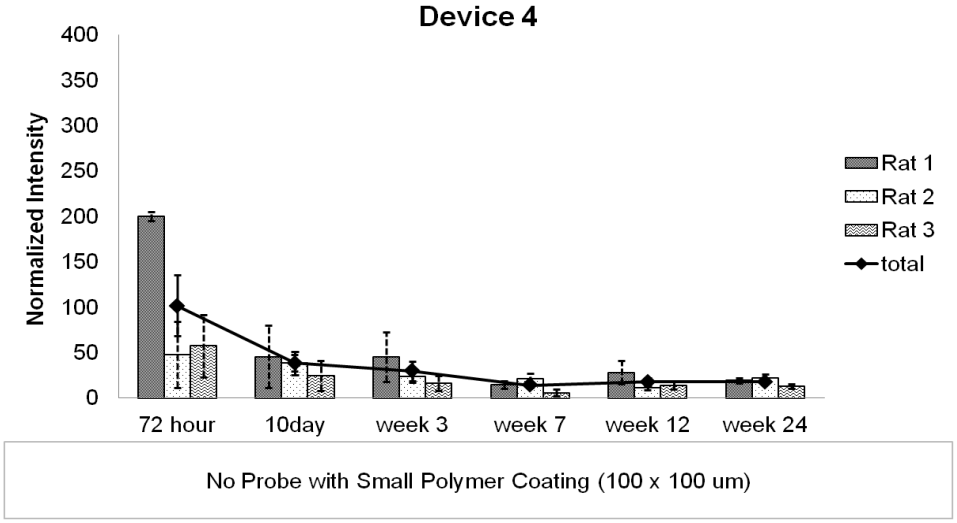

Figure A.3.4 : Normalized intensity for Iba-1 staining vs. time points for Device 4. Device dimension : The probe : no probe. The polymer coating: 100 µm × 100 µm × 4 mm.

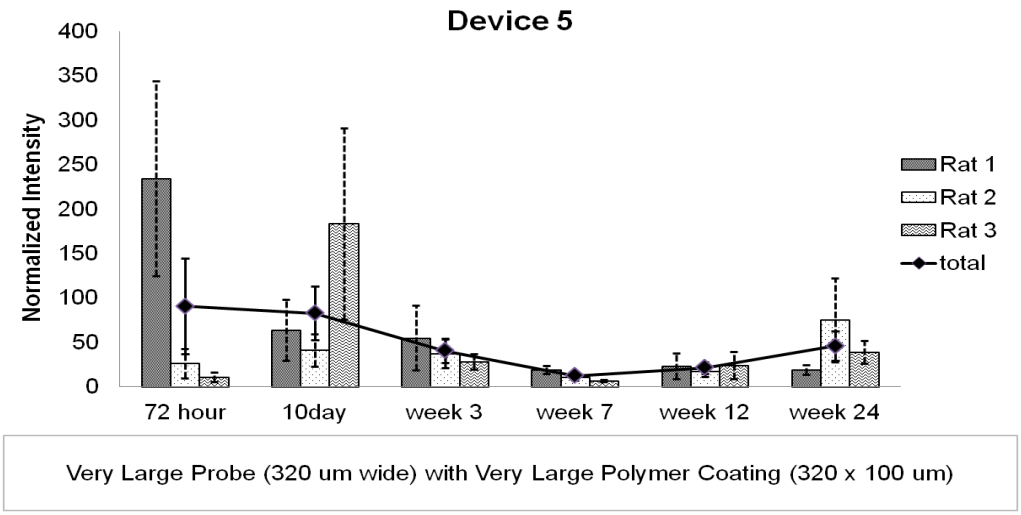

Figure A.3.5 : Normalized intensity for Iba-1 staining vs. time points for Device 5. Device dimension : The probe : 320 µm × 5 µm × 3.5 mm. The polymer coating: 350 µm × 100 µm × 4 mm.

A.4 Normalized intensity vs. Distance from the center of the implantation site (Iba-1 staining)

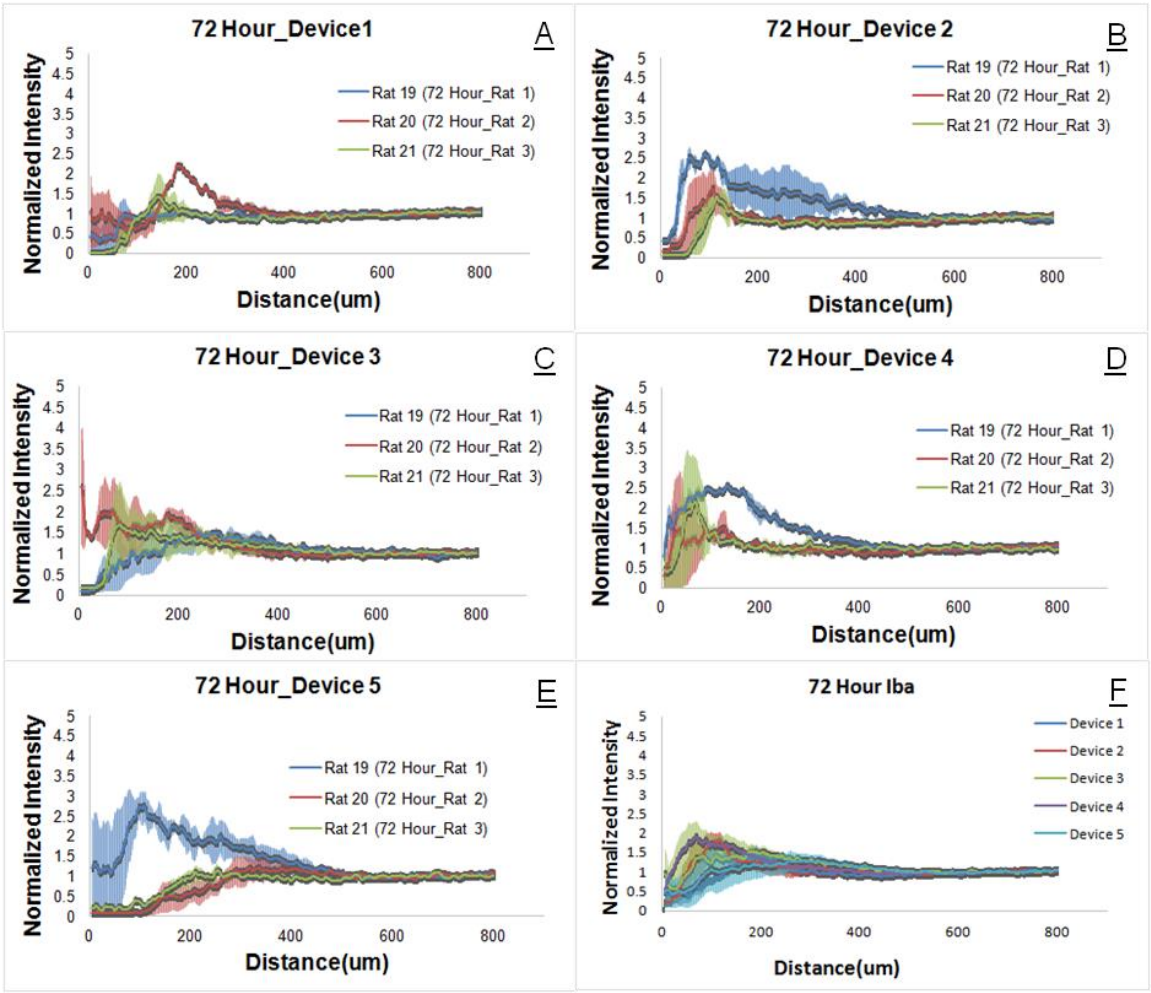

Figure A.4.1 : (A-E) Normallized intensity of Iba-1 staining vs. distance from the center of the implantation sites for 5 devices at 72 hours. (F) Normallized intensity of Iba-1 staining vs. distance from the center of the implantation sites. The intensity values were averaged across 3 animals within the time point.

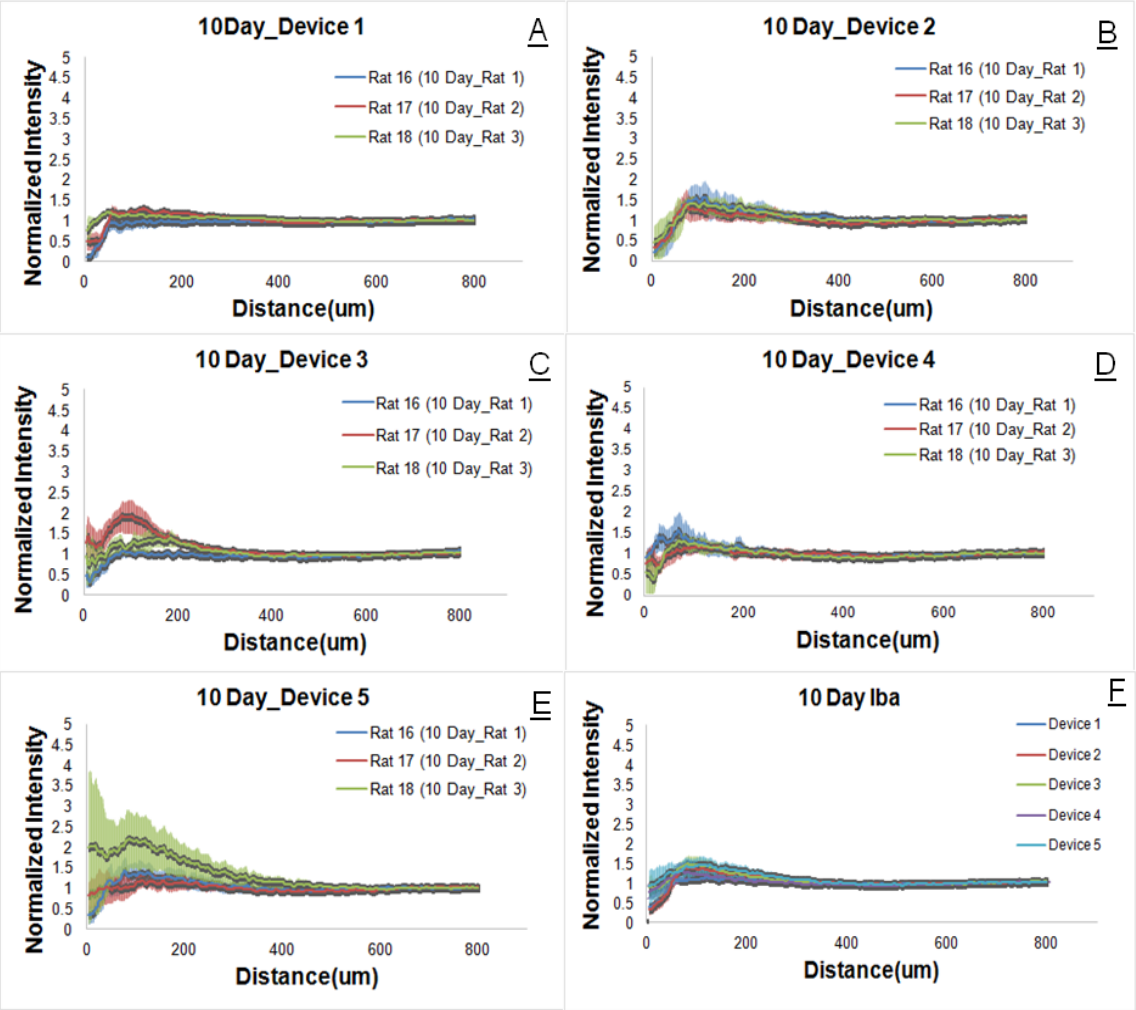

Figure A.4.2 : (A-E) Normallized intensity of Iba-1 staining vs. distance from the center of the implantation sites for 5 devices at 10 Days. (F) Normallized intensity of Iba-1 staining vs. distance from the center of the implantation sites. The intensity values were averaged across 3 animals within the time point.

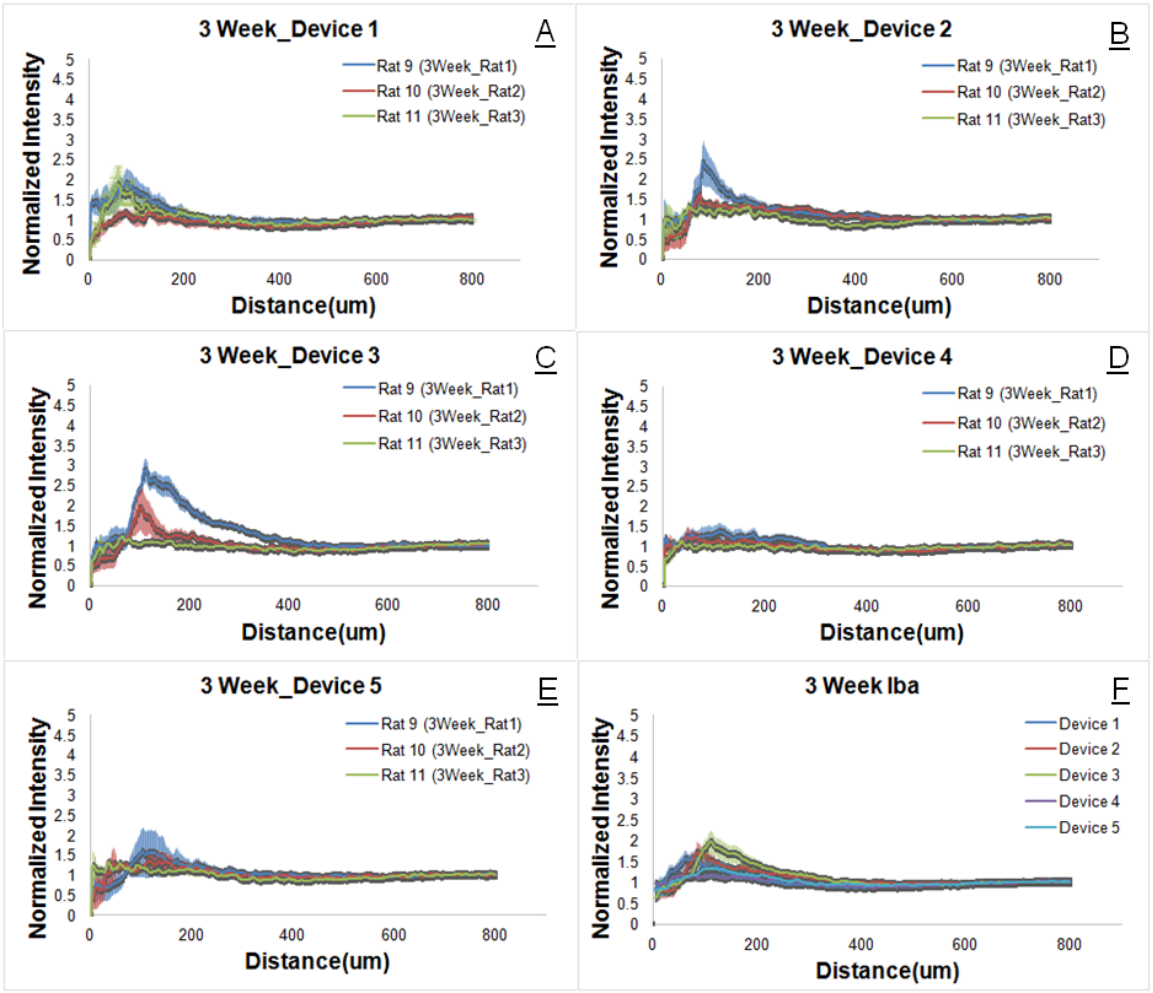

Figure A.4.3 : (A-E) Normallized intensity of Iba-1 staining vs. distance from the center of the implantation sites for 5 devices at 3 Weeks. (F) Normallized intensity of Iba-1 staining vs. distance from the center of the implantation sites. The intensity values were averaged across 3 animals within the time point.

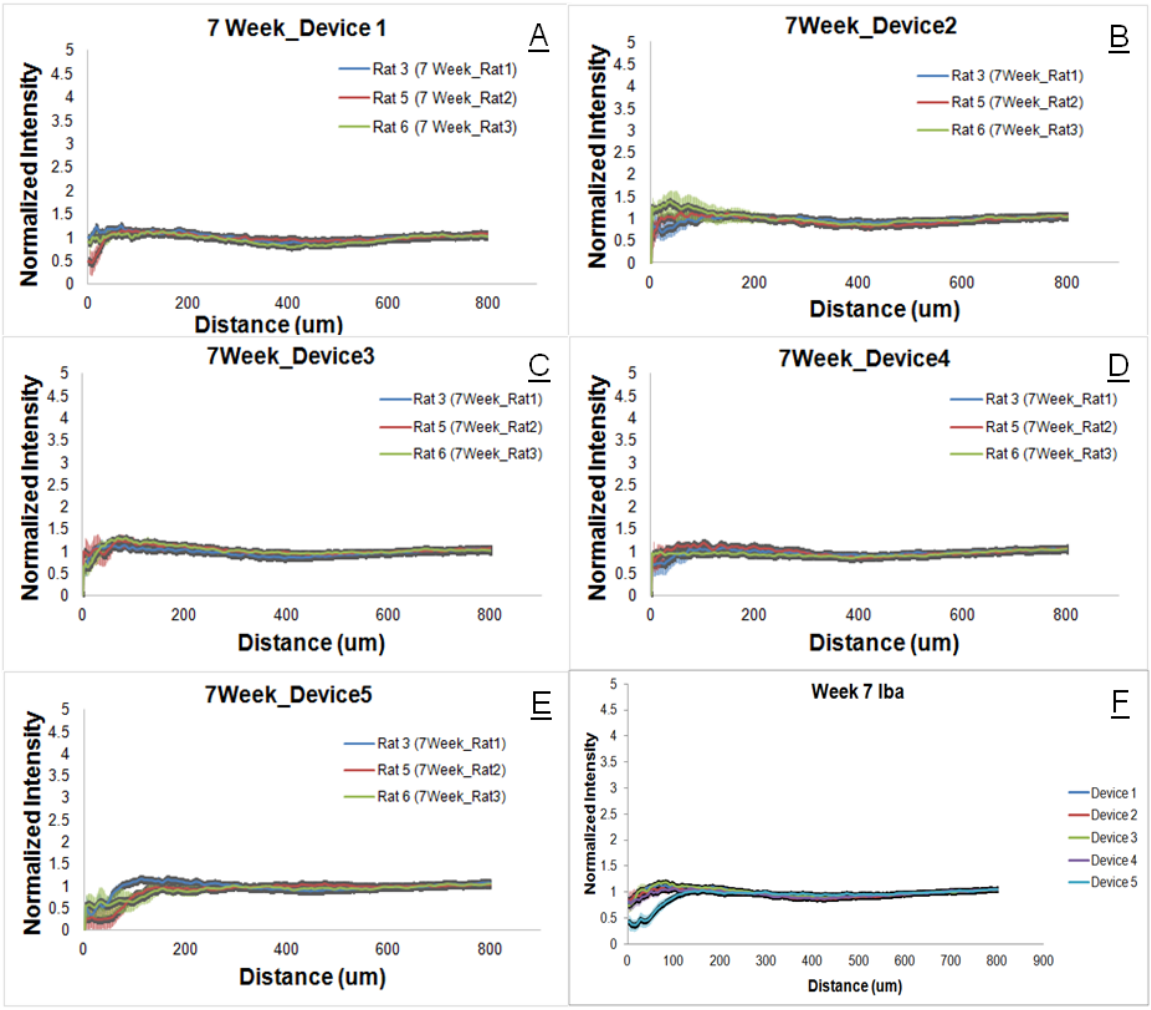

Figure A.4.4 : (A-E) Normallized intensity of Iba-1 staining vs. distance from the center of the implantation sites for 5 devices at 7 Weeks. (F) Normallized intensity of Iba-1 staining vs. distance from the center of the implantation sites. The intensity values were averaged across 3 animals within the time point.

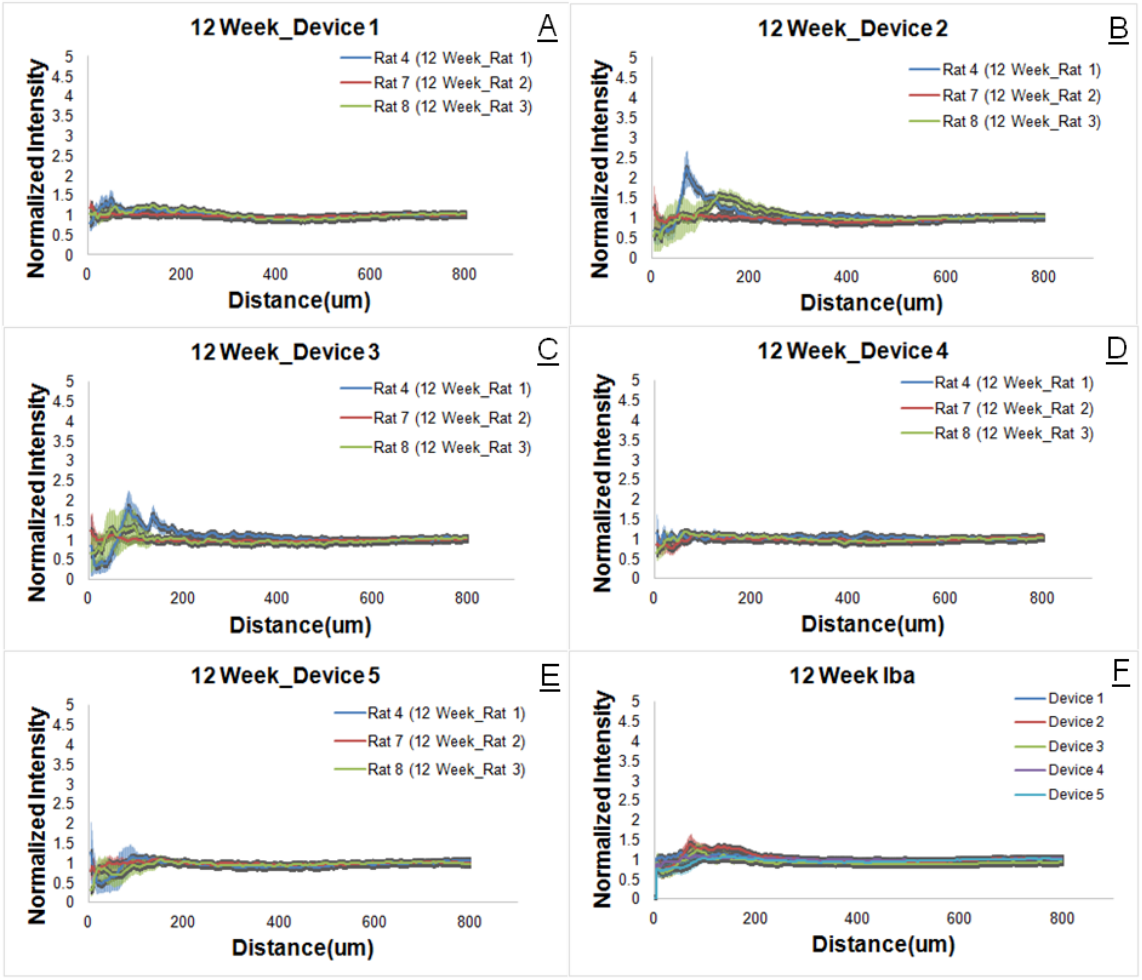

Figure A.4.4 : (A-E) Normallized intensity of Iba-1 staining vs. distance from the center of the implantation sites for 5 devices at 12 Weeks. (F) Normallized intensity of Iba-1 staining vs. distance from the center of the implantation sites. The intensity values were averaged across 3 animals within the time point.

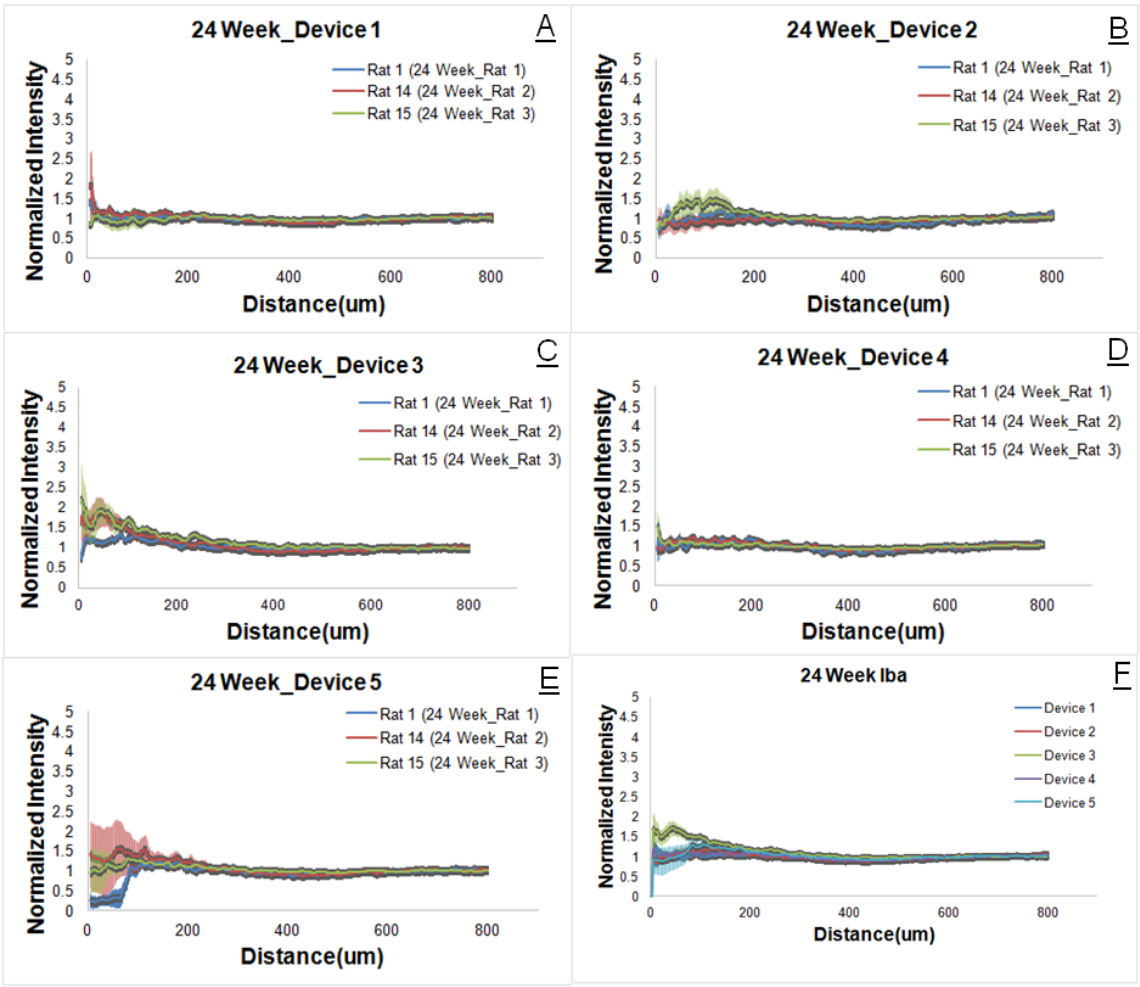

Figure A.4.6 : (A-E) Normallized intensity of Iba-1 staining vs. distance from the center of the implantation sites for 5 devices at 24 Weeks. (F) Normallized intensity of Iba-1 staining vs. distance from the center of the implantation sites. The intensity values were averaged across 3 animals within the time point.

A.5 Relationship between astrocyte and microglia for each device at different time points

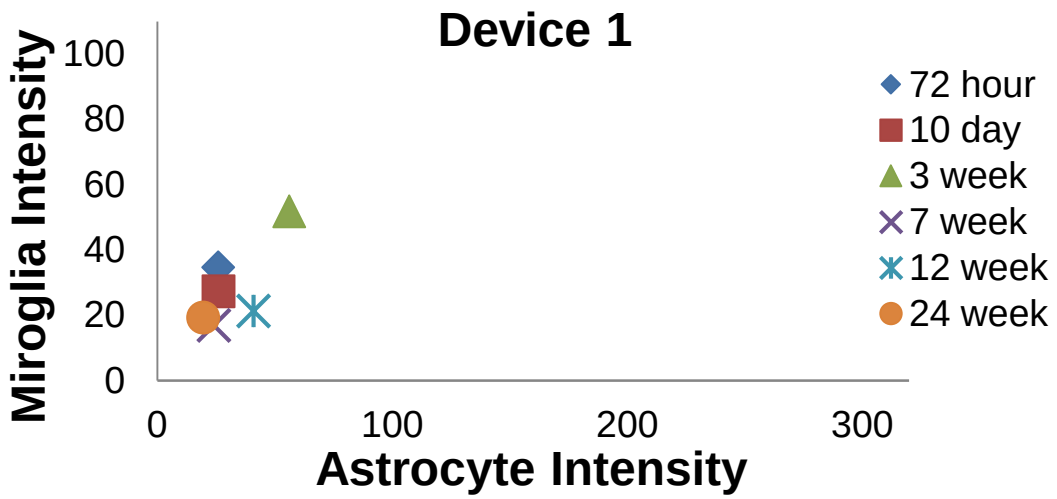

Figure A.5.1 : Relationship between astrocytes vs.microglia for Device 1 at different time points. Device dimension : The probe : 30 µm × 5 µm × 3.5 mm. The polymer coating: 100 µm × 100 µm × 4 mm.

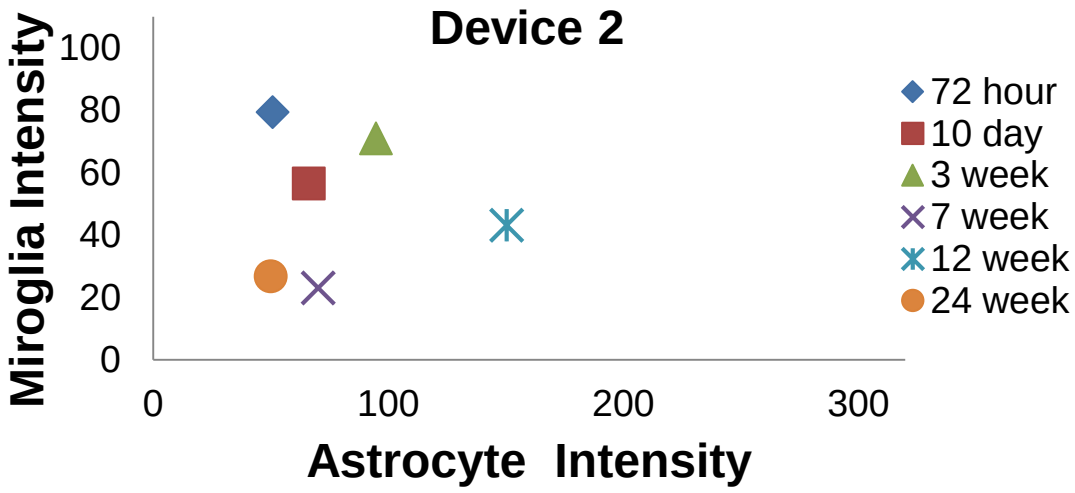

Figure A.5.2 : Relationship between astrocytes vs.microglia for Device 2 at different time points. Device dimension : The probe : 80 µm × 5 µm × 3.5 mm. The polymer coating: 100 µm × 100 µm × 4 mm.

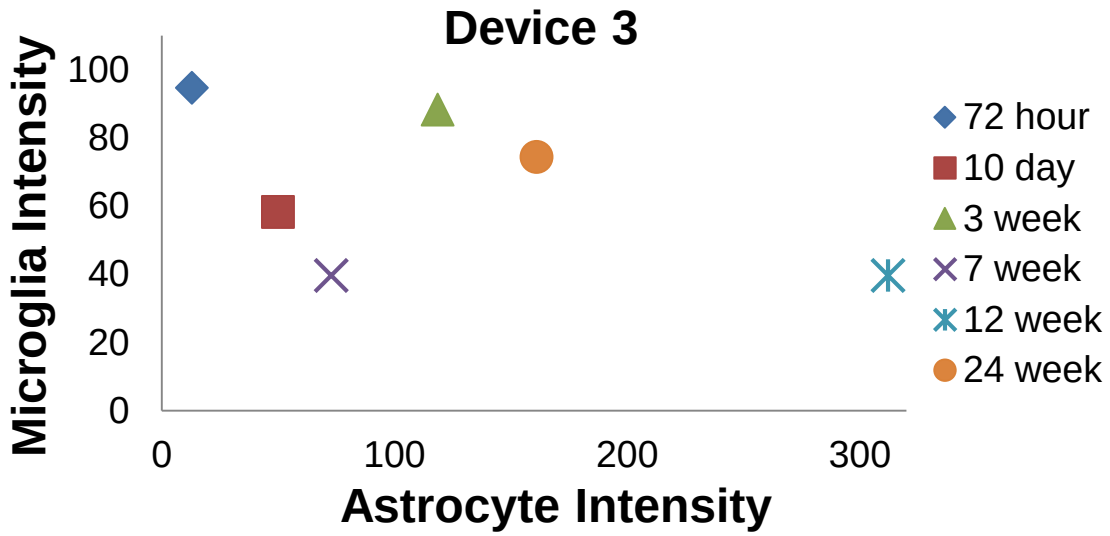

Figure A.5.3 : Relationship between astrocytes vs.microglia for Device 3 at different time points. Device dimension : The probe : 30 µm × 5 µm × 3.5 mm. The polymer coating: 200 µm × 200 µm × 4 mm.

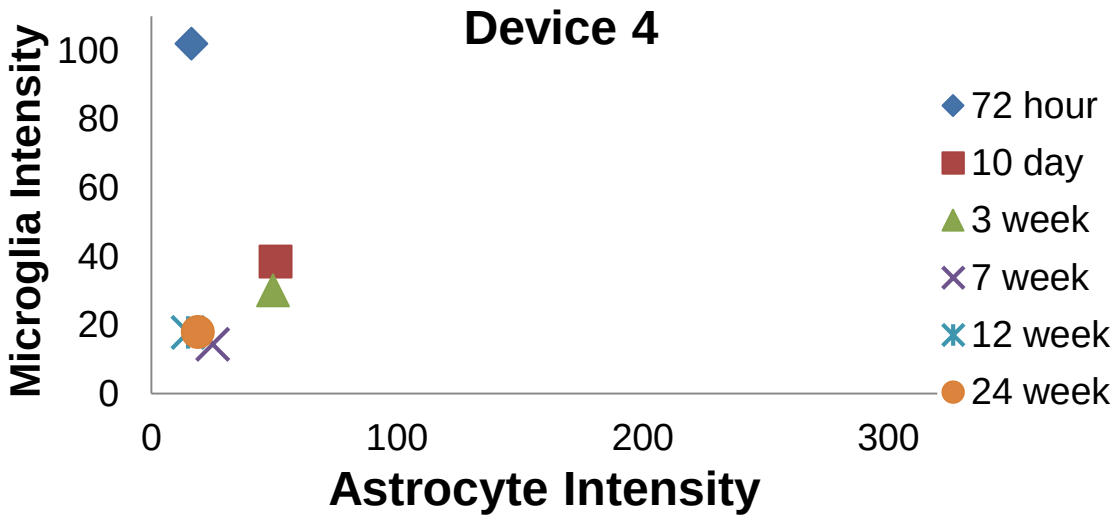

Figure A.5.4 : Relationship between astrocytes vs.microglia for Device 4 at different time points. Device dimension : The probe : no probe. The polymer coating: 100 µm × 100 µm × 4 mm.

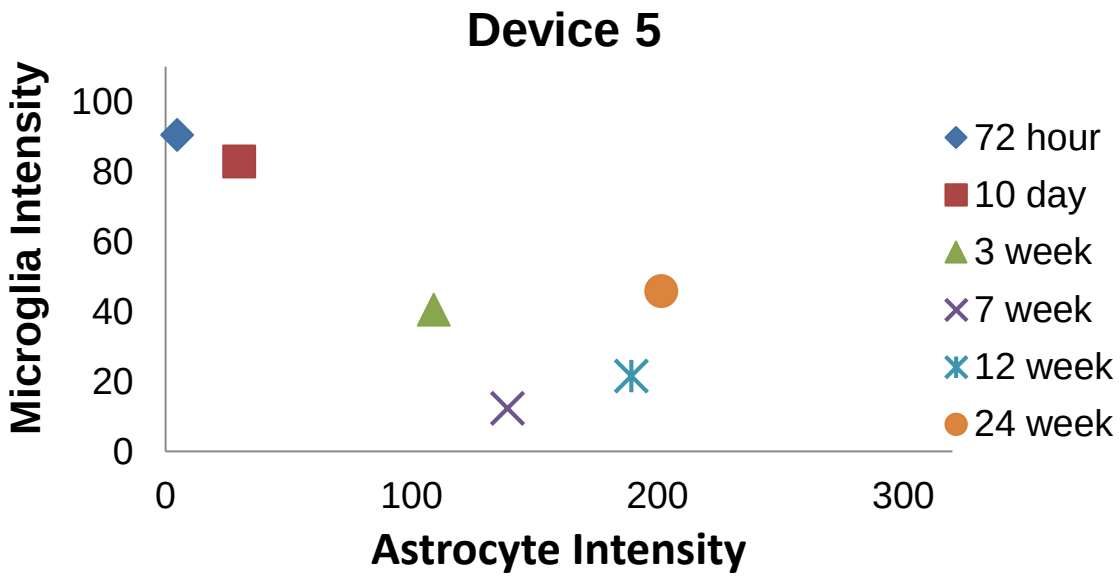

Figure A.5.5 : Relationship between astrocytes vs.microglia for Device 5 at different time points. Device dimension : 320 µm × 5 µm × 3.5 mm. The polymer coating: 350 µm × 100 µm × 4 mm.

BIBLIOGRAPHY

1. *Neural Engineering*. (Springer US, 2005). doi:10.1007/b112182

2. Lancioni, G. E. *et al.* Technology-aided programs for assisting communication and leisure engagement of persons with amyotrophic lateral sclerosis: two single-case studies. *Res. Dev. Disabil.* **33,** 1605–14 (2012).

3. Wolpaw, J. R. *et al.* Brain-computer interface technology: a review of the first international meeting. *IEEE Trans. Rehabil. Eng.* **8,** 164–173 (2000).

4. Ming, C., Xiaorong, G., Shangkai, G. & Dingfeng, X. Design and implementation of a brain-computer interface with high transfer rates. *Biomed. Eng. IEEE Trans.* **49,** 1181–1186 (2002).

5. Pfurtscheller, G. *et al.* Current trends in Graz brain-computer interface (BCI) research. *IEEE Trans. Rehabil. Eng.* **8,** 216–219 (2000).

6. Schwartz, A. B., Cui, X. T., Weber, D. J. & Moran, D. W. Brain-controlled interfaces: movement restoration with neural prosthetics. *Neuron* **52,** 205–20 (2006).

7. Leuthardt, E. C., Schalk, G., Roland, J., Rouse, A. & Moran, D. W. Evolution of brain-computer interfaces: going beyond classic motor physiology. *Neurosurg. Focus* **27,** E4 (2009).

8. Cooper, R., Winter, A. L., Crow, H. J. & Walter, W. G. Comparison of subcortical, cortical and scalp activity using chronically indwelling electrodes in man. *Electroencephalogr. Clin. Neurophysiol.* **18,** 217–228 (1965).

9. Ebersole, J. S. Defining Epileptogenic Foci: Past, Present, Future. *J. Clin. Neurophysiol.* **14,** 470–483 (1997).

10. Freeman, W. J., Holmes, M. D., Burke, B. C. & Vanhatalo, S. Spatial spectra of scalp EEG and EMG from awake humans. *Clin. Neurophysiol.* **114,** 1053–1068 (2003).

11. Daly, J. J. & Wolpaw, J. R. Brain-computer interfaces in neurological rehabilitation. *Lancet. Neurol.* **7,** 1032–43 (2008).

12. Rousche, P. J. & Normann, R. A. Chronic recording capability of the Utah Intracortical Electrode Array in cat sensory cortex. *J. Neurosci. Methods* **82,** 1–15 (1998).

13. Williams, J. C., Rennaker, R. L. & Kipke, D. R. Long-term neural recording characteristics of wire microelectrode arrays implanted in cerebral cortex. *Brain Res. Protoc.* **4,** 303–313 (1999).

14. Nicolelis, M. A. L. *et al.* Chronic, multisite, multielectrode recordings in macaque monkeys. *Proc. Natl. Acad. Sci. U. S. A.* **100,** 11041–6 (2003).

15. Franklin, B. An Account of the Effects of Electricity in Paralytic Cases. In a Letter to John Pringle, M. D. F. R. S. from Benjamin Franklin, Esq; F. R. S. *Philos. Trans.* **50,** 481–483 (1757).

16. AF, H. A. L. & H. Action potentials recorded from inside a nerve fibrer. *Nature* **144 ,** 710–711 (1939).

17. Hodgkin, A. L. & Huxley, A. F. A quantitative description of membrane current and its application to conduction and excitation in nerve. *J Physiol* **117,** 500–544 (1952).

18. Salcman, M. & Bak, M. J. Design, Fabrication, and In Vivo Behavior of Chronic Recording Intracortical Microelectrodes. *Biomed. Eng. IEEE Trans.* **BME-20,** 253–260 (1973).

19. Schmidt, E. M., Bak, M. J. & McIntosh, J. S. Long-term chronic recording from cortical neurons. *Exp. Neurol.* **52,** 496–506 (1976).

20. Najafi, K. Solid-state microsensors for cortical nerve recordings. *Eng. Med. Biol. Mag. IEEE* **13,** 375–387 (1994).

21. Brindley, G. S. & Lewin, W. S. The sensations produced by electrical stimulation of the visual cortex. *J Physiol* **196,** 479–493 (1968).

22. Wilson, B. S. & Dorman, M. F. Cochlear implants: A remarkable past and a brilliant future. *Hear. Res.* **242,** 3–21 (2008).

23. Limousin, P. *et al.* Electrical Stimulation of the Subthalamic Nucleus in Advanced Parkinson's Disease. *N. Engl. J. Med.* **339,** 1105–1111 (1998).

24. Wise, K. D., Angell, J. B. & Starr, A. An Integrated-Circuit Approach to Extracellular Microelectrodes. *Biomed. Eng. IEEE Trans.* **BME-17,** 238–247 (1970).

25. Najafi, K., Ji, J. & Wise, K. D. Scaling limitations of silicon multichannel recording probes. *IEEE Trans Biomed Eng* **37,** 1–11 (1990).

26. Jones, K., Campbell, P. & Normann, R. A glass/silicon composite intracortical electrode array. *Ann. Biomed. Eng.* **20,** 423–437 (1992).

27. Qing, B., Wise, K. D. & Anderson, D. J. A high-yield microassembly structure for three-dimensional microelectrode arrays. *Biomed. Eng. IEEE Trans.* **47,** 281–289 (2000).

28. Jessin, J., Yuefa, L., Jinsheng, Z., Jeffrey, A. L. & Yong, X. Microfabrication of 3D neural probes with combined electrical and chemical interfaces. *J. Micromechanics Microengineering* **21,** 105011 (2011).

29. Ming-Fang, W., Teimour, M. & Babak, Z. A self-assembled 3D microelectrode array. *J. Micromechanics Microengineering* **20,** 35013 (2010).

30. Campbell, P. K., Jones, K. E., Huber, R. J., Horch, K. W. & Normann, R. A. A silicon-based, three-dimensional neural interface: manufacturing processes for an intracortical electrode array. *Biomed. Eng. IEEE Trans.* **38,** 758–768 (1991).

31. Ying, Y., Gulari, M. N., Wiler, J. A. & Wise, K. D. A Microassembled Low-Profile Three-Dimensional Microelectrode Array for Neural Prosthesis Applications. *Microelectromechanical Syst. J.* **16,** 977–988 (2007).

32. Spieth, S. *et al.* A floating 3D silicon microprobe array for neural drug delivery compatible with electrical recording. *J. Micromechanics Microengineering* **21,** 125001 (2011).

33. Stieglitz, T., Beutel, H., Blau, C. & Meyer, J. U. Flexible multichannel microelectrodes with integrated leads for use in neuroprosthetics. *Biomed Tech* **42 Suppl,** 449–450 (1997).

34. Smith, C. *et al.* Development and investigation of flexible polymer neural probe for chronic neural recording. 834404 (2012). doi:10.1117/12.917481

35. González, C. & Rodríguez, M. A flexible perforated microelectrode array probe for action potential recording in nerve and muscle tissues. *J. Neurosci. Methods* **72,** 189–195 (1997).

36. Turner, J. N. *et al.* Cerebral Astrocyte Response to Micromachined Silicon Implants. *Exp. Neurol.* **156,** 33–49 (1999).

37. Polikov, V. S., Tresco, P. A. & Reichert, W. M. Response of brain tissue to chronically implanted neural electrodes. *J. Neurosci. Methods* **148,** 1–18 (2005).

38. Wang, J. H.-C. & Thampatty, B. P. Mechanobiology of adult and stem cells. *Int. Rev. Cell Mol. Biol.* **271,** 301–46 (2008).

39. Vetter, R. J., Williams, J. C., Hetke, J. F., Nunamaker, E. A. & Kipke, D. R. Chronic neural recording using silicon-substrate microelectrode arrays implanted in cerebral cortex. *IEEE Trans. Biomed. Eng.* **51,** 896–904 (2004).

40. Lund, T. *et al.* Shear stress regulates inflammatory and thrombogenic gene transcripts in cultured human endothelial progenitor cells. *Thromb. Haemost.* **104,** 582–591 (2010).

41. Kozai, T. D. Y., Vazquez, A. L., Weaver, C. L., Kim, S.-G. & Cui, X. T. In vivo two-photon microscopy reveals immediate microglial reaction to implantation of microelectrode through extension of processes. *J. Neural Eng.* **9,** 066001 (2012).

42. Edell, D. J., Toi, V. V, McNeil, V. M. & Clark, L. D. Factors influencing the biocompatibility of insertable silicon microshafts in cerebral cortex. *Biomed. Eng. IEEE Trans.* **39,** 635–643 (1992).

43. Seymour, J. P. & Kipke, D. R. Neural probe design for reduced tissue encapsulation in CNS. *Biomaterials* **28,** 3594–3607 (2007).

44. Biran, R., Martin, D. C. & Tresco, P. A. Neuronal cell loss accompanies the brain tissue response to chronically implanted silicon microelectrode arrays. *Exp. Neurol.* **195,** 115–26 (2005).

45. Szarowski, D. H. *et al.* Brain responses to micro-machined silicon devices. *Brain Res.* **983,** 23–35 (2003).

46. Giordana, M. T. *et al.* Reactive cell proliferation and microglia following injury to the rat brain. *Neuropathol. Appl. Neurobiol.* **20,** 163–174 (1994).

47. Fujita, T., Yoshimine, T., Maruno, M. & Hayakawa, T. Cellular Dynamics of Macrophages and Microglial Cells in Reaction to Stab Wounds in Rat Cerebral Cortex. *Acta Neurochir. (Wien).* **140,** 275–279 (1998).

48. Bjornsson, C. S. *et al.* Effects of insertion conditions on tissue strain and vascular damage during neuroprosthetic device insertion. *J. Neural Eng.* **3,** 196–207 (2006).

49. Saxena, T. *et al.* The impact of chronic blood-brain barrier breach on intracortical electrode function. *Biomaterials* **34,** 4703–13 (2013).

50. Leskovar, A., Moriarty, L., Turek, J., Schoenlein, I. & Borgens, R. The macrophage in acute neural injury: changes in cell numbers over time and levels of cytokine production in mammalian central and peripheral nervous systems. *J. Exp. Biol.* **203,** 1783–1795 (2000).

51. Mercanzini, A., Colin, P., Bensadoun, J. C., Bertsch, A. & Renaud, P. In vivo electrical impedance spectroscopy of tissue reaction to microelectrode arrays. *IEEE Trans Biomed Eng* **56,** 1909–1918 (2009).

52. Williams, J. C., Hippensteel, J. A., Dilgen, J., Shain, W. & Kipke, D. R. Complex impedance spectroscopy for monitoring tissue responses to inserted neural implants. *J. Neural Eng.* **4,** 410–23 (2007).

53. Azemi, E., Lagenaur, C. F. & Cui, X. T. The surface immobilization of the neural adhesion molecule L1 on neural probes and its effect on neuronal density and gliosis at the probe/tissue interface. *Biomaterials* **32,** 681–92 (2011).

54. Rathjen, F. G. & Schachner, M. Immunocytological and biochemical characterization of a new neuronal cell surface component (L1 antigen) which is involved in cell adhesion. *EMBO J.* **3,** 1–10 (1984).

55. Dihné, M., Bernreuther, C., Sibbe, M., Paulus, W. & Schachner, M. A new role for the cell adhesion molecule L1 in neural precursor cell proliferation, differentiation, and transmitter-specific subtype generation. *J. Neurosci.* **23,** 6638–50 (2003).

56. Zhong, Y. & Bellamkonda, R. V. Dexamethasone-coated neural probes elicit attenuated inflammatory response and neuronal loss compared to uncoated neural probes. *Brain Res.* **1148,** 15–27 (2007).

57. Abidian, M. R., Kim, D.-H. & Martin, D. C. Conducting-Polymer Nanotubes for Controlled Drug Release. *Adv. Mater.* **18,** 405–409 (2006).

58. Spataro, L. *et al.* Dexamethasone treatment reduces astroglia responses to inserted neuroprosthetic devices in rat neocortex. *Exp. Neurol.* **194,** 289–300 (2005).

59. Kim, D.-H. & Martin, D. C. Sustained release of dexamethasone from hydrophilic matrices using PLGA nanoparticles for neural drug delivery. *Biomaterials* **27,** 3031–3037 (2006).

60. Lee, C. D. *et al.* Matrigel coatings for Parylene sheath neural probes. *J. Biomed. Mater. Res. B. Appl. Biomater.* (2015). doi:10.1002/jbm.b.33390

61. Purcell, E. K., Thompson, D. E., Ludwig, K. A. & Kipke, D. R. Flavopiridol reduces the impedance of neural prostheses in vivo without affecting recording quality. *J. Neurosci. Methods* **183,** 149–57 (2009).

62. Abidian, M. R., Corey, J. M., Kipke, D. R. & Martin, D. C. Conducting-polymer nanotubes improve electrical properties, mechanical adhesion, neural attachment, and neurite outgrowth of neural electrodes. *Small* **6,** 421–9 (2010).

63. Cui, X. *et al.* Surface modification of neural recording electrodes with conducting polymer/biomolecule blends. *J. Biomed. Mater. Res.* **56,** 261–72 (2001).

64. Vitale, F., Summerson, S. R., Aazhang, B., Kemere, C. & Pasquali, M. Neural stimulation and recording with bidirectional, soft carbon nanotube fiber microelectrodes. *ACS Nano* **9,** 4465–74 (2015).

65. Groenendaal, L., Jonas, F., Freitag, D., Pielartzik, H. & Reynolds, J. R. Poly(3,4-ethylenedioxythiophene) and Its Derivatives: Past, Present, and Future. *Adv. Mater.* **12,** 481–494 (2000).

66. Nyberg, T., Shimada, A. & Torimitsu, K. Ion conducting polymer microelectrodes for interfacing with neural networks. *J. Neurosci. Methods* **160,** 16–25 (2007).

67. Green, R. A. *et al.* Substrate dependent stability of conducting polymer coatings on medical electrodes. *Biomaterials* **33,** 5875–86 (2012).

68. Kozai, T. *et al.* Chronic in vivo evaluation of PEDOT/CNT for stable neural recordings. *IEEE Trans. Biomed. Eng.* **PP,** 1 (2015).

69. Kolarcik, C. L. *et al.* Evaluation of poly(3,4-ethylenedioxythiophene)/carbon nanotube neural electrode coatings for stimulation in the dorsal root ganglion. *J. Neural Eng.* **12,** 016008 (2015).

70. Kozai, T. D. Y., Jaquins-Gerstl, A. S., Vazquez, A. L., Michael, A. C. & Cui, X. T. Brain tissue responses to neural implants impact signal sensitivity and intervention strategies. *ACS Chem. Neurosci.* **6,** 48–67 (2015).

71. Kolarcik, C. L. *et al.* Evaluation of poly(3,4-ethylenedioxythiophene)/carbon nanotube neural electrode coatings for stimulation in the dorsal root ganglion. *J. Neural Eng.* **12,** 016008 (2015).

72. Kipke, D. R. *et al.* Advanced neurotechnologies for chronic neural interfaces: new horizons and clinical opportunities. *J. Neurosci.* **28,** 11830–8 (2008).

73. Kozai, T. D. Y. *et al.* Ultrasmall implantable composite microelectrodes with bioactive surfaces for chronic neural interfaces. *Nat. Mater.* **11,** 1065–73 (2012).

74. Kozai, T. D. Y. *et al.* Comprehensive chronic laminar single-unit, multi-unit, and local field potential recording performance with planar single shank electrode arrays. *J. Neurosci. Methods* **242,** 15–40 (2015).

75. Kozai, T. D. Y. *et al.* Mechanical failure modes of chronically implanted planar silicon-based neural probes for laminar recording. *Biomaterials* **37,** 25–39 (2015).

76. Kozai, T. D. Y. *et al.* Ultrasmall implantable composite microelectrodes with bioactive surfaces for chronic neural interfaces. *Nat. Mater.* **11,** 1065–73 (2012).

77. Takeuchi, S., Suzuki, T., Mabuchi, K. & Fujita, H. 3D flexible multichannel probe array. in *Micro Electro Mech. Syst. 2003. MEMS-03 Kyoto. IEEE Sixt. Annu. Int. Conf.* 367–370 (2003). doi:10.1109/memsys.2003.1189762

78. Subbaroyan, J. & Kipke, D. R. The role of flexible polymer interconnects in chronic tissue response induced by intracortical microelectrodes - a modeling and an in vivo study. in *Eng. Med. Biol. Soc. 2006. EMBS '06. 28th Annu. Int. Conf. IEEE* 3588–3591 (2006). doi:10.1109/iembs.2006.260517

79. Harrison, D. G. *et al.* Endothelial mechanotransduction, nitric oxide and vascular inflammation. *J. Intern. Med.* **259,** 351–63 (2006).

80. Lund, T. *et al.* Shear stress regulates inflammatory and thrombogenic gene transcripts in cultured human endothelial progenitor cells. *Thromb. Haemost.* **104,** 582–91 (2010).

81. Uhlig, S. Ventilation-induced lung injury and mechanotransduction: stretching it too far? *Am. J. Physiol. Lung Cell. Mol. Physiol.* **282,** L892–6 (2002).

82. Takeuchi, S. & Shimoyama, I. Three-dimensional shape memory alloy microelectrode with clipping structure for insect neural recording. *J. Microelectromechanical Syst.* **9,** 24–31 (2000).

83. Hoogerwerf, A. C. & Wise, K. D. A three-dimensional microelectrode array for chronic neural recording. *IEEE Trans. Biomed. Eng.* **41,** 1136–1146 (1994).

84. Sridharan, A., Nguyen, J. K., Capadona, J. R. & Muthuswamy, J. Compliant intracortical implants reduce strains and strain rates in brain tissue in vivo. *J. Neural Eng.* **12,** 036002 (2015).

85. Barz, F., Ruther, P., Takeuchi, S. & Paul, O. Flexible silicon-polymer neural probe rigidified by dissolvable insertion vehicle for high-resolution neural recording with improved duration. in *2015 28th IEEE Int. Conf. Micro Electro Mech. Syst.* 636–639 (IEEE, 2015). doi:10.1109/MEMSYS.2015.7051036

86. Fan, B., Rechenberg, R., Becker, M. F. & Li, W. Fabrication of polycrystalline diamond on a flexible Parylene substrate. in *2015 Transducers - 2015 18th Int. Conf. Solid-State Sensors, Actuators Microsystems* 892–895 (IEEE, 2015). doi:10.1109/TRANSDUCERS.2015.7181067

87. Schander, A. *et al.* Design and fabrication of multi-contact flexible silicon probes for intracortical floating implantation. in *2015 Transducers - 2015 18th Int. Conf. Solid-State Sensors, Actuators Microsystems* 1739–1742 (IEEE, 2015). doi:10.1109/TRANSDUCERS.2015.7181281

88. Altuna, A. *et al.* SU-8 based microprobes with integrated planar electrodes for enhanced neural depth recording. *Biosens. Bioelectron.* **37,** 1–5 (2012).

89. Cho, S.-H. *et al.* Biocompatible SU-8-Based Microprobes for Recording Neural Spike Signals From Regenerated Peripheral Nerve Fibers. *IEEE Sens. J.* **8,** 1830–1836 (2008).

90. Kim, B. J. *et al.* 3D Parylene sheath neural probe for chronic recordings. *J. Neural Eng.* **10,** 045002 (2013).

91. Felix, S. H. *et al.* Insertion of flexible neural probes using rigid stiffeners attached with biodissolvable adhesive. *J. Vis. Exp.* e50609 (2013). doi:10.3791/50609

92. Xiang, Z. *et al.* Ultra-thin flexible polyimide neural probe embedded in a dissolvable maltose-coated microneedle. *J. Micromechanics Microengineering* **24,** 065015 (2014).

93. Tan, K. L. *et al.* Polyethylene Glycol-Coated Polyimide-Based Probe with Neural Recording IC for Chronic Neural Recording. *Adv. Mater. Res.* **849,** 183–188 (2013).

94. Chen, C.-H. *et al.* Three-dimensional flexible microprobe for recording the neural signal. in *Nano/Molecular Med. Eng. (NANOMED), 2009 IEEE Int. Conf.* 278–281 (2009). doi:10.1109/nanomed.2009.5559071

95. Takeuchi, S., Ziegler, D., Yoshida, Y., Mabuchi, K. & Suzuki, T. Parylene flexible neural probes integrated with microfluidic channels. *Lab Chip* **5,** 519–523 (2005).

96. Chen, C.-H. *et al.* A three-dimensional flexible microprobe array for neural recording assembled through electrostatic actuation. *Lab Chip* **11,** 1647–55 (2011).

97. Chen, P.-C. & Lal, A. Detachable ultrasonic enabled inserter for neural probe insertion using biodissolvable Polyethylene Glycol. in *2015 Transducers - 2015 18th Int. Conf. Solid-State Sensors, Actuators Microsystems* 125–128 (IEEE, 2015). doi:10.1109/TRANSDUCERS.2015.7180877

98. Foley, C., Nishimura, N., Neeves, K., Schaffer, C. & Olbricht, W. Flexible microfluidic devices supported by biodegradable insertion scaffolds for convection-enhanced neural drug delivery. *Biomed. Microdevices* **11,** 915–924 (2009).

99. Gilgunn, P. J. *et al.* An ultra-compliant, scalable neural probe with molded biodissolvable delivery vehicle. in *Micro Electro Mech. Syst. (MEMS), 2012 IEEE 25th Int. Conf.* 56–59 (2012). doi:10.1109/memsys.2012.6170092

100. Ware, T. *et al.* Fabrication of Responsive, Softening Neural Interfaces. *Adv. Funct. Mater.* **22,** 3470–3479 (2012).

101. Jorfi, M. *et al.* Mechanically adaptive materials for intracortical implants. in *2015 7th Int. IEEE/EMBS Conf. Neural Eng.* 601–602 (IEEE, 2015). doi:10.1109/NER.2015.7146694

102. Zhao, Q., Qi, H. J. & Xie, T. Recent progress in shape memory polymer: New behavior, enabling materials, and mechanistic understanding. *Prog. Polym. Sci.* (2015). doi:10.1016/j.progpolymsci.2015.04.001

103. Harris, J. P. *et al.* Mechanically adaptive intracortical implants improve the proximity of neuronal cell bodies. *J. Neural Eng.* **8,** 066011 (2011).

104. Nguyen, J. K. *et al.* Mechanically-compliant intracortical implants reduce the neuroinflammatory response. *J. Neural Eng.* **11,** 056014 (2014).

105. Hess-Dunning, A. E. *et al.* Microscale Characterization of a Mechanically Adaptive Polymer Nanocomposite With Cotton-Derived Cellulose Nanocrystals for Implantable BioMEMS. *J. Microelectromechanical Syst.* **23,** 774–784 (2014).

106. Lo, M. *et al.* Coating flexible probes with an ultra fast degrading polymer to aid in tissue insertion. *Biomed. Microdevices* **17,** 9927 (2015).

107. Rojas, R., Harris, N. K., Piotrowska, K. & Kohn, J. Evaluation of automated synthesis for chain and step-growth polymerizations: Can robots replace the chemists? *J. Polym. Sci. Part A Polym. Chem.* **47,** 49–58 (2009).

108. Schut, J. *et al.* Glass transition temperature prediction of polymers through the mass-per-flexible-bond principle. *Polymer (Guildf).* **48,** 6115–6124 (2007).

109. Kishi, N., Chen, W. F. & Goto, Y. Effective Length Factor of Columns in Semirigid and Unbraced Frames. *J. Struct. Eng.* **123,** 313–320 (1997).

110. Cheng, M.-Y. *et al.* A flexible polyimide cable for implantable neural probe arrays. *Microsyst. Technol.* **19,** 1111–1118 (2012).

111. Kim, E., Xia, Y. & Whitesides, G. M. Micromolding in Capillaries: Applications in Materials Science. *J. Am. Chem. Soc.* **118,** 5722–5731 (1996).

112. Patel, J. N., Kaminska, B., Gray, B. L. & Gates, B. D. PDMS as a sacrificial substrate for SU-8-based biomedical and microfluidic applications. *J. Micromechanics Microengineering* **18,** 095028 (2008).

113. Zhu, T., Argyrakis, P., Mastropaolo, E., Lee, K. K. & Cheung, R. Dry etch release processes for micromachining applications. *J. Vac. Sci. Technol. B Microelectron. Nanom. Struct.* **25,** 2553–2557 (2007).

114. Chang, F. I. *et al.* Gas-phase silicon micromachining with xenon difluoride. 117–128 (1995). doi:10.1117/12.220933

115. Yi, W. *et al.* A flexible and implantable microelectrode arrays using high-temperature grown vertical carbon nanotubes and a biocompatible polymer substrate. *Nanotechnology* **26,** 125301 (2015).

116. Goodwin, T. W. & Morton, R. A. The spectrophotometric determination of tyrosine and tryptophan in proteins. *Biochem. J.* **40,** 628–32 (1946).

117. Chen, Z.-J. *et al.* A realistic brain tissue phantom for intraparenchymal infusion studies. *J. Neurosurg.* **101,** 314–22 (2004).

118. Senkevich, J. J. & Wang, P.-I. Molecular Layer Chemistry via Parylenes. *Chem. Vap. Depos.* **15,** 91–94 (2009).

119. Senkevich, J. J. & Desu, S. B. Compositional studies of near-room-temperature thermal CVD poly(chloro-p-xylylene)/SiO 2 nanocomposites. *Appl. Phys. A Mater. Sci. Process.* **70,** 541–546 (2000).

120. Fortin, J. B. & Lu, T.-M. *Chemical Vapor Deposition Polymerization: The Growth and Properties of Parylene Thin Films*. **30,** (Springer Science & Business Media, 2003).

121. Winslow, B. D. & Tresco, P. A. Quantitative analysis of the tissue response to chronically implanted microwire electrodes in rat cortex. *Biomaterials* **31,** 1558–67 (2010).

122. Prasad, A. *et al.* Comprehensive characterization and failure modes of tungsten microwire arrays in chronic neural implants. *J. Neural Eng.* **9,** 056015 (2012).

123. Kim, E. G. R. *et al.* A hybrid silicon–parylene neural probe with locally flexible regions. *Sensors Actuators B Chem.* **195,** 416–422 (2014).

124. Abidian, M. R. & Martin, D. C. Multifunctional Nanobiomaterials for Neural Interfaces. *Adv. Funct. Mater.* **19,** 573–585 (2009).

125. Biran, R., Martin, D. C. & Tresco, P. A. Neuronal cell loss accompanies the brain tissue response to chronically implanted silicon microelectrode arrays. *Exp. Neurol.* **195,** 115–126 (2005).

126. Lewitus, D., Smith, K. L., Shain, W. & Kohn, J. Ultrafast resorbing polymers for use as carriers for cortical neural probes. *Acta Biomater* **7,** 9 (2011).

127. Kozai, T. D. Y. *et al.* Chronic tissue response to carboxymethyl cellulose based dissolvable insertion needle for ultra-small neural probes. *Biomaterials* **35,** 9255–68 (2014).

128. Cogan, S. F. Neural stimulation and recording electrodes. *Annu. Rev. Biomed. Eng.* **10,** 275–309 (2008).

129. Ward, M. P., Rajdev, P., Ellison, C. & Irazoqui, P. P. Toward a comparison of microelectrodes for acute and chronic recordings. *Brain Res.* **1282,** 183–200 (2009).

130. Cogan, S. F., Troyk, P. R., Ehrlich, J. & Plante, T. D. In vitro comparison of the charge-injection limits of activated iridium oxide (AIROF) and platinum-iridium microelectrodes. *IEEE Trans. Biomed. Eng.* **52,** 1612–4 (2005).

131. Karp, F. B., Bernotski, N. A., Valdes, T. I., Bohringer, K. F. & Ratner, B. D. Foreign Body Response Investigated With an Implanted Biosensor by <emphasis emphasistype='italic'>In Situ</emphasis> Electrical Impedance Spectroscopy. *IEEE Sens. J.* **8,** 104–112 (2008).

132. HajjHassan, M., Chodavarapu, V. & Musallam, S. NeuroMEMS: Neural Probe Microtechnologies. *Sensors* **8,** 6704–6726 (2008).

133. Onaral, B. & Schwan, H. P. Linear and nonlinear properties of platinum electrode polarisation. Part 1: frequency dependence at very low frequencies. *Med. Biol. Eng. Comput.* **20,** 299–306 (1982).

134. Kim, B. J. *et al.* 3D Parylene sheath neural probe for chronic recordings. *J. Neural Eng.* **10,** 045002 (2013).

135. Chen, Z.-J. *et al.* A realistic brain tissue phantom for intraparenchymal infusion studies. *J. Neurosurg.* **101,** 314–22 (2004).

136. Daly,J.J. & Wolpaw, J. R. Brain-computer interfaces in neurological rehabilitation. *Lancet. Neurol.* **7,** 1032–43 (2008).

137. Bai, Q. & Wise, K. D. Single-unit neural recording with active microelectrode arrays. *IEEE Trans. Biomed. Eng.* **48,** 911–20 (2001).